ISSN 0912-1803

PHOTON FACTORY ACTIVITY REPORT

1989

#7

NATIONAL LABORATORY FOR HIGH ENERGY PHYSICS, KEK

Photon Factory

Activity Report

1989

Staff members and users of the Photon Factory are gathering with Mt. Tsukuba in their background

KEK Progress Report 89- 3 A/M

KEK Reports are available from:

Technical Information & Library
National Laboratory for High Energy Physics
1-1 Oho, Tsukuba-shi
Ibaraki-ken, 305
JAPAN

Phone: 0298-64-1171
Telex: 3652-534 (Domestic)
(0)3652-534 (International)
Fax: 0298-64-4604
Cable: KEKOHO

PREFACE

Since the Photon Factory was commissioned with 13 experimental stations in 1982, the annual number of experiments has increased with a rate of 25% per year, and 500 experiments are now running annually with about 50 experimental stations, the total operation time of the 2.5 GeV storage ring was 3400 hour in 1989, and the number of users was more than 2000, including 300 scientists from industry.

This wide usage of synchrotron radiation has been supported by good performance of the accelerators. The positron beam current of the linac was increased for rapid injection (injection time: 20 min). The entire roof of the Light Source building was covered with thermal insulator (urethane-foam). This has greatly improved the beam stability of the ring. It has been operated at an initial ring current of 350 mA with a life time of 20 hours.

Distinctive instrumentation at the Photon Factory has expanded to various fields such as angle-resolved ion-spectroscopy, dispersive EXAFS, trace impurity X-ray fluorescence analysis, plane-wave topography, structure analysis under high pressure, and imaging plates. Recently, experiments of protein structure analysis have been carried out extensively; Sakabe developed a new type of Weissenberg camera for protein crystallography, and about 50 experiments have been done for the past six months by a combination of Sakabe camera and imaging plates. One can understand his effective method by noting the fact that structure determination has been made for only 350 species of protein in the world since the beginning of X-ray protein crystallography. The 2.5 GeV light source is now at an entrance of its harvest season.

The TRISTAN Accumulation Ring has been used throughout this year in a time sharing basis with the TRISTAN experiment; twenty minutes for injection to TRISTAN Main Ring and 2 hours for SR experiment. The main subject has been magnetic Compton scattering with circularly polarized wiggler radiation. Such experiences enable us to expand our perspective for resarch in the following decade; we are investigating the possibility of operating the TRISTAN Main Ring at 6-8 GeV with 6000-pole undulators, resulting in an extremely brilliant radiation source (Emittance: 0.1 nm·rad at 5 GeV with damping rings).

We would like to mention here the retirement of professor G. Horikoshi and Professor K. Huke at the end of March, 1989. Prof. Horikoshi jointed KEK in 1972 in order to construct the vacuum system for the 12 GeV Proton Synchrotron. He has served as the director of Injector Linac Division from April 1987. Thanks to his great efforts, a high-current positron beam is now available for the PF and TRISTAN experiments. Prof. Huke jointed KEK in 1979 to construct the Photon Factory as the director of Light Source Division. He greatly contributed to its foundation as one of the originators of the Photon Factory and has brought it to today's high status through his enthusiastic endeavors.

Jun-ichi Chikawa
Director of the Photon Factory

EDITORIAL

The editors are sending herewith a new volume of the Photon Factory Activity Report which summarizes our activities in the past year. The report compiles a large number of user's short reports on various kinds of experiments made in this facility. These reports are classified according to the PAC codes. The report also includes text describing the Injector Linac, Light Source and Instrumentation Divisions. Most materials in the text carry the names of authors with whom readers may contact directly for further discussion if necessary. Also intended is to make the volume a package of basic information on this facility such as various parameters of the machines, insertion devices, beamlines and experimental apparatuses.

The editors would like to appreciate Yoshiko Yamaguchi, Miyako Kimura, and Kiyoko Yano for their hard work in preparation of this issue. All the PF members who contributed to this volume are acknowledged.

You can jump to the article by clicking its title.

Contents

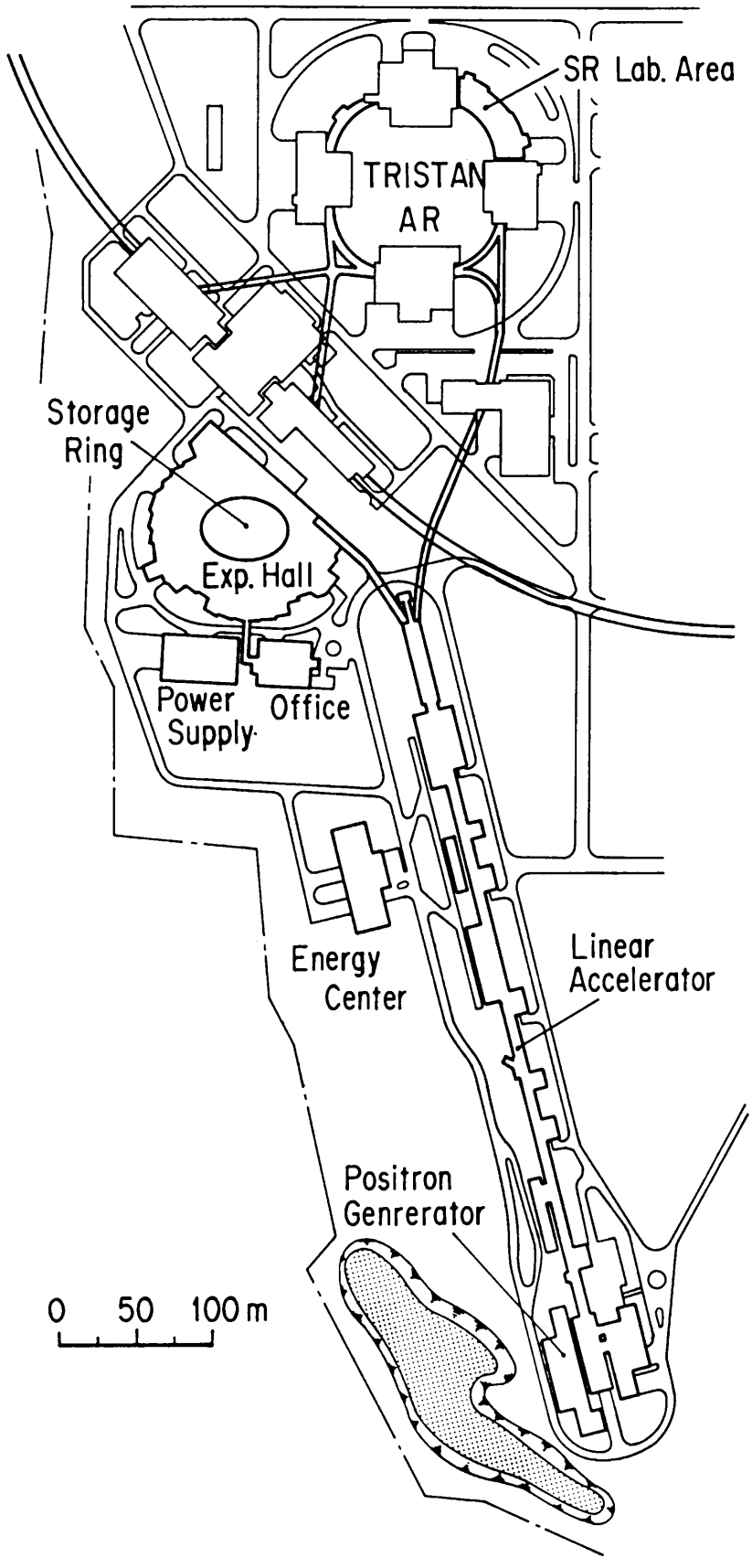

Fig. 1 Plan view of the Photon Factory

OUTLINE OF THE PHOTON FACTORY

A. INTRODUCTION

The Photon Factory (PF) is a national synchrotron radiation (SR) research facility affiliated with the National Laboratory for High Energy Physics (KEK), supervised by the Ministry of Education, Science and Culture. It consists of a 2.5-GeV electron/position linear accelerator, 2.5-GeV electron/position storage ring as a dedicated light source, and beamlines and experimental stations for exploiting synchrotron radiation, in studies involving such research fields as physics, chemistry, biology, medical sciences, pharmacology, earth sciences and lithography. All of the facilities for synchrotron radiation research are open to scientists of universities and research institutes belonging to the government, public organizations, private enterprises and those of foreign countries. The members of institutions affiliated with the Ministry of Education, Science and Culture are given the highest priority among all users. Applications from other organizations are also admitted with or without charge, depending upon the categories of their objectives.

The Photon Factory is located at the northern end of Tsukuba Science City, about 60 km north-east of Tokyo.

B. OVERVIEW OF THE FACILITY

The general view of the facility is shown in Fig. 1. The 2.5-GeV linac housed in a 450 m long enclosure is used as an injector for both the PF storage ring and the accumulation ring (AR) of TRISTAN. The PF storage ring was already facilitated with the flexibility of storing positrons in place of electrons. The part of AR has been used as high energy synchrotron radiation source from its bending magnet and partly augmented with a new insertion device to produce elliptical polarized radiation. It has been operated for synchrotron radiation users with the energy range from 5 to 6.5 GeV.

C. ORGANIZATION AND STAFF

The organization structure of KEK is shown in Fig. 2. The PF is composed of three divisions; Injector Linac, Light Source and Instrumentation. The organizational structure of the PF including its personnel is shown in Fig. 3. The Advisory Council for the PF was established to discuss scientific programs and management of the PF. The council consists of twenty-one of learned and experienced persons including ten non-KEK members (Table 1). The term of the membership is two years; half of the outside members are changed every year. The Program Advisory Committee (PAC) consisting of the members listed in Table 2 accepts proposals of users and decides priorities for the experiments.

In Table 3, the names of the staff members are listed to make direct and quick contact. Also, the number of staff members and visiting scientists are summarized in Table 4.

D. BUDGET

The budget of the PF during the construction period and after commissioning of the facilities are shown in Table 5 and 6. Financial support for the PF is made by the government. The numbers of beam channels in each year are shown in Table 7.

E. OPERATION TIME AND PROPOSAL

The machine operation time is divided into three terms in every year. The operation schedule and time table of FY 1989 are summarized in Table 8 and 9 respectively. Fig. 4 shows the annual ring operation time of the PF. This indicates that the ring operation time has remarkably increased; the ratio of user time in those of whole ring operation has been getting dominative.

About 25 % of the operation time is used for machine studies. Such studies have been effective in improving stability, beam life time, low emittance operation and positron accumulation.

There are three ways of access to make experiments at the PF. The first category is for scientists of universities, research institutes belonging to the government or public organizations who can make experiments without charge if their proposals are accepted by the PAC. The proposal is valid for two years. The deadlines for the applications are January 14 and July 15 every year. An urgent proposal is also accepted any time. The number of proposals approved by the PAC since commissioning of the PF is listed in Table 10.

The second category is for scientists of private corporations who have to pay all the expenses. No approval by the PAC is required.

The third category is for collaboration between staff members of the PF and scientists of private corporations; no charge and no approval by the PAC are required but renewed every fiscal year starting April.

All the proposals belonging to the three categories approved during FY 1989 are listed at the end of this section.

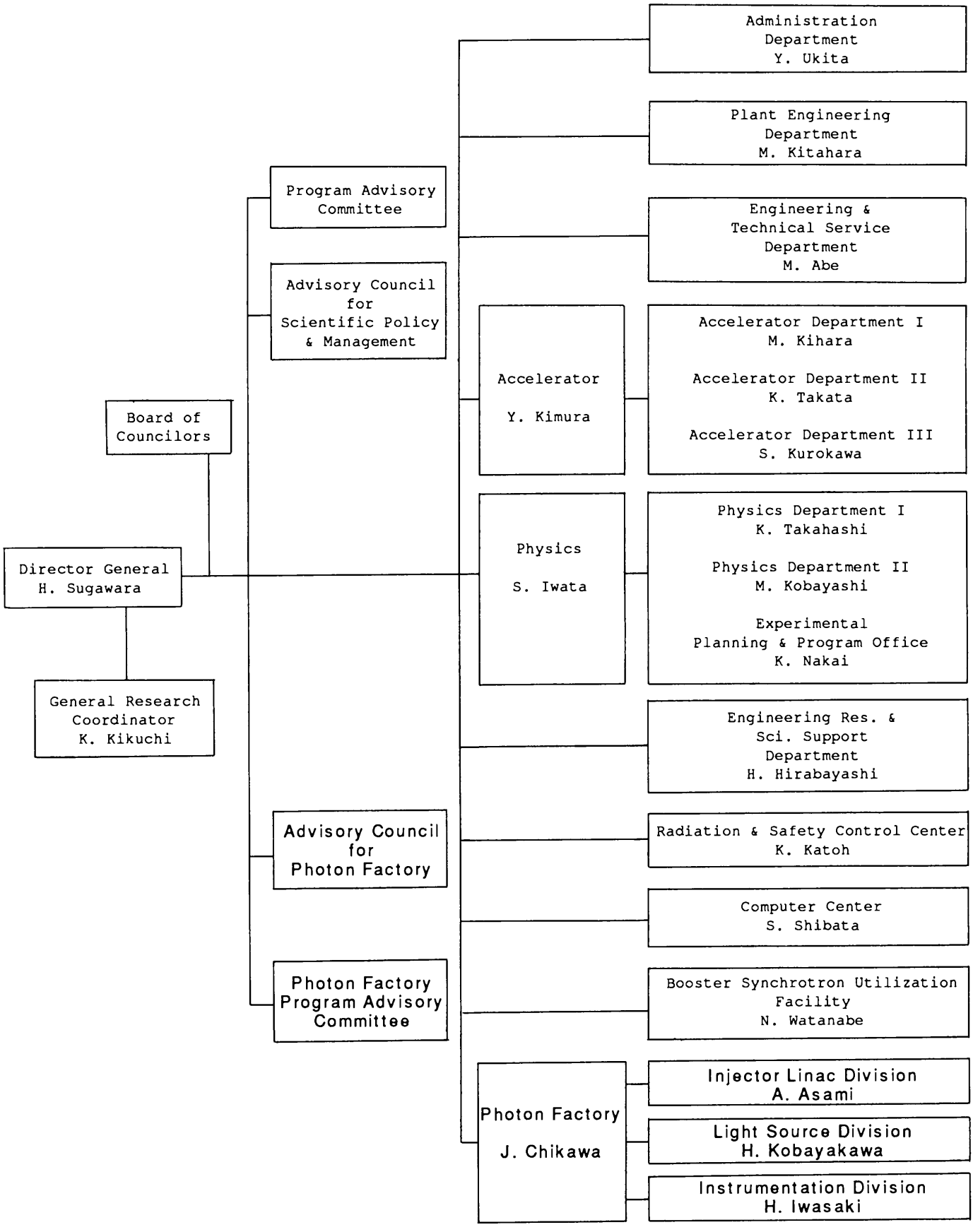

Fig. 2 Organization of KEK

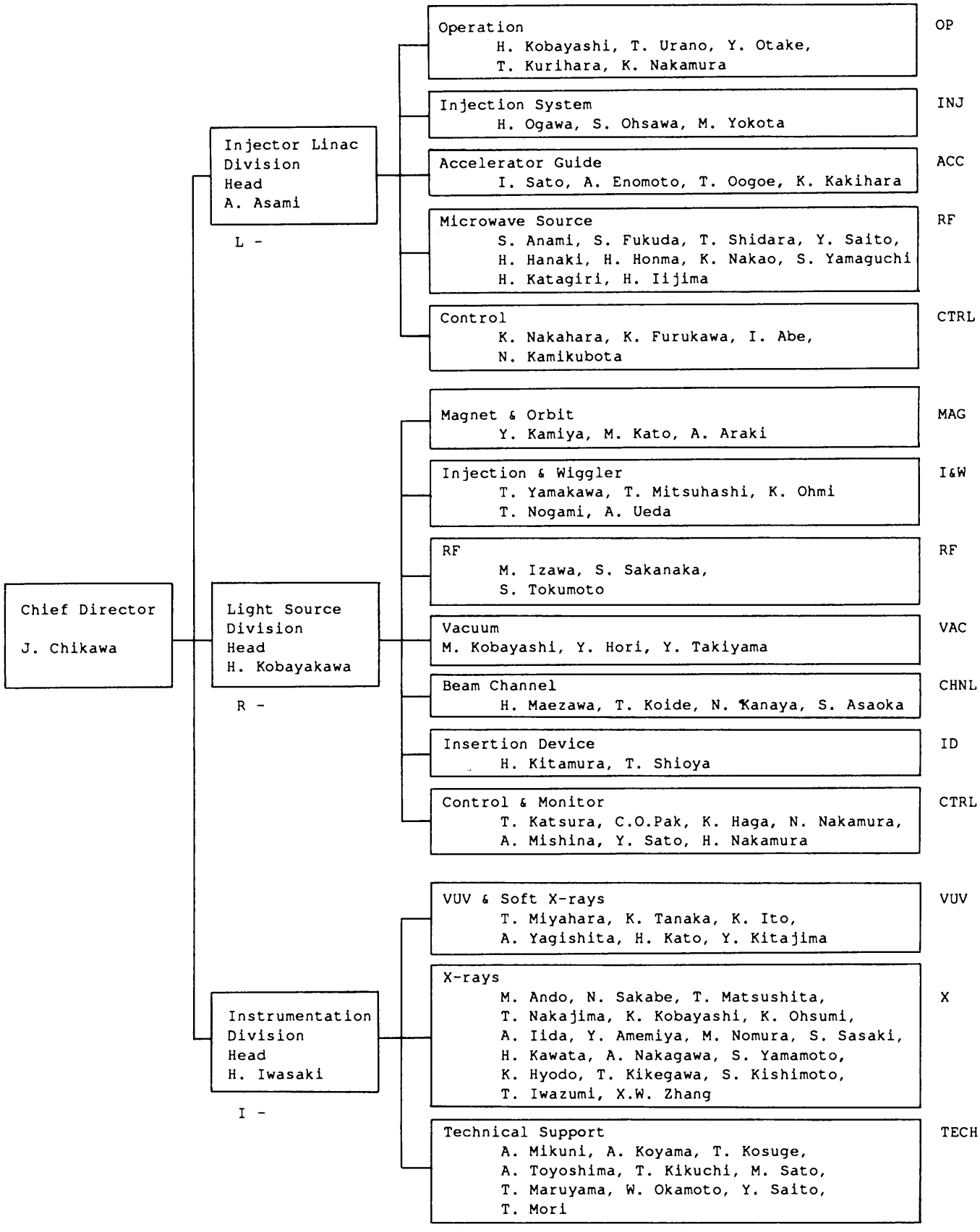

Fig. 3 Organization and Members of Photon Factory

Table 1 Members of Advisory Council * Chairman ** Vice-Chairman

Prof. ANDO, Masami	PF Instrumentation Division, KEK
Prof. ASAMI, Akira	Head of PF Injector Linac Division, KEK
Prof. FUJII, Yasuhiko	Institute of Materials Science, University of Tsukuba
Prof. HIEDA, Kotaro	Faculty of Science, Rikkyo University
Prof. IIJIMA, Takao	Faculty of Science, Gakushuin University
Prof. ISHII, Takehiko	Institute for Solid State Physics, University of Tokyo
Prof. IWASAKI, Hiroshi*	Head of PF Instrumentation Division, KEK
Prof. KASUYA, Tadao	Faculty of Science, Tohoku University
Prof. KATSUBE, Yukiteru	Institute for Protein Research, Osaka University
Prof. KIKUTA, Seishi	Faculty of Engineering, University of Tokyo
Prof. KITAMURA, Hideo	PF Light Source Division, KEK
Prof. KOBAYAKAWA, Hisashi	Head of PF Light Source Division, KEK
Prof. KOBAYASHI, Masanori	PF Light Source Division, KEK
Prof. KURODA, Haruo**	Faculty of Science, University of Tokyo
Prof. MATSUSHITA, Tadashi	PF Instrumentation Division, KEK
Prof. NAKAHARA, Kazuo	PF Injector Linac Division, KEK
Prof. OHTA, Toshiaki	Faculty of Science, Hiroshima University
Prof. SAKABE, Noriyoshi	PF Instrumentation Division, KEK
Prof. SATO, Isamu	PF Injector Linac Division, KEK
Prof. TOKONAMI, Masayasu	Faculty of Science, University of Tokyo
Prof. YAMAKAWA, Tatsuya	PF Light Source Division, KEK

Table 2 Members of Program Advisory Committee * Chairman

Prof. ANDO, Masami*	PF Instrumentation Division, KEK
Prof. ASAMI Akira	Head of PF Injector Linac Division, KEK
Prof. ASHIDA, Tamaichi	Faculty of Engineering, Nagoya University
Prof. HATANO, Yoshihiko	Faculty of Science, Tokyo Institute of Technology
Prof. HIEDA, Kotaro	Faculty of Science, Rikkyo University
Prof. ISHII, Takehiko	Institute for Solid Physics, University of Tokyo
Prof. IWASAKI, Hiroshi	Head of PF Instrumentation Division, KEK
Prof. KIKUTA, Seishi	Faculty of Engineering, University of Tokyo
Prof. KOBAYAKAWA, Hisashi	Head of PF Light Source Division, KEK
Prof. GHOSHI, Youichi	Faculty of Engineering, University of Tokyo
Prof. NIHEI, Yoshimasa	Institute of Industrial Science, University of Tokyo
Prof. OHTA, Toshiaki	Faculty of Science, Hiroshima University
Dr. SHIMOMURA, Osamu	National Institute for Research in Inorganic Materials
Prof. SUGI, Haruo	Faculty of Medicine, Teikyo University
Prof. YOSHIMORI, Akio	Faculty of Engineering science, Osaka University

Table 3 Name list of all staff members at the PF

ABE, Isamu	Tech.	L-CTRL	ABEI@JPNKEKVM
AMEMIYA, Yoshiyuki	Ass. Prof.	I-X	AMEMIYA@JPNKEKVM
ANAMI, Shozo	Ass. Prof.	L-RF	
ANDO, Masami	Prof.	I-X	ANDO@JPNKEKVM
ARAKI, Akira	Tech.	R-MAG	
ASAMI, Akira	Prof.	L-INJ	
ASAOKA, Seiji	Tech.	R-CHNL	
CHIKAWA, Jun"ichi	Prof.	Chief Director	
ENOMOTO, Atsushi	Ass. Prof.	L-ACC	ENOMOTOA@JPNKEKVX
FUKUDA, Shigeki	Ass. Prof.	L-RF	
FURUKAWA, Kazuro	Res. Ass.	L-CTRL	FURUKA@JPNKEKVX
HAGA, Kaiichi	Res. Ass.	R-CTRL	HAGA@JPNKEKVM
HANAKI, Hirofumi	Res. Ass.	L-RF	HANAKI@JPNKEKVX
HONMA, Hiroyuki	Tech.	L-RF	
HORI, Yoichiro	Res. Ass.	R-VAC	
HYODO, Kazuyuki	Res. Ass.	I-X	
IIDA, Atsuo	Ass. Prof.	I-X	
IIJIMA, Hitoshi	Tech.	L-RF	
ISAWA, Masaaki	Ass. Prof.	R-RF	ISAWA@JPNKEKVX
ITO, Kenji	Ass. Prof.	I-VUV	ITO@JPNKEKVM
IWASAKI, Hiroshi	Prof.	I-Director	
IWAZUMI, Toshiaki	Res. Ass.	I-X	
KAKIHARA, Kazuhisa	Tech.	L-ACC	
KAMIKUBOTA, Norihiko	Res. Ass.	L-CTRL	KAMI@JPNKEKVX

KAMIYA, Yukihide	Ass. Prof.	R-MAG	KAMIYA@JPNKEKVM
KANAYA, Noriichi	Res. Ass.	R-CHNL	KANAYA@JPNKEKVM
KATAGIRI, Hiroaki	Tech.	L-RF	
KATSURA, Tomotaro	Ass. Prof.	R-CTRL	KATSURA@JPNKEKVM
KATO, Hiroo	Res. Ass.	I-VUV	
KATO, Masahiro	Res. Ass.	R-MAG	
KAWADA, Hiroshi	Res. Ass.	I-X	
KIKEGAWA, Takumi	Res. Ass.	I-X	KIKEGAWA@JPNKEKVM
KIKUCHI, Takashi	Tech.	I-TECH	
KISHIMOTO, Syunji	Res. Ass.	I-X	KISHIMOTO@JPNKEKVM
KITAJIMA, Yoshinori	Res. Ass.	I-VUV	
KITAMURA, Hideo	Ass. Prof.	R-ID	KITAMURA@JPNKEKVM
KOBAYAKAWA, Hisashi	Prof.	R-RF	
KOBAYASHI, Hitoshi	Ass. Prof.	L-OP	
KOBAYASHI, Katsumi	Ass. Prof.	I-X	KOBAYASI@JPNKEKVM
KOBAYASHI, Masanori	Prof.	R-VAC	
KOIDE, Tsuneharu	Res. Ass.	R-CHNL	
KOSUGE, Takashi	Tech	I-TECH	
KOYAMA, Atsushi	Tech.	I-TECH	
KURIHARA, Toshikazu	Res. Ass.	L-OP	
MAEZAWA, Hideki	Prof.	R-CHNL	MAEZAWAH@JPNKEKVX
MARUYAMA, Tadashi	Tech.	I-TECH	
MATSUSHITA, Tadashi	Prof.	I-X	MATSUS@JPNKEKVM
MIKUNI, Akira	Tech.	I-TECH	
MISHINA, Atsushi	Tech.	R-CTRL	MISHINA@JPNKEKVM
MITSUHASHI, Toshiyuki	Res. Ass.	R-I&W	
MIYAHARA, Tsuneaki	Prof.	I-VUV	MIYAHARA@JPNKEKVM
MORI, Takeharu	Tech.	I-TECH	
NAKAGAWA, Atsushi	Res. Ass.	I-X	NAKAGAWA@JPNKEKVM
NAKAHARA, Kazuo	Prof.	L-CTRL	
NAKAJIMA, Tetsuo	Ass. Prof.	I-X	NAKATETS@JPNKEKVM
NAKAMURA, Kie	Tech.	L-OP	
NAKAMURA, Hajime	Tech.	R-I&W	
NAKAMURA, Norio	Res. Ass.	R-CTRL	
NAKAO, Katsumi	Tech.	L-RF	
NOGAMI, Takashi	Tech.	R-CTRL	
NOMURA, Masaharu	Ass. Prof.	I-X	
OGAWA, Yujiro	Res. Ass.	L-INJ	OGAWA@JPNKEKVX
OHMI, Kazuhito	Res. Ass.	R-I&W	OHMI@JPNKEKVX
OHSAWA, Satoshi	Res. Ass.	L-INJ	OHSAWA@JPNKEKVX
OHSUMI, Kazumasa	Ass. Prof.	I-X	
OKAMOTO, Wataru	Tech.	I-TECH	
OOGOE, Takao	Tech.	L-ACC	
OTAKE, Yuji	Tech.	L-OP	
PAK, Cheol On	Ass. Prof.	R-CTRL	PAK@JPNKEKVM
SAITO, Yoshio	Ass. Prof.	L-RF	
SAITO, Yuuki	Tech.	I-TECH	
SAKABE, Noriyoshi	Prof.	I-X	SAKABE@JPNKEKVM
SAKANAKA, Shyogo	Res. Ass.	R-RF	SAKANAKA@JPNKEKVM
SASAKI, Satoshi	Res. Ass.	I-X	SASAKIS@JPNKEKVM
SATO, Isamu	Prof.	L-ACC	
SATO, Masato	Tech.	I-TECH	
SATO, Yoshihiro	Tech.	R-CTRL	YOSHIHIR@JPNKEKVM
SHIDARA, Tetsuo	Res. Ass.	L-RF	SHIDARA@JPNKEKVM
SHIOYA, Tatsuro	Tech.	L-ID	
TAKIYAMA, Youichi	Tech.	R-VAC	
TANAKA, Ken"ichiro	Ass. Prof.	I-VUV	TANAKA@JPNKEKVM
TOKUMOTO, Shuichi	Tech.	R-RF	
TOYOSHIMA, Akio	Tech.	I-TECH	
UEDA, Akira	Tech.	R-I&W	
URANO, Takao	Res. Ass.	L-OP	
YAGISHITA, Akira	Ass. Prof.	I-VUV	
YAMAGUCHI, Seiya	Res. Ass.	L-RF	
YAMAKAWA, Tatsuya	Prof.	R-I&W	
YAMAMOTO, Shigeru	Res. Ass.	I-X	
YOKOTA, Mitsuhiro	Tech.	L-INJ	
Zhang, Xiao Wei	Res. Ass.	I-X	

Table 4 Annual number of staff & visiting scientists

Position	Department	1978	1979	1980	1981	1982	1983	1984	1985	1986	1987	1988	1989
Chief Director		1	1	1	1	1	1	1	1	1	1	1	1
	Injector Linac	1	2	3	3	3	3	3	3	4	4	4	3
Professor	Light Source	1	4	4	4	4	4	4	3	4	4	4	4
	Instrumentation	0	0	0	1	1	1	1	2	3	4	5	5
Associate	Injector Linac	0	1	1	1	2	2	2	2	1	2	3	5
Professor	Light Source	1	5	4	4	4	3	5	5	3	3	3	5
	Instrumentation	0	0	1	3	4	5	5	8	7	9	7	10
Research	Injector Linac	1	3	4	6	7	8	9	10	11	10	10	9
Associate	Light Source	0	1	4	6	7	7	6	8	9	12	12	9
	Instrumentation	0	0	3	2	7	10	10	10	13	13	14	11
Technical	Injector Linac	0	0	2	3	5	5	6	6	7	8	9	10
Staff	Light Source	3	3	3	4	6	6	6	6	7	7	8	10
	Instrumentation	0	0	0	0	1	2	4	4	8	9	11	10
Visiting	Injector Linac	2	2	2	2	2	2	2	2	2	2	2	2
Scientist	Light Source	2	6	4	4	4	4	4	4	4	4	4	4
	Instrumentation	0	0	6	6	6	6	6	6	6	6	6	6
Total		12	28	42	51	64	69	74	80	90	97	103	104

Table 5 Construction budget (in million yen)

Item	1978	1979	1980	1981	1982
Salary	10	82	179	269	
Injector Linac	245	815	1,456	1,152	
Storage Ring	259	582	792	754	
Instrumentation	30	73	379	822	977
Civil Engineering	868	2,546	4,561	2,529	
Accelerator Operation	0	7	60	177	
Computer Rentals	0	0	34	135	
Cooling system & Electric Plant Operation	0	0	0	60	
Electricity	0	1	26	52	
Miscellaneous	29	95	154	233	126
Total	1,441	4,201	7,641	6,173	1,103

Table 6 PF-Budget in each fiscal year (in million yen)

Item	1982	1983	1984	1985	1986	1987	1988	1989
Salary	402	474	484	510	561	561	642	757
PF Storage Ring (channel, insertion device, etc.)	0	0	0	153	131	647	0	0
PF Experiments	140	153	134	184	190	196	237	341
PF Operation & Maintenance	412	477	552	653	820	907	962	1,078
Computer Rentals	136	135	135	135	136	136	141	145
Positron Source & Electric Plant Operation	0	0	0	41	138	208	258	300
Cooling System & Electric Operation	120	111	124	180	211	214	217	231
Electricity	209	226	257	338	381	331	355	425
PF-Industrial Cooperative Experiments	0	94	84	95	185	166	302	219
AR Construction and Experiments						398	267	334
Miscellaneous	115	134	115	127	162	120	301	298
Total	1,534	1,804	1,885	2,397	2,864	3,884	3,682	4,128

Table 7 Yearly account of beam channels

Fiscal	1981	1982	1983	9184	1985	1986	1987	1988	1989
PF	6	8	8	8	10	12	13	13	15
Institutes	0	0	0	1	1	1	3	4	4
Industry	0	0	1	2	4	4	4	4	4
Total	6	8	9	11	15	17	20	21	23

Table 8 Summary of Operation Schedule in FY 1989 (Apr. 1989 - Mar. 1990) (hours)

Cycle	Linac	PF Ring	User's time	AR Ring	Dedicated to SR
1	1844	1632	1152	1788	0
2	1726	1680	1200	1678	456
3	984	864	624	960	0
Total	4554	4176	2976	4426	456

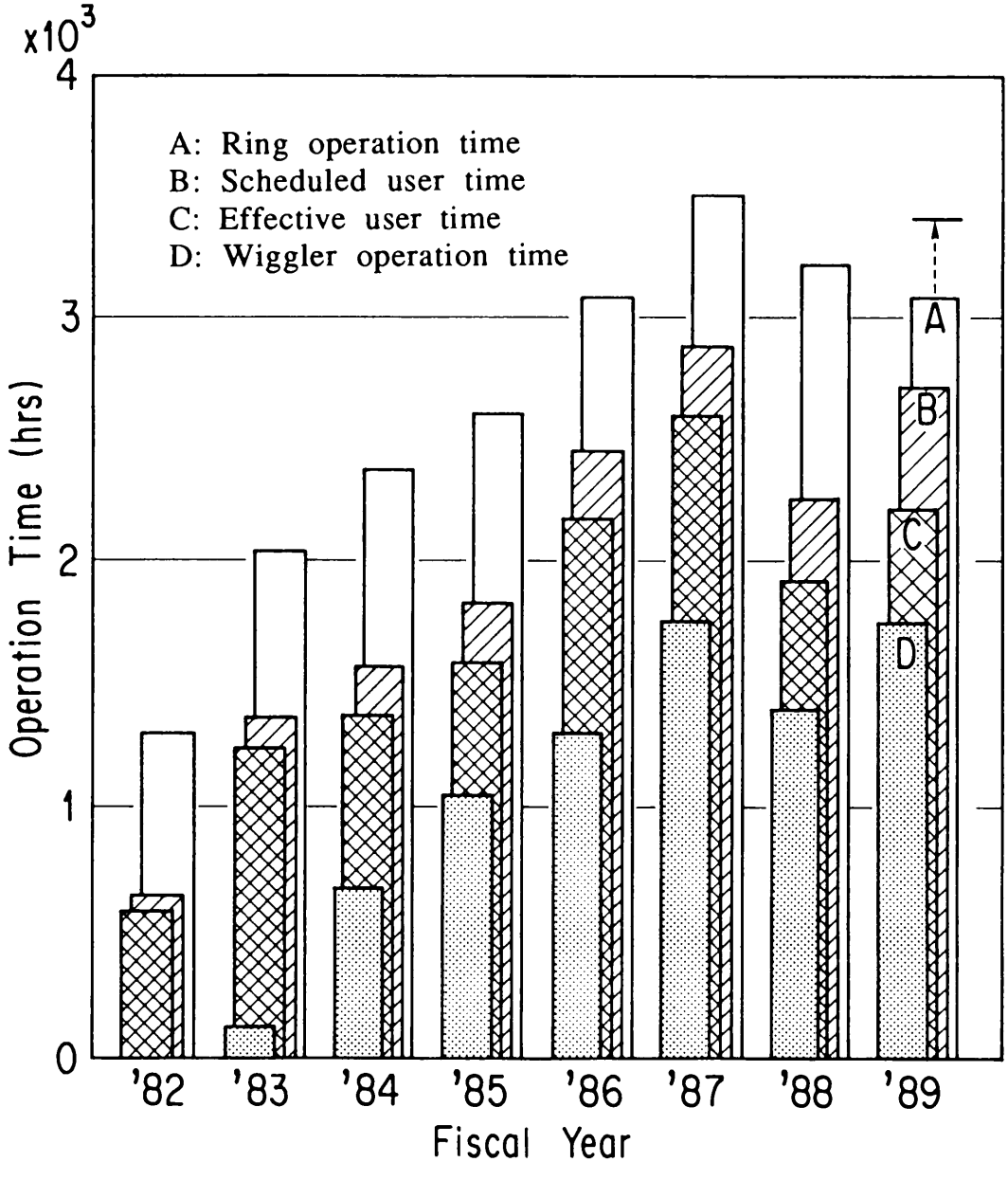

Fig. 4 Ring operation statistics

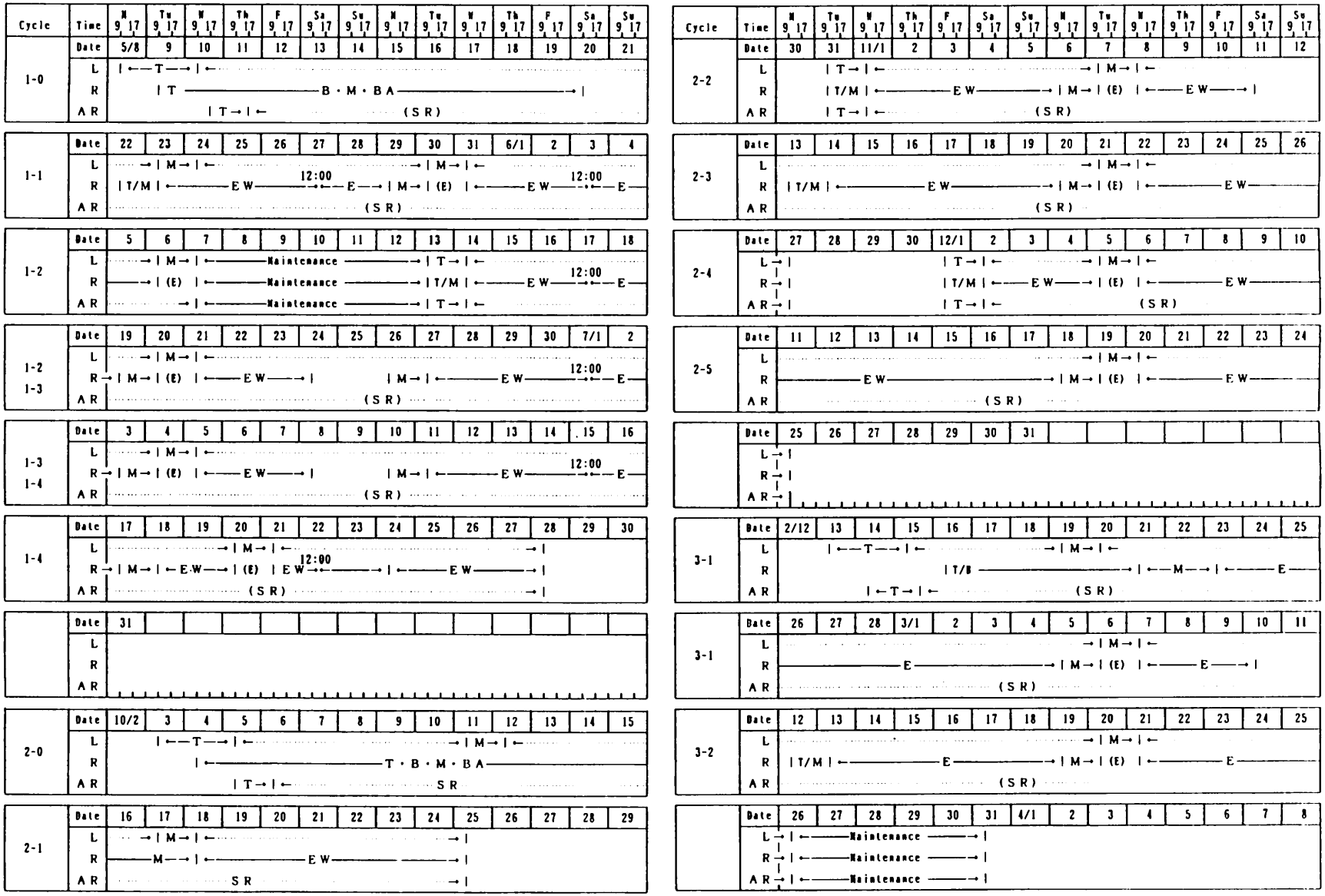

Table 9 Operation Schedule in FY 1989. L: Linac, R: PF Ring, A: Accumulation Ring, T: Machine Tuning, M: Machine Study, E: User's Beam Time without Vertical Wiggler, (E): User's Bonus Time without Vertical Wiggler, EW: User's Beam Time with Vertical wiggler, SR: Dedicated SR Use of AR, (SR): Parastic SR Use of AR, B: Photo-Baking of PF Ring and Beamline, BA: Beamline Alignment.

F. SEMINARS, MEETINGS AND PUBLICATIONS

In FY 1989, twenty one seminars were given by foreign as well as domestic visiting scholars. Meetings were held for an annual symposium and for perspective views of possibilities associated with the future plan. The Factory publishes its quarterly News in Japanese for communication between the users and the staff.

PF seminars

Koide, T. (PF, KEK)
Measurement of Degree of Circular Polarization and BL-28
Feb. 16, 1989

Sato, I. (PF, KEK)
High Brilliance Light Source with CW Linac
March 9, 1989

Fujimito, F. (Osaka Univ.)
Development of Slow Positron Source at the Institute of Scientific and Industrial Research
March 16, 1989

Eland, J.H.D. (Oxford Univ.)
Electron-Electron and Ion-Ion Coincidence Experiments
April 28, 1989

Stöhr, J. (IBM, Almaden Research Center)
Research on Surface of Solid Using NEXAFS
May 17, 1989

Ellis, C. (IFGW-UNICAMP)
1 The Resonant Cavity and the Stimulated Emission of X-ray
2 The Monochromatization of SR by Dynamical Diffraction from Multilayered Crystalline Structure
May 17, 1989

Kovalchuk, M. (Academy of Sciences USSR)
Surface and Interface Structure Investigated by X-ray Standing Wave Method
June 13, 1989

Masujima, T. (Hiroshima univ.)
Perspective of X-ray Photoacoustic Spectroscope
July 25, 1989

Kanazawa, I. (Tokyo Gakugei Univ.)
Generation of Slow Positron with Linac
July 7, 1989

Zhang, X.W. (PF, KEK)
Nuclear Resonance Bragg Scattering Using SR
July 11, 1989

Bordas, J. (Daresbury Lab.)
Synchrotron Radiation Researches in UK
July 27, 1989

Codling, K. (Reading Univ.)
Atomic Molecular Physics
July 27, 1989

Woodruff, D.P. (Univ. of Warwick)
Surface Studies Using SR
August 1, 1989

Zimmermann, P. (Tech. Univ. Berlin)
Photoelectron Spectroscopy on Laser-Excited Aligned Free Atoms
August 4, 1989

West, J. (Daresbury Lab.)
Atomic and Molecular Physics at Daresbury Laboratory
August 4, 1989

Petroff, Y. (LURE)
Recent Experiments at LURE: F.H. Holography High Tc Superconductivity, Clusters
August 8, 1989

Klapper, H. (Tech, Univ. Aachen)
Synchrotron Radiation Topographic Observation of the Para to Ferroelectric Transition of Ammonium Sulphate
September 14, 1989

Iwata, M. (KEK)
Experiments with TRISTAN in Second Phase
October 23, 1989

Nesermann, H. (DESY)
Status of DORIS II
October 18, 1989

Kanna, K.K. (Bhabha Atomic Research Center)
Structure Function and During Interaction of Carbonic Anhydrase
November 22, 1989

Nakanishi, T. (Nagoya Univ.)
Development of Polarized Electron Source
December 19, 1989

Kosarev, E.L. (Institute for Physical Problems)
Experimental Physics Inverse Problems
December 19, 1989

Meetings

Design Meeting on the Beam Line of AR-NE3. I
March 26, 1989

Workshop on Circularly Polarized SR in the VUV and SX region
June 30, 1989

Meeting for Protein Crystallography
August 30-31, 1989

Workshop on Soft X-ray and Ultrasoft X-ray Radiation Biology
September 7-8, 1989

Design Meeting on the Beam Line of AR-NE3. II
November 1, 1989

Design Meeting on the Beam Line of AR-NE3. III
December 1, 1989

Workshop on Small Angle X-ray Scattering
December 8-9, 1989

7th Photon Factory Symposium
February 6-7, 1990

Publications

PHOTON FACTORY NEWS ISSN 0916-0604 Vol.7, No.1-4

Table 10 Number of Proposals approved by PAC.

Research Field	1983	1984	1985	1986	1987	1988	1989
(A) EXAFS	42	26	35	40	61	66	57
(B) Biology	18	18	28	28	32	38	57
(C) X-Ray	24	29	75	54	73	65	61
(D) VUV & Soft X-Ray	19	12	27	26	28	28	36
Total	103	85	165	148	194	197	211

G. GRADUATE UNIVERSITY FOR ADVANCED STUDIES

A new national graduate university has been established in 1988. It has the following three schools:

School of Cultural Studies
School of Mathematical and Physical Sciences
School of Life Sciences.

National Laboratory for High Energy Physics has participated in the University to form the department of Synchrotron Radiation Science and the department of Accelerator Science, both of which belong to the School of Mathematical and Physical Sciences.

Students in the department of Synchrotron Radiation Science are expected to study the basic theory of emission of synchrotron radiation, its characteristics and interaction of radiation with matter, and then engage in research by using various kinds of the facilities in the Photon Factory. The research field includes the development of radiation sources, optical elements and instruments for diffraction, scattering spectroscopy and irradiation experiments as well as the exploration of new areas of applying radiation to science and technology. The students are expected to play an important role in the future development of the synchrotron radiation science in Japan.

Four young men have entered the department of Synchrotron Radiation Science as the first students. They will be given the degree of philosophy after three years.

List of proposals Accepted in Fiscal 1989

Proposal Number	Spokesperson	Title
89-001	T. Matsushita Photon Factory, National Laboratory for High Energy Physics	Development of time-resolved dispersive X-ray absorption spectrometer using imaging plate
89-002	T. Mukoyama Institute for Chemical Research, Kyoto Univ.	One-photon multi-electron excitation process in X-ray absorption spectra
89-003	M. Misono Faculty of Engineering, Univ. of Tokyo	EXAFS and XANES analyses of supported vanadium oxide thin film catalysts prepared by CVD
89-004	T. Miyanaga Faculty of Science, Hirosaki Univ.	Temperature dependence of the Debye-Waller factor in EXAFS of polynuclear metal complexes
89-005	K. Otsuka Institute of Materials Science, Univ. of Tsukuba	Study of premartensitic phenomena in Cu-Al-Ni by EXAFS
89-006	Y. Iwasawa Faculty of Science, Univ. of Tokyo	A direct determination of the structure of the active site in SiO_2-attached niobium acid one-atomic layer catalysts by means of difference EXAFS spectroscopy
89-007	Y. Iwasawa Faculty of Science, Univ. of Tokyo	EXAFS and XANES studies on a noble metal-support interaction on Pt/Nb_2O_5
89-008	N. Toshima Faculty of Engineering, Univ. of Tokyo	Studies on the structure of the metal complex immobilized on the polymeric resin
89-009	H. Maeda Faculty of Science, Okayama Univ.	Development of modulated EXAFS method and its application to structure determination of excited state
89-010	K. Oki Interdisciplinary Graduate School of Engineering Science, Kyushu Univ.	Valence fluctuation of Ce and physical anomalies in Pd-Ce alloys
89-011	R. F. Howe Chemistry Department, Univ. of Auckland	EXAFS studies of metal clusters in zeolites
89-012	H. Hattori Faculty of Science, Hokkaido Univ.	Structural analysis of antimony complex on solid superacid catalysts by means of EXAFS
89-013	H. Hattori Faculty of Science, Hokkaido Univ.	EXAFS study on the structure of the surface species of supported tantalum oxide
89-014	T. Kawashima Department of Chemistry, Univ. of Tsukuba	Structural studies of copper(II)-aminocarboxylate complexes in aqueous solution by EXAFS
89-015	T. Kawashima Department of Chemistry, Univ. of Tsukuba	An EXAFS study of Cr(III, IV, V)-edta complexes in aqueous solution
89-016	Y. Iwasawa Faculty of Science, Univ. of Tokyo	Attached Ru_6 carbide anion cluster-static and dynamic structure analysis under reaction condition

89-017	Y. Iwasawa Faculty of Science Univ. of Tokyo	In-situ EXAFS studies on the structure of the actue-site for CO dissociation on the rare-earth metal oxide-supported metal particle induced by H_2
89-018	Y. Iwasawa Faculty of Science Univ. of Tokyo	A dynamic EXAFS study on the photocatalytic process of the attached Mo oxide
89-019	H. Kuroda Faculty of Science, Univ. of Tokyo	EXAFS of zeolite-supported Co-Rh bimetallic calalysts
89-020	N. Toshima Faculty of Engineering, Univ. of Tokyo	The structure of bimetallic colloidal catalysts
89-021	M. Abe Faculty of Science, Tokyo Institute of Technology	The study of adsorption state of transition metal ions in synthetic inorganic ion exchangers
89-022	M. Okuno Faculty of Science, Kanazawa Univ.	EXAFS studies on the structures of SiO_2 glasses containing alkali earth metals and their crystallizations
89-023	S. Yano Faculty of Science, Nara Women's Univ.	Accumulation and transformation of biologically important compounds by the Co-operative effects of metal ions and amines
89-024	Y. Yoshikawa Faculty of Science, Okayama Univ.	EXAFS studies on oxide films on metal fine-particles
89-025	M. Inoue Faculty of Science, Hiroshima Univ.	EXAFS and XANES studies on intercalation compounds M_xTiS_2 (M = Mn, Fe, Co, Ni)
89-026	M. Hidaka Faculty of Science, Kyushu Univ.	Structural phase transitions on layer compounds ABF_4 using EXAFS
89-027	K. Segawa Faculty of Science and Technology, Sophia Univ.	EXAFS studies of MoO_3/TiO_2 catalyst prepared by an equilibrium adsorption method
89-028	T. Yamaguchi Faculty of Science, Fukuoka Univ.	EXAFS and XANES studies of transition-metal sugar complexes
89-029	M. Nomura Photon Factory, National Laboratory for High Energy Physics	Applicability of X-ray absorption spectroscopy to analytical chemistry
89-030	Y. Huahui Department of Chemistry, Xiamen Univ.	EXAFS studies of synthetic nitrogenase FeMo-cofactor model compounds and Mo-Fe-S cluster complexes
89-032	T. Ohta Faculty of Science, Hiroshima Univ.	Temperature dependent EXAFS studies on $AgBr_xI_{1-x}$ and $AgBr_xCl_{1-x}$ mixed crystals
89-033	Y. Kai Faculty of Engineering, Osaka Univ.	X-ray crystal structure analysis of carboxylases

89-034	I. Tanaka Faculty of Science, Hokkaido Univ.	Structure analysis of ribosomal protein from extreme thermophile
89-035	M. Konno Faculty of Science, Ochanomizu Univ.	Crystal structure analysis for Mn superoxide dismutase
89-036	K. Fukuyama Faculty of Science, Osaka Univ.	X-ray crystallographic analysis of heat-labile enterotoxin
89-037	M. Kusunoki Institute of Protein Research, Osaka Univ.	X-ray crystal analysis of α-amylase, β-amylase and α-amylase inhibitor
89-038	Y. Hata Institute for Protein Research, Osaka Univ.	Dynamical studies of enzymic reaction in crystal
89-039	T. Tsukihara Faculty of Engineering, Tottori Univ.	Crystal structural analysis of spherical viruses
89-040	N. Sakabe Photon Factory, National Laboratory for High Energy Physics	Development of time resolved laue method for protein crystallography
89-041	N. Sakabe Photon Factory, National Laboratory for High Energy Physics	X-ray structure analysis of DPI using weissenberg camera for protein crystallography
89-042	N. Sakabe Photon Factory, National Laboratory for High Energy Physics	Improvement of data collection system using weissenberg camera for protein crystallography and its application study
89-043	A. E. Yonath Weixmann Institute & Max Planck Institute MPG	Crystal structure analysis of ribosomal particles from bacterial sources
89-044	N. Yasuoka Basic Research Laboratory, Himeji Institute of Technology	Multi-wavelength anomalous diffraction studies of ferredoxins
89-045	S. Yoshikawa Basic Research Laboratory, Himeji Institute of Technology	X-ray crystal structural analysis of bovine heart cytochrome c oxcidare
89-046	K.K. Kannan Neutron Physics Division, Bhabha Atomic Research Center	Structure and function of human carbonic anhydrase I. The structure and refinement at 1.5 A resolution
89-047	Y. Izumi Faculty of Science, Hokkaido Univ.	Structural study of activation mechanism of enzyme by calmodulin
89-048	K. Kajiwara Faculty of Engineering and Design, Kyoto Institute of Technology	Gelation of casein micelles as observed by small-angle X-ray scattering
89-049	T. Ueki Faculty of Engineering Science, Osaka Univ.	Solution X-ray scattering study on proteins with a dumbbell-shape

9-050	Y. Inoko Faculty of Engineering Science, Osaka Univ.	Small-angle X-ray scattering studies of isolated linker and core histones
89-051	Y. Inoko Faculty of Engineering Science, Osaka Univ.	Improvement of "SAXES" and development of data treatment software II
89-052	N. Matsushima School of Allied Health Professions, Sapporo Medical College	Solution X-ray scattering of S-100 proteins
89-053	D. M. Engelman Molecular Biophysics & Biochemistry, Yale Univ.	Solution scattering studies on folding/ unfolding of mutants of staphylococcal nuclease
89-054	D. M. Engelman Molecular Biophysics & Biochemistry, Yale Univ.	Interaction of 1, 2, 3-heptanetriol with non-ionic detergent micelles
89-055	K. Kobayashi Photon Factory, National Laboratory for High Energy Physics	Study on the degradation products of amino acid irradiated with monochromatic soft X-rays
89-056	K. Hieda Faculty of Science, Rikkyo Univ.	Analysis of products of oligonucleotides by K-shell ionization of phosphorus
89-057	J. L. Smith Department of Biological Sciences, Purdue Univ.	Collection of Multiwavelength anomalous diffraction data from crystals of glutamine amidotransferase
89-058	I. Matsubara Tohoku Univ., School of Medicine	Delay of tension development after molecular changes at the onset of contraction
89-059	N. Yagi Tohoku Univ., School of Medicine	X-ray diffraction study of skeletal muscles during unloaded shorting
89-060	I. Hatta Faculty of Engineering, Nagoya Univ.	Studies on phase transition and structure of phospholipid by X-ray diffraction
89-061	S. Takemori The Jikei Univ., School of Medical	X-ray diffraction of skinned skeletal muscle under the inhibitory effect of butanedione monoxime.
89-062	T. Hamanaka Faculty of Engineering Science, Osaka Univ.	Structural studies of visual cell membrane by X-ray diffraction
89-063	K. Wakabayashi Faculty of Engineering Science, Osaka Univ.	Dynamical X-ray diffraction studies on structural changes of thin (actin) filaments during muscle contraction
89-064	H. Sugi School of Medicine, Teikyo Univ.	Dynamic X-ray diffraction studies on the contracting chemically-modified skinned fibers of rabbit skeletal muscle
89-065	M. Akisada Institute of Clinical Medicine, Univ. of Tsukuba	Intravenous coronary arteriography by synchrotron radiation
89-066	I. Abe Institute of Clinical Medicine, Univ. of Tsukuba	SR diagnosis of lymphography and soft tissue tumor

89-067	S. Hasegawa Department of Electronics, Univ. of Electronics-Communication	Development of imaging system for medical diagonis using SR
89-068	K. Nishimura Saitama Medical School	Development of high speed aquisition system for energy differential image of coronary arteries
89-069	S. Kikuta Faculty of Engineering, Univ. of Tokyo	Structural analysis of metal-silicon interface by X-ray
89-070	I. Nakai Department of Chemistry, Univ. of Tsukuba	Chemical stae imaging of earth and planetary minerals by selectively induced X-ray fluorescence analysis
89-071	Y. Gohshi Faculty of Engineering, Univ. of Tokyo	Development of a scanning X-ray microprobe with synchrotron radiation
89-072	K. Sakurai National Research Institute for Metals	Near-surface analysis of metals using grazing incidence X-ray spectrometry
89-073	M. Ohmasa Institute of Materials Science, Univ. of Tsukuba	Characterization of sintered silicon nitrides
89-074	K. Koto Tokushima Univ.	X-ray powder diffraction pattern of the oriented thin film
89-075	R. Uno College of Humanities and Science, Nihon Univ.	Analysis of orientational distribution of powder in powder diffractometry using synchrotron radiation
89-076	K. Ohsumi Photon Factory, National Laboratory for High Energy Physics	Development of structure analysis of submicrometer-sized crystal
89-077	K. Ohsumi Photon Factory, National Laboratory for High Energy Physics	Standardization of powder diffraction study by using SR
89-078	M. Miyamoto College of Arts and Science, Univ. of Tokyo	Characterization of micro-sized vapor-growth diamonds by the laue method
89-079	S. Hashimoto The Research Institute for Iron, Steel and Other Metals, Tohoku Univ.	Approach to non-periodic atomic arrangements in ternary alloy crystals and quasi-crystals with use of X-ray anomalous scattering effect
89-080	S. Hashimoto The Research Institute for Iron, Steel and Other Metals, Tohoku Univ.	Low temperature phase diagram of Fe-Ni alloys
89-081	K. Otsuka Institute of Materials Science, Univ. of Tsukuba	Study of premartensite in Ni-Al by X-ray dittraction
89-082	Y. Matsuo Faculty of Science Nara Women's Univ.	X-ray diffuse scattering study of premartensitic Transition
89-083	H. Masiyama Faculty of Science, Yamaguchi Univ.	Appearance of superstructure in ferroelectrics at lower temperature below the incommensurate-commensurate transition

89-084	N. Tsukuda Research Institute for Applied Mechanics, Kyushu Univ.	Depth dependence of lattice parameter of InAs on GaAs
89-085	Y. Soejima Faculty of Science, Kyushu Univ.	Superstructure determination using X-ray anomalous dispersions
89-086	T. Matsushita Photon Factory, National Laboratory for High Energy Physics	Study of two dimensional structure of langmuir and langmuir-blodgett films
89-087	D. F. McMorrow Department of Physics, Univ. of Edinburgh	Diffuse scattering in $KAlF_4$ showing a planar elastic instability and in $SrTiO_3$ and $RbCaF_3$ undergoing an antiferrodistortive transition
89-088	T. Izumi Faculty of Engineering, Chubu Univ.	An effect of a synchrotron irradiation on high Tc superconductors
89-089	M. Ohmasa Institute of Materials Science, Univ. of Tsukuba	In situ observation of neucleation of dehydration products
89-090	T. Takahashi The Institute for Solid State Physics, Univ. of Tokyo	Surface structure analyses of semiconductor crystals by X-ray diffraction
89-091	Y. Udagawa Institute for Molecular Science	A study of X-ray raman scattering
89-092	Y. Satow Faculty of Pharmaceutical Science, Univ. of Tokyo	Methodological studies on short-wavelength X-ray diffraction data collection and structure analyses utilizing horizontal-type four-circle diffractometer
89-093	S. Kikuta Faculty of Engineering, Univ. of Tokyo	Nuclear resonant bragg scattering by synchrotron radiation
89-094	K. Nakayama National Research Laboratory of Metrology	Lens action of asymmetric diffraction
89-095	T. Hondoh Faculty of Engineering, Hokkaido Univ.	Measurements of dislocation velosities in ice at a temperature close to the melting point
89-096	T. Mukoyama Institute for Chemical Research, Kyoto univ.	Nuclear excitation by synchrotron radiation
89-097	O. Shimomura National Institute for Research in Inorganic Materials	In-situ observation of graphite-hexagonal diamond transition at high temperature and pressure
89-098	T. Yamasaki Himeji Institute of Technology	SAXS study of hydrogen absorption and desorption in some amorphous alloys
89-099	K. Namikawa Department of Physics, Tokyo Gakugei Univ.	A spin resolved vacant state spectroscopy by means of X-ray resonance magnetic scattering
89-100	H. Yamazaki Faculty of Science, Okayama Univ.	Magnetic X-ray scattering studies on magnetic structure of the $R_2Fe_{14}B$ compounds

89-101	T. Ishikawa Faculty of Engineering, Univ. of Tokyo	Generation of coherent X-rays by means of flat crystal optics
89-102	T. Ishikawa Faculty of Engineering, Univ. of Tokyo	R&D studies of high performance X-ray optics for next generation SR
89-103	K. Namikawa Tokyo Gakugei Univ.	X-ray parametric frequency conversion
89-104	R.J. Nelmes Department of Physics, Univ. Edinburgh	P-T dependence of spontaneous strain in $PbTiO_3$
89-106	Y. Nannichi Institute of Materials Science, Univ. of Tsukuba	Synchrotron radiation studies of electronic structure and surface chemistry of the sulfide-treated GaAs
89-107	S. Aoki Institute of Applied Physics, Univ. of Tsukuba	Study of real time imaging with a soft X-ray microscope
89-108	T. Koizumi Faculty of Science, Rikkyo Univ.	Multiple-photoionization of alkali and alkaline-earth atoms by inner-shell excitation
89-109	Y. Sato Research Institute for Scientific Measurements, Tohoku Univ.	Photodissociation of methyl-compounds of group II and III metals by core-level excitation
89-110	M. Yanagihara Research Institute for Scientific Measurements, Tohoku Univ.	Optical constants of superthin films for soft X-rays and multilayer coatings
89-111	T. Ohta Faculty of Science,, Hiroshima Univ.	XANES study of carbon films synthesized by chemical vapour deposition
89-112	Y. Kihara Jichi Medical School	Development of X-ray zooming tube for X-ray microscope. Evaluation of photoemission surface characteristics
89-113	T. Nagata Department of Science and Technology, Meisei Univ.	Multiple photoionization of rare earth atoms due to photoexcitation of a 4d-shell electron
89-114	Y. Kondo Faculty of Engineering, Tohoku Univ.	Relaxation of soft X-ray excitation in ionic crystals
89-115	Y. Sakisaka Faculty of Science, Kyoto Univ.	Angle-resolved photoemission spectroscopy of H-, Xe-, CO- and N_2-adsorbed Fe(110) surfaces at 80 K
89-116	D. Xunmin Physics Department, Fudan Univ.	Electronic surface properties of MBE-Crown $Al_xGa_{1-x}As$ crystals
89-117	N. Kouchi Faculty of Science, Tokyo Institute of Technology	Absolute photoabsorption cross sections and photoionization quantum yields of silicon, germanium, and carbon compounds
89-118	K. Yoshino Harvard-Smithonian Center for Astrophysics	High resolution spectroscopic study and measurement of absolute photoabsorption coefficients of molecules of astrophysical and atmospheric importance

89-119	K. Kaneko Faculty of Science, Chiba Univ.	Structural polymorphism of metal oxides formed in micropores
89-120	K. Oda Faculty of Engineering, Univ. of Tokyo	Local atomic configurations in Fe-M-C (M:Al, Mn, Ni) fcc γ-phase
89-121	Y. Morikawa Research Laboratory of Resources Utilization, Tokyo Institute of Technology	Structure of active sites in metal ion-exchanged layered clay minerals
89-122	S. Yoshida Faculty of Engineering, Kyoto Univ.	An EXAFS study on the structures of V-Ti composite oxides prepared by CVD method
89-123	T. Murata Faculty of Education, Kyoto Univ. of Education	Development of optical EXAFS and its application to lattice relaxation of impurity in crystals
89-124	I. Watanabe Faculty of Science, Osaka Univ.	Solvent effects on the electronic state and structure of anionic complexes by X-ray absorption spectroscopy
89-125	M. Takahashi Institute of Scientific and Industrial Research, Osaka Univ.	X-ray spectroscopic investigation on local structure and electronic structure of transition metal nitride solid solutions (MoN-MN (M=Nb, Zr, Ti), Cu_3N-TiN)
89-126	T. Yamaguchi Faculty of Science, Hokkaido Univ.	Crystallization process of ZrO_2 thin film overlayer on SiO_2
89-127	M. Ichikawa Catalysis Research Center Hokkaido Univ.	Characterization of RhIr bimetallic clusters in Zeolite by EXAFS
89-128	H. Arashi Research Institute for Scientific Measurements, Tohoku Univ.	Studies for micro-structure of hydrous zirconia particles by using EXAFS method
89-129	H. Arashi Research Institute for Scientific Measuremtens, Tohoku Univ.	Studies of valence state in oxide electrodes by using XANES method
89-130	M. Nasu Faculty of Education, Yamaguchi Univ.	EXAFS study on solid state amorphization process of Fe-C alloy
89-131	K. Ozutumi Department of Chemistry, Univ. of Tsukuba	Structure of Cadmium(II)-thiocyanato complexes in DMSO, DMF, and aqueous solutions
89-132	H. Kuroda Faculty of Science, Univ. of Tokyo	EXAFS study of metal carbonyl clusters photochemically grafted on silica
89-133	M. Abe Faculty of Science, Tokyo Institute of Technology	The study of adsorption state of transition metal ions in synthetic inorganic ion exchangers
89-134	H. Kawazoe Faculty of Engineering, Tokyo Institute of Technology	Coordination of In in a- and c-In_2Se_3 thin films
89-136	T. Fukushima Faculty of Engineering, Yokohama National Univ.	Preparation of ultrafine particles of gold on supports

89-137	H. Endo Faculty of Science, Kyoto Univ.	Chemical short range order of liquid selenium mixture containing halogen
89-138	Y. Okamoto Faculty of Engineering Science, Osaka Univ.	Local structure of highly active and highly dispersed Mo-sulfide catalysts from $Mo(Co)_6$ prepared
89-141	H. Yamazaki Faculty of Science, Okayama Univ.	Polarization dependent EXAFS measurement on oxide superconductors uniaxially oriented by magnetic field
89-142	T. Yoshikawa Faculty of Science, Okayama Univ.	Local crystal structure of oxide films on metal fine-particles
89-143	K. Tamura College of Integrated Science, Hiroshima Univ.	Local structure of fluid selenium
89-144	K. Mizuno College of Integrated Science, Tokushima Univ.	XANES and EXAFS of $YBa_2Cu_3O_{7-\delta}$ partially substituted by Sn
89-145	Y. Kou Lanzhou Institute of Chemistry, Academia Sinica	EXAFS studies of immobilized metal clusters
89-146	K. Asakura Faculty of Science, Univ. of Tokyo	Dynamic studies on the asymmetric synthesis in chiral crystal by means of EXAFS
89-147	J. S. Chung Pohang Institute of Science and Technology, POSTEC	An EXAFS characterization of iron clusters in zeolite
89-148	H. Mori School of Medicine, Tokai Univ.	Quantitation and 2-dimensional imaging of organ blood flow with nonradioactive microspheres
89-149	H. Yoshida Faculty of Science, Tohoku Univ.	X-ray structure analysis of RNase F_1 using Weissenberg camera for protein crystallography
89-150	K. Murakami Univ. of Tsukuba	X-ray analysis of recombinant human renin
89-151	K. Nakamura Faculty of Pharmaceutical, Univ. of Tokyo	Crystal structure determination of microbial ribonucleases
89-152	S. Aibara Research Institute for Food Science, Kyoto Univ.	X-ray crystallography of protein crystals prepared under the microgravity
89-153	B. Mikami Research Institute for Food Science, Kyoto Univ.	X-ray crystal structure analysis of β-amylase
89-154	M. Hidaka Faculty of Science, Kyushu Univ.	Structural property of modified lysozymes
89-155	N. Hirayama College of Science and Technology, Yokohama City Univ.	X-ray diffraction experiments of single crystals of human granulocyte colony stimulating factor

89-156	T. Higuchi Faculty of Science, Osaka City Univ.	Crystal structure analyses of aminotransferases and their mutants from microorganisms
89-157	P. M. Colman CSIRO	Antigen-antibody interactions
89-158	P. M. Colman CSIRO	Seed storage protein structure and engineering
89-159	P. M. Colman CSIRO	Plant virus structure and function
89-160	M. Hidaka Faculty of Science, Kyushu Univ.	Structural properties of proteins in a solution and membrane
89-161	K. Tanaka Faculty of Dentistry Nagasaki Univ.	Conformational studies of osteocalcin by X-ray small angle scattering
89-162	N. Matsushima School of Allied Health Professions, Sapporo Medical College	Fractal structure of biological materials
89-163	K. Kobayashi Photon Factory, National Laboratory for High Energy Physics	Product analysis of inner shell ionized amino acids using high performance liquid chromatograph
89-164	K. Kobayashi Photon Factory, National Laboratory for High Energy Physics	Quantitative analysis of DNA double strand breaks as a result of inner shell ionization of constituent atoms
89-165	Y. Satow Faculty of Pharmaceutical Science, Univ. of Tokyo	Development of the multi-exposure oscillation method for protein crystallography
89-166	Y. Satow Faculty of Pharmaceutical Science, Univ. of Tokyo	High-resolution crystal structure analysis of an amylase inhibitor, haim
89-167	T. Takeda Institute of Clinical Medicine, Univ. of Tsukuba	Angiography of small animals by iodine filter method
89-168	S. Komura College of Integrated Science, Hiroshima Univ.	Time resolved small-angle X-ray scattering study of dynamical structure of lipid bilayer
89-169	I. Nakai Department of Chemistry Univ. of Tsukuba	Nondestructive X-ray analyses of archaeological samples
89-170	Y. Gohshi Faculty of Engineering, Univ. of Tokyo	Surface analysis using the critical take off angle of X-ray fluorescence
89-171	A. Iida Photon Factory, National Laboratory for High Energy Physics	Wavelength dispersive X-ray fluorescence analysis
89-172	K. Kato National Chemical Laboratory for Industry	Imaging of layerd materials by correlation photoacoustics and simultaneous measurement of photoacoustic and florescence spectra

89-173	F. Marumo Research Laboratory of Engineering Materials, Tokyo Institute of Technology	Structure determination of $MgSo_4 \cdot 5MgO \cdot 8H_2O$ by means of ultramicro-single-crystal X-ray diffraction
89-174	T. Yamanaka College of General Education, Osaka Univ.	Kinetics of the pressure induced phase transition by means of energy dispersive diffractometry
89-175	H. Mashiyama Faculty of Science, Yamaguchi Univ.	Appearance of superstructure in ferroelectrics at lower temperature below the incommensurate-commensurate transition
89-176	M. Sakata Faculty of Engineering, Nagoya Univ.	A study of density distribution of crystals by powder diffraction
89-178	N. Kojima Faculty of Science, Kyoto Univ.	Low temperature and high pressure X-ray study on the crystal structure of low-dimensional metal $K_3Cu_8S_6$
89-179	T. Nakajima Photon Factory, National Laboratory for High Energy Physics	Establishment of the X-ray diffraction methods at very and ultra low temperature and study of the phase transitions
89-180	K. Fukamachi Faculty of Engineering, The Saitama Institute of Technology	A study of anomalous scattering factors used by pendellösung fringes due to X-ray resonant scattering
89-182	Y. Kashiwase College of General Education, Nagoya Univ.	Correlation between X-ray inelastic scattering and dynamical diffraction
89-183	S. Sasaki Photon Factory, National Laboratory for High Energy Physics	Thermal scattering of $SrTiO_3$ from 100 k to room temperature
89-184	K. Tsukimura Geological Survey of Japan	Cation distribution and temperature dependency of Ni ferrite
89-185	S. Kimura National Institute for Research in Inorganic Materials	Small angle scattering from lithium niobate melt
89-186	Y. Chikaura Faculty of Engineering, Kyushu Institute of Technology	Observation of thermal behaviour of microdefects in thinned silicon wafers by means of plane-wave SR topography
89-187	A. Iida Photon Factory, National Laboratory for High Energy Physics	X-ray fluorescence analysis of heavy elements
89-188	Y. Suzuki Faculty of Engineering, Kyushu Institute of Technology	Satellite diffraction topography of semiconductor superlattices
89-189	M. Kamimoto Electrotechnical Laboratory	Study on the melting and solidification processes of high temperature latent thermal energy storage materials
89-190	N. Kojima Faculty of Science, Kyoto Univ.	Low temperature and high pressure X-ray study on the crystal structure of $Cs_2Au_2X_6$ (X=Cl, Br, I)

89-191	H. Iwasaki Photon Factory, National Laboratory for High Energy Physics	Dynamical study of recrystallization process of "grain oriented 3% silicon steel" by synchrotron radiation
89-192	K. Osamura Faculty of Engineering, Kyoto Univ.	Dynamical structure change of Al based alloys during phase decomposition and reversion
89-193	K. Osamura Faculty of Engineering, Kyoto Univ.	SR-SAXS experiments on the compositional fluctuation in alloy semiconductors
89-194	P. K. Gyung	In situ topographic observation of crack tip propagation
89-195	M. Ando Photon Factory, National Laboratory for High Energy Physics	Characterization of X-ray and soft X-ray optical elements with monochromatic synchrotron radiation
89-196	A. Iida Photon Factory, National Laboratory for High Energy Physics	Soft X-ray fluorescence spectrometry using undulator radiation
89-197	T. Miyahara Photon Factory, National Laboratory for High Energy Physics	3dXPS and 3d resonant XPS on heavy rare-earth alloys and compounds
89-198	A. Yagishita Photon Factory, National Laboratory for High Energy Physics	Resonance Auger spectra of rare-gas atoms and simple molecules
89-199	S. Suga Institute for Solid State Physics, Univ. of Tokyo	3d core spectroscopy of lahthanide monopnictides
89-200	S. Yasumi Teikyo Univ	Studies on the m-shell of the dysprosium atom using monochromatic X-rays for determining the mass of the electron neutrino
89-201	S. Sato Faculty of Science, Tohoku Univ.	High-energy-resolved soft X-ray spectroscopy of electron-doped high-Tc superconductors
89-202	S. Nakai Faculty of Engineering, Utsunomiya Univ.	2PXPS and 3d resonant XPS of 3d transition-metal compounds
89-203	T. Hanyu Faculty of Science, Tokyo Metropolitan Univ.	Angular dependency of photoelectric yield spectra from rare earth metals and their compounds
89-204	N. Miyamoto Research Institute of Electrical Communication, Tohoku Univ.	Surface cleaning of semiconductor using synchrotron radiation
89-205	N. Yamaguchi Plasma Research Center, Univ of Tsukuba	Characterization of X-ray detectors for plasma diagnostics
89-206	S. Nakai Faculty of Engineering, Utsunomiya Univ.	XPS study of 3d levels in heavy rare-earth valence fluctuation compounds

89-207	N. Miyamoto Research Institute of Electrical Communication, Tohoku Univ.	Epitaxial thin film growth using synchrotron radiation
89-208	H. Fukutani Institute of Physics, Univ. of Tsukuba	Stress optical studies of alkali and alkaline-earth halides
89-209	H. Fukutani Institute of Physics, Univ. of Tsukuba	Development, characterization and applications of polarizers in the VUV, SX region
89-210	T. Koide Photon Factory, National Laboratory for High Energy Physics	Magnetic-circular-dichroism study of the electronic states of transition metal and rare earth compounds
89-211	A. Misu Faculty of Science, Science Univ. of Tokyo	Magneto-optical effects of high Tc superconductors VUV
89-212	H. Kawazoe Faculty of Engineering, Tokyo Institute of Technology	Chemical bonding state of SiO_2/Si interface
89-213	Y. Sakisaka Faculty of Science, Kyoto Univ.	Angle-resolved photoemission spectroscopy of high-Tc superconducting $Nd_{2-x}Ce_xCuO_4$(001) single-crystal thin films
89-214	N. Ueno Faculty of Engineering, Chiba Univ.	Photon energy dependence of the photochemical decomposition of polymer films
89-215	Y. Morioka Institute of Physics, Univ. of Tsukuba	The study of threshold electron spectra of clusters
89-216	Y. Morioka Institute of Physics, Univ. of Tsukuba	The study of high resolution absorption spectra of $^{16}O_2$ and $^{18}O_2$
89-217	K. Ito Photon Factory, National Laboratory for High Energy Physics	Measurements of high-resolution photoabsorption spectrum of H_2
89-218	A. Kawazu Faculty of Engineering, Univ. of Tokyo	Study of surface electronic structure on (BEDT-TTF)2[Cu(NCS)2] by angle-resolved UPS
89-Y001	H. Asahina Mitsubishi Petro Chemical Co.	XAS study of metal phthalocyanine
89-Y002	H. Asahina Mitsubishi Petro Chemical Co.	XAS study of etyleneoxide catalysis
89-Y003	K. Ueda Center Research Laboratory, Hitachi Ltd.	Development of angiographic system using iodine filter method
89-Y004	T. Hisatsugu Fujitsu Laboratories Ltd.	Exposure tests by synchrotron radiation in BL-17A and BL-17C
89-Y005	K. Mochiji Center research Laboratory, Hitachi Ltd.	Photochemical reactions on semiconductor surface by synchrotron radiation
89-Y006	Y. Koike Mitsubishi Kasei Corp.	The EXAFS study of catalysts

89-Y007	K. Hayakawa Advance Research Laboratory, Hitachi Ltd.	BL-8A; Soft X-ray diffractometry, B; Noise level reduction of the B line optics and silicon EXAFS experiments, C; X-ray digital radiography, lithography and microprobe experiments
89-Y008	S. Maeyama NTT Applied Electronics Laboratory	EXAFS measurements on high-Tc superconducting materials
89-Y009	J. Matsui Fundamental Research Laboratory, NEC Corp.	X-ray optics, X-ray lithography and photo-chemical reaction experiments
89-Y010	S. Kawado Research Center, Sony Co.	Grazing incidence X-ray fluorescence analysis of metal contamination on Si surfaces
89-Y011	C. Uemura Applied Electronics Laboratory, NTT	Analysis, lithography and photo-reaction using SR
89-Y012	K. Tani Richo Co., Ltd.	Measurements of EXAFS on As_2Se_3 thin films
89-Y013	T. Hisatsugu Fujitsu Laboratories Ltd.	Exposure tests by synchrotron radiation in BL-17A and BL-17C
89-Y014	J. Matsui Fundamental Research Laboratory, NEC Corp.	X-ray optics, X-ray lithography and photo-chemical reaction experiments
89-Y015	A. Nakano Center Research Laboratory, Hitachi Ltd.	BL-8A; Soft X-ray diffraction, B; Silicon EXAFS experiments, total refection measurement, C; X-ray digital radiography, lithography and microprobe experiments
89-Y016	Y. Koike Mitsubishi Kasei Corp.	The EXAFS study of catalysts and thin films
89-Y017	K. Ueda Center Research Laboratory, Hitachi Ltd.	Development of angiographic system using iodine filter method
89-Y018	T. Takyu Central Research Laboratories Idemitsu Kohsan Co. Ltd.	An EXAFS study of platinum, iron gallium on zeolite
89-Y019	K. Ohshima Mitsui Toatsu Chemicals Inc.	EXAFS of supported metallic or metal-oxide catalysts
89-Y020	T. Kawamura Applied Electron Laboratory, NTT	Analyses of hetero-epi film interface by X-ray standing wave
89-Y021	T. Okada Tosho Corporation	EXAFS study of copper ion-exchanged zeolites
89-Y022	H. Hashimoto Toray Research Center	Total reflection X-ray fluorescence spectrometry for thin film analyses
89-Y023	T. Hisatsugu Fujitsu Laboratories Ltd.	Exposure tests by synchrotron radiation in BL-17A, BL-17B and BL-17C
89-C001	M. Matsumoto Mecanical Engineering Research Laboratory, Hitachi Ltd.	Photodesorption from stainless steel, aluminum alloy and oxygen free copper test chambers
89-C002	T. Kitano Central Research Laboratoris, NEC Corp.	Characterization of semiconductor materials by high precision X-ray optics

89-C003	N. Yoshioka LSI Research & Development Laboratory, Mitsubishi Electric Corp.	Industrial application of soft X-ray spectroscopy
89-C004	T. Ito Fujitsu Laboratories Ltd.	Study of new method in vapor-phase epitaxial growth using synchrotron radiation
89-C005	S. Yasuami Research & Development Center, Toshiba Corp.	Characterization of semiconductor materials using soft X-ray EXAFS and X-ray diffraction
89-C006	T. Ohtsubo Nippon Steel Corp.	Dynamic observation of materials processing by synchrotron radiation
89-C007	S. Suzuki Tsukuba Research Center, Sanyo Electric Co., Ltd.	Micro pattering by synchrotron radiation
89-C008	S. Kawado Research Center, Sony Corp.	Development of ultrafast X-ray detector system
89-C009	H. Ayato Research Laboratories, Ashigara, Fuji Photo Film Co., Ltd.	Structurul analysis of halogen compound by EXAFS method with SR
89-C010	Y. Muramatsu Applied Electronics Laboratories, NTT	Monochromator technologies for highly brilliant insertion device radiation
89-C011	A. Aoki Engineering Research Center, NKK Corp.	Structure analysis of Ion-implanted materials
89-C012	T. Takigawa ULSI Research Center, Toshiba Corp.	Study of new technique in synchrotron radiation processing of semiconductor materials
89-C013	K. Kawashima Electronics & Control Systems R&D Laboratory, Nippon Steel Corp.	Development of a high-resolution CT imaging system using the high energy X-rays
89-C014	H. Hashimoto Toray Research Center	Fluorescence EXAFS spectrometer for soft X-ray region
89-C015	T. Mochizuki Division of Nuclear Power Plant, NKK Corp.	Development of a beamline for high brilliance quasi-monochromatic X-rays
89-C016	M. Funabashi Research Development Corp. of Japan	Study of photochemical processes on surfaces using synchrotron radiation
89-C017	H. Nagata Research development Corp. of Japan	Analytical studies on fabricated surfaces using synchrotron radiation
89-C018	T. Kojima Takatsuki Research Laboratory, Sumitomo Chemical Co., Ltd.	Dynamic structure of synthetic polymer materials using X-ray small angle scattering
89-019	Y. Fukuda Canon Research Center, Canon Inc.	Studies on the optical properties of focusing multilayer soft X-ray mirrors
89-C020	T. Yagi Development Center, Konica Corp.	Structure analysis of halogen compound by powder diffraction method with synchrotron radiation
89-C021	K. Konashi Power Reactor and Nuclear Fuel Development Corp.	Basic study for development of high intensity CW electron accelerator

Y: approved for charged beam time,
C: Collaborations between the Photon Factory and institutes of private companies.

Injector Linac Division

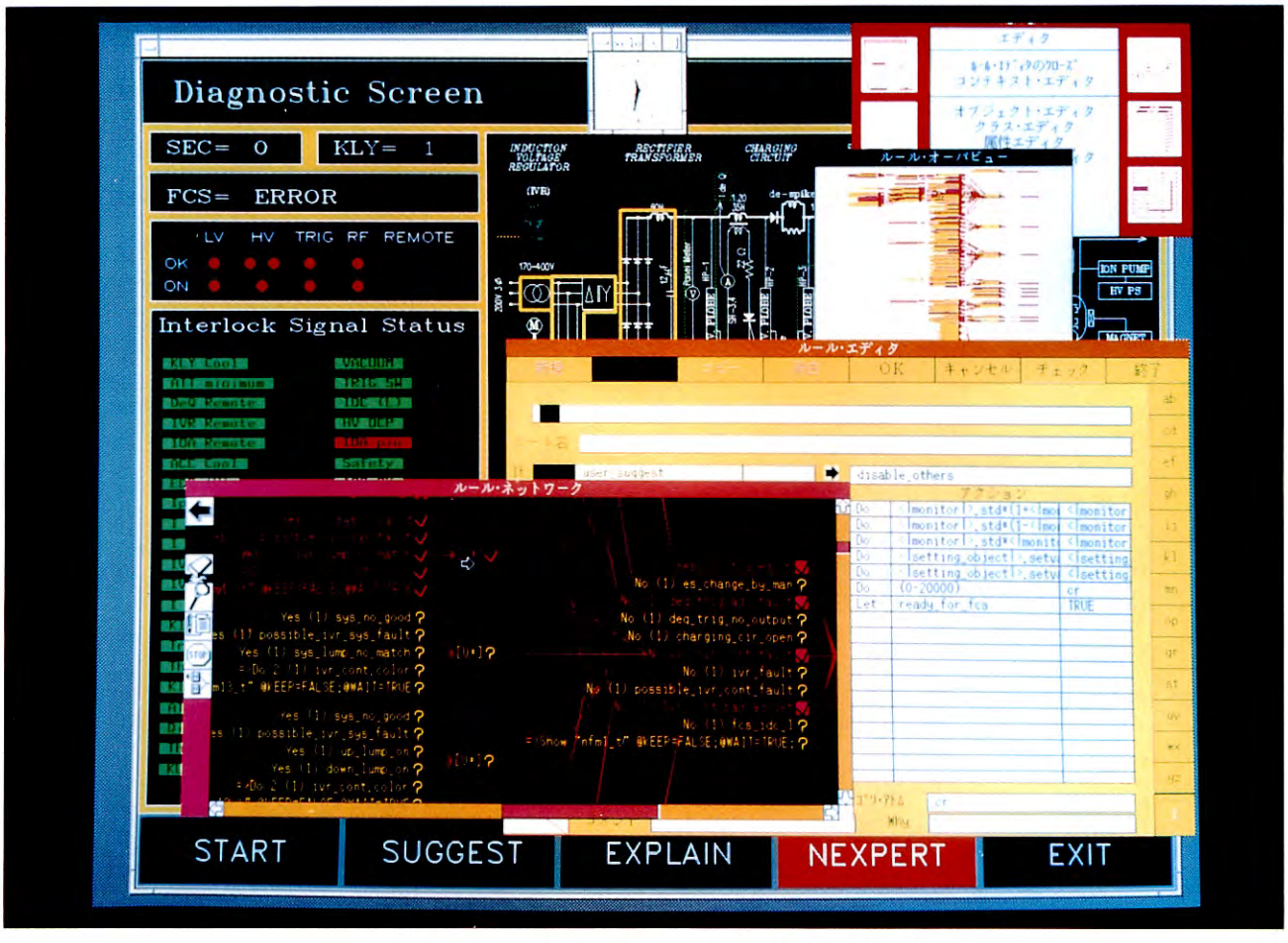

Expert system for klystron modulator trouble shooting

INJECTOR LINAC DIVISION

A. INTRODUCTION

Following the last period (October 1987 - September 1988) the operation time of the PF linac has further been increased, now exceeding 5,200 hours, as described later in detail (B. Operation). It was about 4,500 hours during the last period, an increase of as much as 700 hours, corresponding to a 15 % increase. In spite of this large increase, the operation rate was improved from 95 to 97 %. This high rate is the result of continual efforts made to improve various instruments of the linac. In the following, these improvements made during this period (October 1988 - September 1989) are briefly described first; then presented is research carried out by the Linac Division.

In recent years the PF ring group requested the linac group to supply them with positrons for their routine synchrotron-radiation research. Considering the increasing demand for more positrons from TRISTAN and PF, a new electron-gun system has been developed with a cathode-grid assembly (EIMAC Y-796). The electron gun of the positron generator must have the ability to emit a very high current with a reasonable emittance, and a reasonably long lifetime as well. The new gun was installed in October, 1988. With this system and other improvements in associated equipment, positron injection into the PF ring was remarkably improved. The injection rate remained at ~ 0.05 mA/s during very early stage, but gradually increased; finally, in June 1989, it reached ~ 0.4 mA/s. Furthermore, the gun has not shown any deterioration after use for nearly one year.

Construction of beam analyzing and monitoring systems has continued and is nearly completed. Energy analysis of the beam is now possible at four locations along the accelerator. The beam currents are monitored simultaneously at various locations, and the beam profiles are more easily measurable. In addition, monitors of the rf system have been prepared, and variation is more easily and widely detected for rf phase and power.

In addition to the development of these new analyzers and monitors, significant developments and improvements have also been made on the control system of the linac by introducing a CATV system and an additional network (Ethernet) for man-machine interface enhancement. The DS-Link and beam-switching systems were also improved. With both these developments and improvements regarding tuning, trouble-shooting has become much easier than before, serving to increase the reliability of the linac.

When it comes to increasing the linac reliability, the most effective factor may be an improvement in the main high-power klystrons. As described in the last issue of this report, six new klystrons with barium-impregnated cathodes were test used and showed promising characteristics. Since then, six klystrons of the same type were added during FY 1988, and another eighteen during FY 1989. All of them showed much improved characteristics: the occurrence of arcing around the cathode assembly appreciably decreased, and the resulting deterioration of the klystron frequently experienced with the old type has become much less. This epoch-making improvement served to make the daily operation of the linac considerably easier.

With the improvement of the klystrons it was noticed that the high voltage to be applied to the klystron could not be raised sufficiently high, because the PFN capacitors of the klystron modulators could not stand this voltage. Therefore, new capacitors which have a much higher working voltage have been designed and fabricated; replacement of the old-type capacitors is now under way with the new ones.

As for research in the Linac Division, two subjects should be mentioned first. Both were recently started: one involves a beam acceleration experiment with a wakefield caused by high-intensity electrons in plasma; the other involves the channeling of high-energy positrons through a single-crystal. Though both are still in the preliminary stage, some promising results have already been obtained in the former experiment.

For research of an advanced accelerator, it is important to have a suitable facility; for this reason a plan exists to build a new small linac, Test Linac. Most of the design work has been finished, and its construction is to start shortly. Some major subjects to be investigated are the production and acceleration of beams with high brightness, such as with an rf gun or high gradient acceleration.

A. Asami

B. OPERATION

During this period, the linac has been successfully and stably operated with a total operation time of 5244 hours. The beam-monitoring system mentioned in the last issue has been useful for trouble shooting and for tuning of the linac, and has contributed to a high operation rate. Operation statistics for this period are listed in Table 1. As a special case, the maintenance time scheduled at the beginning of FY 1988 was shortened by 9 days during December and January to increase the integrated luminosity of TRISTAN experiments.

Twenty klystrons were replaced during this period. Fifteen of them had failed owing to internal arcing. The other five were returned from the klystron gallery to the klystron test shop for retesting. Three of them were installed again and are being used.

The operational performance during the last five years and the averaged fault rate during these seven years are shown in Tables 2 and 3, respectively. As described in the last issue, klystrons with barium-impregnated (BI) cathodes

have been introduced into the linac. When klystrons with oxide cathodes failed, they were replaced with these newly developed types. Twenty-four, just half the total number of klystrons with BI cathodes were being operated at the end of July 1989. These new klystrons have a very low fault rate (improved averaged, as shown in Table 3).

After a vacuum leak accident of the P4 accelerator guide related to a breakdown of the pulsed-focusing coil at the positron production target, arcing in the accelerator guide rapidly increased. Replacement of this accelerator guide with an improved one is being prepared.

H. Kobayashi

Table 1. Operation and failure time of each cycle.

Term-cycle	Date	Operation time (minutes)	Failure time (minutes)	Operation rate (percent)
FY 1988				
2-1	Oct. 7 - Oct. 26	27360	182	99.3
2-2	Nov. 7 - Nov. 28	34620	3042	91.2
2-3	Dec. 1 - Dec. 28	39360	1128	97.1
3-1	Jan. 5 - Jan. 14	57600	2850	95.1
3-2	Feb. 17 - Feb. 20	45060	624	98.6
FY 1989				
1-0	May 8 - May 22	20160	285	98.6
1-1	May 22 - June 7	23040	815	96.5
1-2	June 13 - June 25	18420	190	99.0
1-3	June 26 - July 10	19680	394	98.0
1-4	July 10 - July 31	29350	99	99.7
total		314650 (5244 hours)	9609	96.9

Table 2. Cumulative usage hours of klystrons during the past years.

Period	Total	Unused	Failed		Living		MTBF
	No. of tubes	No. of tubes	No. of tubes	Mean age (hours)	No. of tubes	Av.op.time (hours)	(hours)
up to July 1985	79	2	28	3600	49	6200	13400
up to July 1986	91	3	39	4400	49	7400	13100
up to July 1987	106	4	52	4400	50	9600	13600
up to July 1988	120	2	67	4500	51	11400	13500
up to July 1989	140	5	82	6400	53	12400	14400

Table 3. Averaged fault rate and averaged applied voltage to klystrons.

Period	Fault rate (/day·tube)	Applied voltage (average) (kV)	Total operation (tube-days)
Aug. 1982-July 1983	2.5	238	4470
Aug. 1983-July 1984	1.6	242	4150
Aug. 1984-July 1985	1.2	240	4420
Aug. 1985-July 1986	1.0	238	5600
Aug. 1986-July 1987	1.0	239	7740
Aug. 1987-July 1988	1.0	240	9990
Aug. 1988-July 1989	0.6	241	10510

C. PROGRESS AND IMPROVEMENTS

1. INJECTION SYSTEM

1a. Installation of a New Gun

A new-type electron gun was installed in the positron generator during September 1988, and is now in operation. It has a dispenser-type cathode with the advantage that the emission current is not very sensitive to residual gas in the vacuum. It has been utilized for more than one year without changing the cathode. The variation of the gun anode current is shown in Fig. 1 for the 4-ns beam of TRISTAN. The current has been stable during the long term, as can be seen in Fig. 1. This indicates that the lifetime of the cathode is sufficiently long in practical use. The operational conditions have been fixed during the term, except for a change of the bias voltage between the grid and cathode. The gun

has been operated at a cathode voltage of -160 kV. The heater power of the gun and the pulse voltage between the grid and cathode have been kept constant. The vacuum pressure in the gun has been kept in the range of 1.1-1.6 $\times 10^{-7}$ Pa.

S. Ohsawa

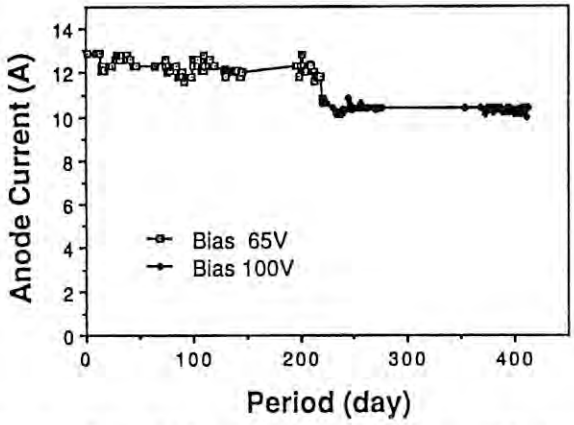

Fig. 1. Gun anode current variation with time. The current is that of the 4-ns beam of TRISTAN. The periods without data are for scheduled maintenance.

2. MICROWAVE SOURCE

2a. Operational Performance of an Improved Klystron with a Barium-Impregnated Cathode

Up until July 1987, 106 klystrons (tubes) had been cumulatively used in the klystron gallery as the microwave source of the PF linac (Table 2). All of them had oxide-barium cathodes, and 52 had failed up to then. The cause of failures was mostly internal arcing. The mean age of the failed tubes was 4,500 hours and the MTBF (mean time before failure) was about 13,000 hours. Therefore, nearly half the number of tubes installed in the gallery (total socket number is 48) had to be replaced by new ones every year (the total operation time during one year is about 10,000 tube-days). During these years, research on the internal arcing phenomena and the improvement of tubes had been made (Photon Factory Activity Reports #6, 1988). A failed klystron was opened in order to inspect the cathode-anode assembly. The results indicated that both the anodes and focusing electrodes of the electron gun were heavily contaminated with barium compounds evaporated from the cathode surface and that it was likely to be a cause of tube arcing. A new type of tube with a barium-impregnated (BI) cathode had been developed. This cathode, also called a dispenser cathode, can be prefired so as to evaporate any excess barium compound from the cathode material before installing it in the tube; consequently, electrode contamination is expected to be reduced.

During FY 1987 and 1988, 27 tubes with the BI cathode have been produced and 24 of them had been installed in the klystron gallery by July 1989. In Table 4, the cumulative status of klystrons corresponding to the year of production is summarized. The total operation time of oxide-cathode tubes is about 1,070,000 tube-hours and the number of failed tubes is 82; therefore, the MTBF of an oxide-cathode tube is about 13,000 hours. On the contrary, no BI cathode tubes have failed during an operation time of 115,000 tube-hours, up to July 1989. If this operation (115,000 tube-hours) were carried out only with oxide-cathode tubes instead of BI cathode tubes, at last 8 tubes (115,000 tube-hours/13,000 hours) would have failed. The result shows that the BI cathode tubes have a noticeably longer MTBF than that of the oxide-cathode tubes. As shown in Table 5, the averaged fault rate of BI cathode tubes is much smaller (0.27/day·tube) than that of oxide-cathode tubes (1.21/day·tube) for operation up to July 1989. During the operation period of Aug. 1988-July 1989 the fault counts ratio of BI cathode tubes to all tubes was less than 18%, while the contribution by those tubes to the total operation was nearly 40% (Fig. 2). Consequently, the applied voltage to the BI tubes can be increased to 244 kV (Table 5). From these statistical results it can be concluded that the improved klystron with a BI cathode has a longer life and a lower fault rate than those of the oxide-cathode klystron.

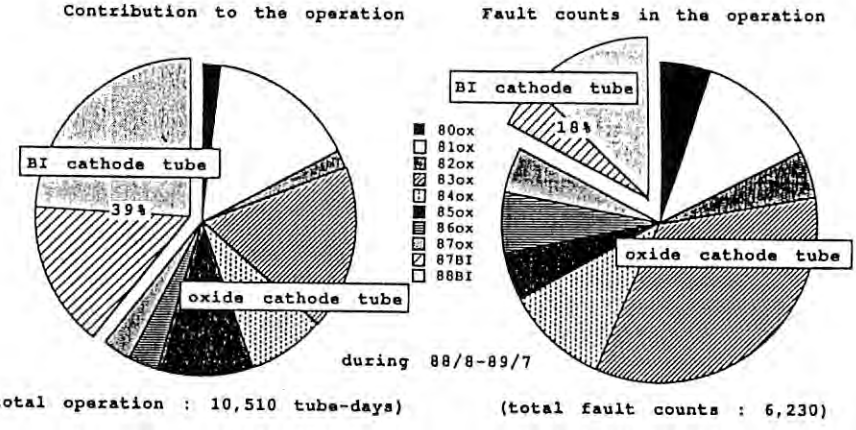

Fig. 2. Contribution of BI cathode tubes to the total operation and fault count ratio of BI cathode tubes to the total fault count for the operation period during Aug.1988-July 1989.

Table 4. Cumulative status of klystrons up to July 1989 corresponding to the year of production. Unused tubes are those which have never been used in the klystron gallery. STB (Standby) tubes are those which have been used in the gallery and can be used there again.

Year of production	Cathode	Total	Unused	Living					Failed					Cumulative operation	MTBF
		No. of tubes	No. of tubes	No. of tubes	(STB	working e^-	working e^+)	Av.op.time (hours)	No. of tubes	Causes (arcing	windows	others)	Mean age (hours)	(tube-hours)	(hours)
1979	oxide	4	0	0	(0	0	0)	———	4	(2	1	1)	3900	15600	3900
1980	oxide	20	0	2	(1	1	0)	15000	18	(10	5	3)	7900	172800	9600
1981	oxide	20	0	8	(1	7	0)	24500	12	(8	2	2)	7400	284100	23700
1982	oxide	9	0	2	(1	1	0)	13300	7	(4	2	1)	7800	80800	11500
1983	oxide	13	0	7	(1	6	0)	21400	6	(5	1	0)	11600	219600	36600
1984	oxide	13	1	3	(0	3	0)	14900	9	(9	0	0)	6400	102400	11400
1985	oxide	12	1	5	(0	5	0)	15300	6	(6	0	0)	4800	105000	17500
1986	oxide	15	0	2	(1	1	0)	9800	13	(13	0	0)	3000	59000	4500
1987	oxide	7	0	0	(0	0	0)	———	7	(5	1	1)	4300	30400	4300
	BI	7	0	7	(0	6	1)	7400	0	(0	0	0)	———	51900	———
1988	BI	20	3	17	(0	11	6)	3700	0	(0	0	0)	———	62700	———
	oxide	113	2	29	(5	24	0)	18700	82	(62	12	8)	6400	1069700	13000
	BI	27	3	24	(0	17	7)	4800	0	(0	0	0)	———	114600	———
	total	140	5	53	(5	41	7)	12400	82	(62	12	8)	6400	1184300	14400

Table 5. Fault rate and applied voltage of oxide-cathode and BI cathode tubes during each one-year operation period.

Period	Fault rate (/day·tube)		Applied voltage (kV)		Total operation (tube-days)	
	oxide	BI	Oxide	BI	oxide	BI
Aug. 1982-July 1983	2.5	---	238	---	4470	---
Aug. 1983-July 1984	1.6	---	242	---	4150	---
Aug. 1984-July 1985	1.2	---	240	---	4420	---
Aug. 1985-July 1986	1.0	---	238	---	5600	---
Aug. 1986-July 1987	1.0	---	239	---	7740	---
Aug. 1987-July 1988	1.03	0.28	238	239	9290	710
Aug. 1988-July 1989	0.79	0.27	238	244	6460	4060
total (up to July 1989)	1.21	0.27	239	244	42120	4770

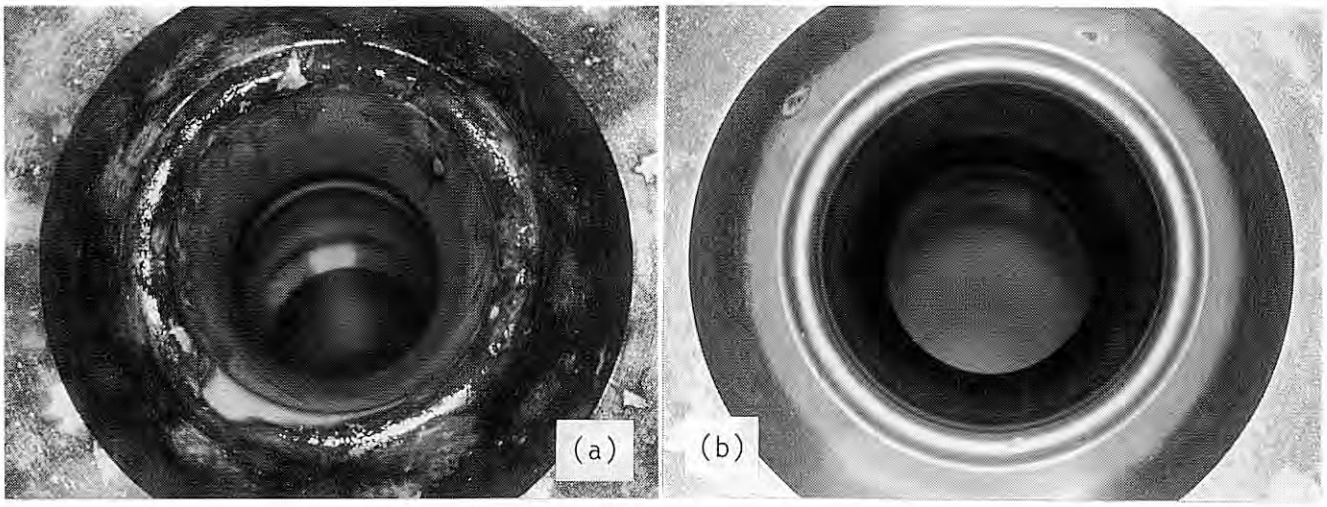

Fig. 3. Anode electrode contamination of oxide (a) and BI (b) cathode tubes, whose experienced hours of high voltage are about one hundred and several hundred, respectively.

The electrode contamination of a BI cathode tube which had been operated for several hundred hours in the klystron gallery was observed. In Fig. 3, the anode electrode of this tube is shown compared with that of the oxide-cathode tube which had only been experienced by the initial high-voltage conditioning of about one hundred hours after tube production. Despite the longer operation time of the BI cathode tube, the anode electrode is distinctively less contaminated than that of the oxide-cathode tube. The amount of x-ray radiation from the direction of the electron-gun assembly in the BI cathode tube under operation was also observed to be still lower, even after several thousand hours operation, while the gun assembly area of the oxide-cathode tubes increasingly radiate x-rays with the operation time. Since x-ray radiation is considered to be caused by the electron bombardment on the anode electrode, and these electrons are most likely emitted from the focus electrode contaminated by the barium compounds, the contamination of not only the anode but also the focus electrode of the BI cathode tube would not be accumulated with the operation time. Therefore, it is ascertained that the internal arcing of the oxide-cathode klystron is due to electrode contamination by barium compounds and that the lower fault rate of the BI cathode tube is due to the less contamination (taking into account operational statistics).

Y. Saito

2b. Remedy for PFN capacitors

1) Introduction

Some of the capacitors in the pulse-forming network (PFN; 20 sections) for the klystron modulators had begun to break down since 1986. There are 48 klystron modulators in the PF linac (including the positron generator), and a total of 960 capacitors. The number of breakdowns corresponds to 2.5% of all capacitors. Once a breakdown occurs, it has great effect on linac operation. It was therefore necessary to solve this problem as soon as possible. In this report, an outline of investigation of the breakdown and development of a new-type capacitor is described.

2) The long-term variation of tanδ

The tanδ and insulation resistance of all capacitors have been measured regularly every year since 1982 when the PF linac operation started. The dielectric loss factor (tanδ) is a good parameter to investigate deterioration of capacitors. The initial value of the tanδ was 0.01% on the average. Figure 4 shows the tanδ data (the maximum, the minimum, and the average values of twenty capacitors of each modulator) measured in 1987. We can divide all the capacitors into two groups in terms of the

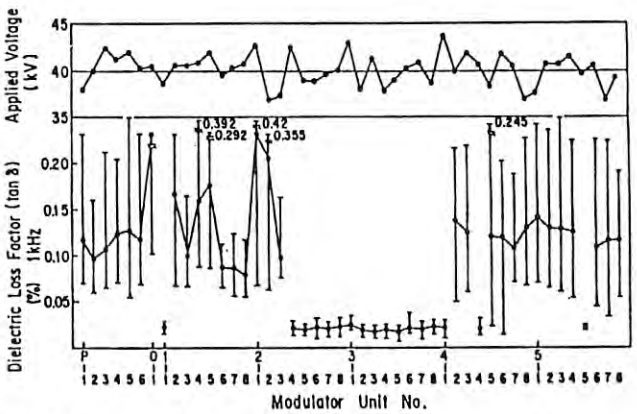

Fig. 4. The maximum, the minimum and the average tanδ values of twenty capacitors and the applied voltage for each modulator.

large difference in the measured values. In one group (group 1 in Table 6), they exhibit a great increment of tanδ. In the other group (group 2 in Table 6), they exhibit no deterioration. All of the capacitors which have broken down belong to the former group. Since there is no difference among the applied voltages for the two groups of capacitors, capacitor breakdown seems to be due to individual capacitors.

3) The results of an investigation regarding breakdown

To determine the cause of breakdown, the same number of capacitors from both groups were opened and investigated. Table 6 shows the characteristics of the samples. The following facts were found for both groups:

1. The insulating oil was not fully aromatic. (It is said that olefinic polymer (polypropylene) can easily swell unless it is used in fully aromatic insulating oil.)
2. The corona starting voltage (CSV) of elements is very close to the rated voltage.
3. Line scratches along the electrode edge are observed in the dielectric (polypropylene). (The dielectric consists of a sheet of mica paper and two polypropylene films which are located just next to the electrodes.)
4. During dc breakdown tests of the capacitor elements, almost all breakdowns occurred at the edge region, as shown in Fig. 5.
5. The dc breakdown voltage (DCBDV) of elements depends on the accumulated operation time.

Judging from these facts, it was found that the region of the dielectric which is right next to the electrode edge had gradually deteriorated due to a corona discharge in both the group-1 and group-2 capacitors. (The difference of characteristics between two groups is not so large as shown in Fig. 4). Therefore, all of the capacitors in the linac should be replaced by newly designed capacitors in order to prevent future breakdowns.

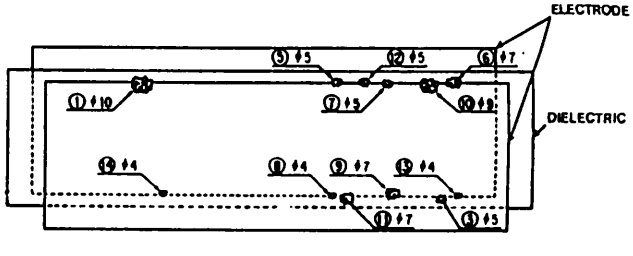

Fig. 5. Accumulated locations of 15 elements where dc breakdown occurred. The numbers in circles indicate the element number.

4) Acceleration tests of the life span for a newly designed capacitor

Acceleration tests in which a voltage higher than the rated voltage was applied (but, of course, it was lower than the breakdown voltage) were performed at klystron modulators in the PF linac in order to design a new capacitor. Table 7 shows the test condition and

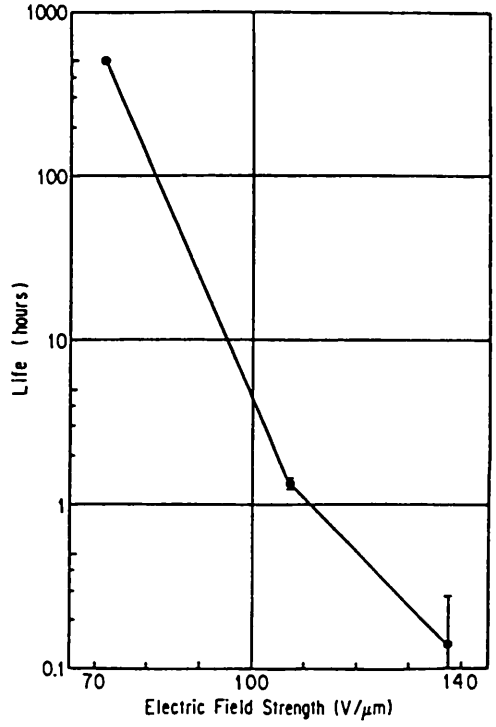

Fig. 6. Life-span dependence of type-A capacitors on the electric field strength.

results. The first type (type-A) uses mica as a dielectric material and the second type (type-B) uses a low-density paper and polypropylene. For the type-A capacitors (mica), three levels of electric field strength (70, 110 and 140 V/μm) were applied, since mica has a large dielectric strength and is expensive. For type-B capacitors (paper and polypropylene), three-level fields around 60 V/μm were applied according to the result of a preliminary test. Figure 6 shows the dependence of the life span for type-A capacitors on the electric field strength. From a test of type-A capacitors, a voltage acceleration coefficient (n in eq. (1)) of 14.7 was obtained. The acceleration test for type-B capacitors gave a life span of more than 2,500 hours.

The type-B capacitor was adopted for replacement. It was difficult to estimate the shortest life span of type-A capacitors owing to a lack of sufficient test data. Though the tanδ value of the type-B capacitor is larger than that of the old-type capacitor, there is no problem regrading our low-duty operation. The shortest life span (T) can be estimated in terms of E, n and T_0 by the equation:

$$T = T_0 \times E^n \qquad (1)$$

E: the ratio of the electric field strength of the test to the designed value.
n: the voltage acceleration coefficient.
T_0: the shortest life span obtained by the test.

Table 6. Characteristics of sample capacitors and elements.

Group		1					2				
Sample NO.		1-1	2-5(9)	2-5(12)	2-4(10)	2-4(11)	1-4	1-5	1-6	5-6(A)	5-6(B)
Operation time (× 1000 hours)		16	25	25	25	25	14	14	13	21	21
Capacitor	1kHz tanδ (%)	0.03	0.02	0.02	0.03	0.03	0.57	0.18	0.19	0.11	0.09
Characteristics	CSV (kV)	——	>10	>10	>10	>10	——	——	——	>10 (*3.9)	>10 (*3.1)
	clamp ratio(%)	——	101.6	104.3	102.0	101.3	——	——	——	100.4	99.5
Insulating oil	ρ (1kV, Ω·cm)	7.8×10^{13}	2.1×10^{13}	1.6×10^{13}	3.8×10^{13}	4.5×10^{13}	2.4×10^{13}	5.0×10^{13}	2.6×10^{13}	5.6×10^{13}	5.6×10^{13}
characteristics	tanδ (1kV,%)	2.5	2.2	1.5	1.2	1.3	0.3	0.9	1.3	0.8	0.6
Capacitor	1kHz tanδ (%)	——	0.06	——	0.09	——	——	——	——	——	0.21
Element	CSV/Rating voltage	0.9	1.2	1.1	1.2	1.1	1.1	1.2	1.2	1.1	1.0
Characteristics	DC BDV/Rating voltage	6.5	5.5	5.6	5.7	5.1	6.8	6.4	6.2	5.3	5.6

* the value measured at 4°C.

Table 7. Acceleration test conditions and results.

Type		A	B
Dielectric material	electrode side	mica	insulating paper polypropylene
	middle		
Electric field strength (V/mm)		70	57
		110	61
		140	65
Result		voltage acceleration coefficient=14.7	the shortest life span=2,500 hours

By substituting E=1.5, n=15, T_0=2500 for type B, T of a new capacitor becomes more than one million hours. This value is sufficiently long to use them in the PF linac, although its operation has been increased to more than 5,000 hours per year.

From the result of this test, a new type capacitor was fabricated and installed in the klystron modulators. Over 70 % of the PFN capacitors has been replaced by the new type and successfully operated. Figure 7 shows the long-term variation of tanδ of the new- and old-type capacitors. No deterioration of tanδ has been observed up to now.

H. Honma

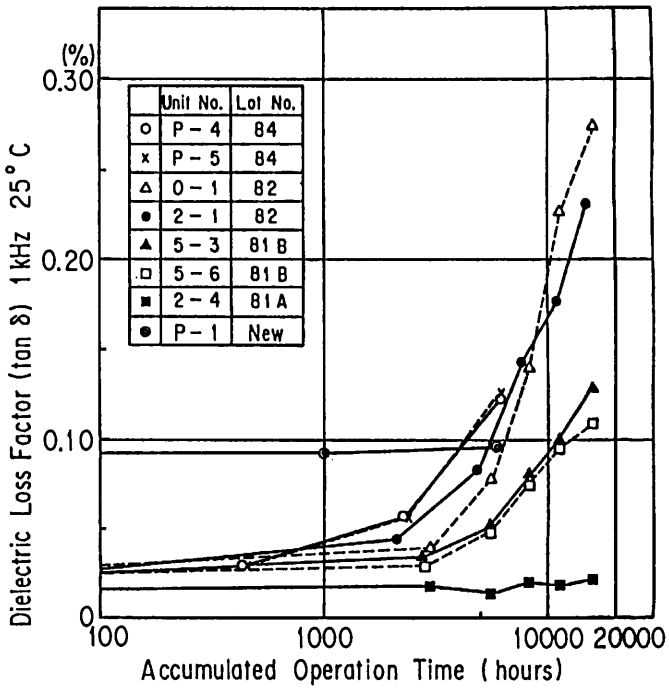

Fig. 7. Long-term variation of tanδ of the new- and old-type capacitors.

3. CONTROL SYSTEM

3a. Main Control Network Extension

The linac is controlled with a distributed processor network comprising nine minicomputers and hundreds of microcomputers. Control messages are interchanged between these computers through fiber-optic ring networks. The main network between minicomputers (MELCOM 70/30) is a 5 Mbit/s fiber-optic ring network (LOOP-I). We have recently had many requests for increased functionality of the control system not included in the original design. Since system resources were inadequate to implement the desired functionality, the system was extended to meet new needs.

Since LOOP-I is specific to the MELCOM 70/30 system, it cannot be extended to other, more modern computers. We thus planned to introduce a standard local-area network. We presently employ the media of Ethernet (IEEE802.3 or ISO8802/3) and the TCP/IP (DARPA) protocol suite for the standard network, because they are flexible and most of their components are commercially available for many kinds of computers.

For communication between the old and new network, gateway programs have been developed on the minicomputer (MELCOM MX3000-II), which was introduced in FY 1988. From the viewpoint of control message compatibility, the paths for control message flow in the old system were extended to the standard network. In this extended system, it becomes possible to send/receive linac control messages to/from any computer. The gateway programs also transfer the data base (control parameters) from the old minicomputer to the gateway computer every second. According to this system enhancement, we can easily connect the control system to others and combine resources.

In the new network the message response time is about 25 ms; the throughput is about 30 kbyte/s. Under heavy traffic conditions there is no noticeable change in performance for up to 200 messages per second. The resultant average response time between an application program in the extended system and a device controller is about 380 ms, including the overhead of LOOP-I (300 ms).

Several computer subsystems have already been connected to the new network: a beam-current monitoring subsystem and a workstation for both program development and communication with a laboratory network. Connections with a large mainframe computer (Fujitsu M780) in the Photon Factory and an expert system for the diagnosis of klystron failure are also planned.

On this basis we have been developing an upper-level control-message protocol using an object-oriented idea in order to allow easier control of accelerator equipment than is now possible. A device name, an action command and a realistic unit in character strings are used in the new message instead of binary address, command and number specifications. A message converter program between old and new message protocols has been developed. The new message protocol is already being used for a part of the magnet control and makes application programs portable and easy regrading maintenance.

K. Furukawa

3b. Improvements in DS-Link

It has been two years since a new console display system (DS-Link) has come into use. The system contains (1) a personal computer network (DS-Link) (2) a broad-band cable television (CATV) system and (3) video processors. All of the personal computers on the DS-Link are FMR-50 and FMR-70 made by Fujitsu Ltd. Ten FMR stations of those are connected with CATV through VP-150-FM video processor. CATV tuners and video processors are controllable through the DS-Link. A block diagram of the network is depicted in Fig. 8.

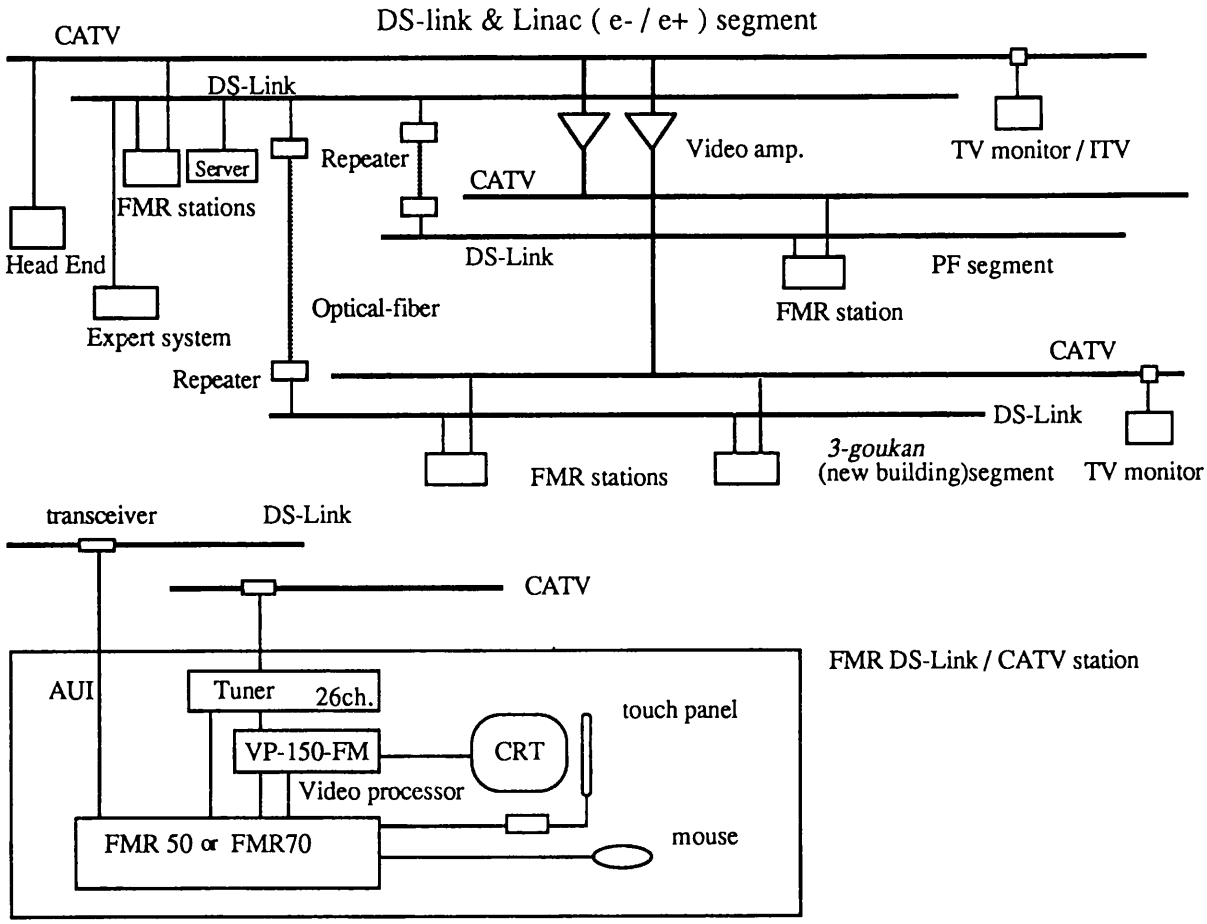

Fig. 8. CATV and DS-Link network.

Many application programs have been developed during the last two years. Presently, over 200 files are stored on the RAM disk of each node or server of the DS-Link. The gateway and server were replaced with much faster computers (FMR-70HX3, 25 MHz 80386) so as to obtain higher performance. The simple data-base for documents in Japanese was constructed and is in use. Programs for devices such as Vacuum, Magnet, Profile monitor, Trigger and Mode SW, as well as the menu system were upgraded; CATV control programs and document files were constructed.

A new operating system (OS/2) is now under installation and development on several network nodes. As DS-Link has been operated on MS-DOS with CPMGR (communication manager), it is easy to change the OS from MS-DOS to OS/2 with only a little change in the existing software. The new operating system will allow the following features on our DS-Link system: 1) multitask, 2) multi-language (BASIC interpreter, C, Fortran and Assembler), 3) high limit of the program/memory size and number and 4) desk-top publishing (DTP) software (which requires a large memory size) is also available on the network. However, there are still few commercially available applications of OS/2.

I. Abe

3C. Installation of CATV

The CATV system for the real-time display of accelerator status has been successfully and stably operated in the linac from 1988. In 1989, the number of channels was increased to 26 and the service area was also extended to over *3-goukan* (new building) and *PF kenkyutou* (PF building).

Channel selection can be made by a push button on the tuner or by command from a user computer through a serial port (RS-232C). Some channel has several pages (50-page max in each channel) of a still image picture (640×400 pixels) which is prepared by a handy still TV camera using a 2-inch magnetic disk. The pictures in the magnetic disk are selectable only through a DS-Link at each location. Computer graphics (DS-Link) may be overlapped with those CATV pictures. Their programs were developed on DS-Link. Users can select what they want to see on a 20-inch console CRT by the touchpanel or at any DS-Link station by using a mouse.

I. Abe

3d. Expert System (ES)

An expert system called KMTS (Klystron Modulator trouble shooting system), was developed by March 1989; thereafter, the system was connected to the linac computer network for receiving real data of the 2.5-GeV Linac. From October 1989, the KMTS started practical runs for the diagnosis of one of 48 klystron modulators, even though the receiving data are still not sufficient. Normally, the KMTS is just idling and waiting for shutdown data from klystron modulators; an inference engine starts automatically while picking up shutdown data from a klystron modulator through the network. However, the real data necessary for diagnosis was received only once in three months. Just after we developed the expert system, klystron modulators became very stable; consequently, there were few chances for diagnosis using the KMTS expert system.

Although the KMTS has now one hundred facts picked up through interviews in the field, a new K/B (knowledge base) is being added and tested for expected phenomena. The KMTS has a debugging mode for diagnosis, which is easy to simulate at any time.

The development for operation support and diagnosis using an Expert system has started on the basis of the KMTS. The beam-injection system (gun, modulator, vacuum, etc.) will be a new target in K/B. The new system has almost the same basic configuration as the KMTS (HP9000/370, HP-UX, C, Nexpert-Object (shell), Data-View). However, the user interface and knowledge base transparency will be modified in order to make it easier for users.

I. Abe

4. OPERATION GROUP

4a. New Safety Interlock System

A new safety interlock system based on personal key control was introduced in September 1989.

In the old system, the entering into and exiting from the linac tunnel were checked by magnetic personal card readers on both sides of electrically locked doors into the tunnel. If the card readers identified permission for any person, they opened the locked doors and sent messages to computers which added and extracted the read name to and from an inner list of tunnel users. When the list was empty, the signal of "TUNNEL CLEAR", which shows that there is nobody remaining in the tunnel, was sent to a main relay-logic circuit of the safety interlock system. Though the old system did not have any serious troubles, we needed to have a more reliable system in order to avoid any accident caused by a careless mistake or a computer trouble in response to an increasing number of users of the linac.

In the new system a personal key box and key switches take the place of the computer and the magnetic card readers, respectively. A person who wants to enter the linac tunnel takes out his key after getting permission by introducing his magnetic card into the reader in the front of a box, opens the door lock with the key switches using the key and keeps the key while staying in the tunnel. Only when all keys remain at the key box, is the signal "TUNNEL CLEAR" sent to the main relay-logic circuit of the safety interlock system through a programmable sequence controller. The history of each taking out and returning of the key is sent to a factory computer, displayed on a CRT and recorded by a printer.

In addition to the above-mentioned function, the new system introduces a lock control of both the key box and the key switches according to the accelerator status. Nobody can take out his personal key; even if he could, he cannot open the lock of the door when one of the rf power sources is under high-voltage operation or the accelerator is ready to operate. The programmable sequence controller watches and controls these conditions. The status of the input and output signals of the sequence controller is sent to the factory computer and displayed on the CRT.

T. Urano

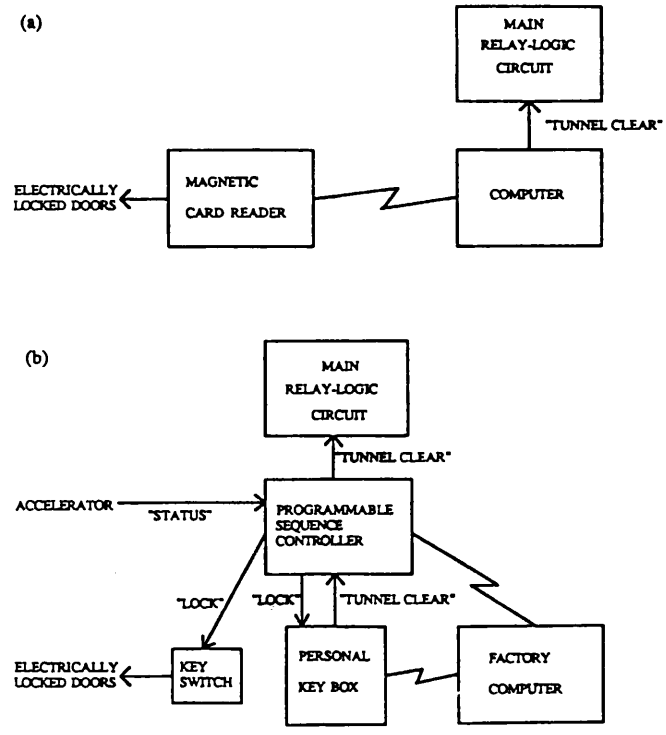

Fig. 9. Block diagram of the safety interlock system: (a) old and (b) new.

5. BEAM MONITORING SYSTEM

5a. Energy Analyzing System

Improvements in the monitoring system of the KEK 2.5-GeV linac have been undertaken in order to realize stable operation and fast beam recovery in the case of trouble.

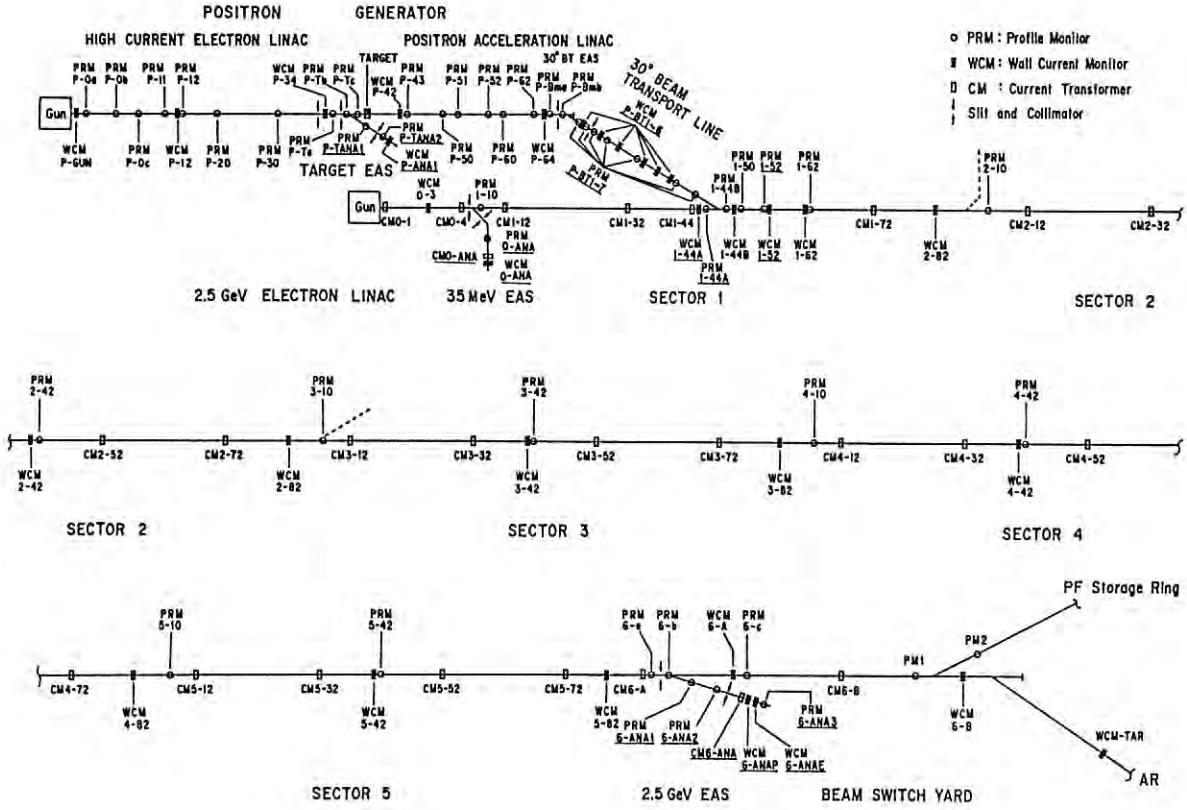

Fig. 10. Location of monitors in the 2.5-GeV linac: PRM (Profile Monitor), WCM (Wall Current Monitor), CM (Current Transformer) and EAS (Energy Analyzing Station).

Four energy-analyzing stations (EAS) have been built and installed on the accelerator at the following locations (see Fig. 10): (1) a target EAS which analyzes the beam at the end of a high-current electron linac just before a positron production target (~ 200 MeV); (2) a 30° BT EAS at the end of a positron acceleration linac (~250 MeV); (3) a 35-MeV EAS at the 35-MeV point of the 2.5-GeV linac immediately after the injection system; and (4) a 2.5-GeV EAS at the end of the 2.5-GeV linac. Each energy-analyzing station consists of an analyzing magnet, computer-controlled variable aperture slits and collimators, profile monitors and current monitors.

The energy spectrum of a short-pulse electron beam at the target EAS (Fig. 11; with a pulse width of ~ 1.5 ns and a peak current of 9 A) shows several peaks; each peak corresponds to a beam bunch and seems to have a different energy spread. The energy spectra of positron and electron beams at the 2.5-GeV EAS show an energy spread of ~ 0.5 % (FWHM/peak energy).

By introducing these stations, it has become easy to locate the cause of any troubles and was useful for the fine adjustment of the linac.

T. Shidara

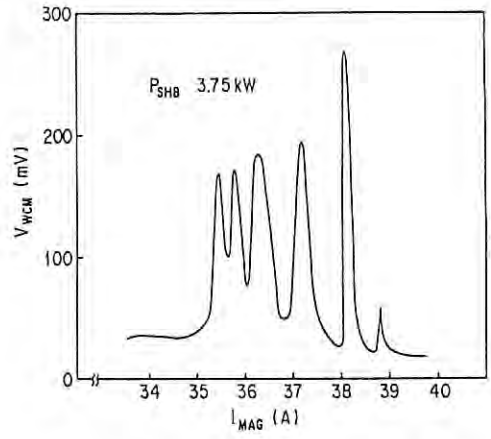

Fig. 11. Energy spectrum of a high-current electron beam measured by the energy analyzer at the positron-production target.

5b. Current Monitoring System

In order to observe short- and long-pulse beams, wall- and core-current monitors have been employed, respectively. However, their read-out systems were not well prepared. Operators of the linac have usually selected a signal from the current monitors, one-by-one, through signal selectors, observed the waveform with an oscilloscope and calculated the current value with a calibration table. In order to make this type of beam manipulation easier, simultaneous beam monitoring along the linac has been necessary. Thus, a new read-out system for the current monitors has been developed.

It is intended that the new system does not interfere with the previous monitoring system, involving an oscilloscope, which is required for observing waveforms. For short-pulse beams a signal from a wall-current monitor is divided into two identical signals by a power splitter, allowing it to be shared with one of the signal selectors connected to the operator's console. The output is then divided again by a 180° out-of-phase power splitter in order to obtain two signals of opposite polarity. One of the divided signals is used for the electron beam; the other is amplified by a fast 20-dB amplifier, and is used when the positron beam is accelerated, since the signal is ten-times smaller than that of the electron beam.

The total charge of the beam pulse has been digitized employing a charge-integration-type analogue-to-digital converters (ADC). Each signal is fed into a separate ADC input. In order to acquire the correct charge and to avoid noise from klystron modulators, precise gate timings are adjusted by computer-controllable delay generators.

For a long-pulse beam, the signal is processed with a buffer amplifier and a transient digitizer.

Electric modules, such as ADC's, are accommodated in one of the six CAMAC crates distributed along the 500-meter linac. These crates are connected to a data-acquisition computer (Micro VAX) through a fiber optic CAMAC serial highway in an enhanced byte serial mode of 5 M byte/s. The highway driver has the capability of the list mode DMA, which enables a direct memory transfer in which many CAMAC commands can be achieved. This capability is important for a process like that of this system which carries many different CAMAC commands sequentially.

One ADC or a transient digitizer in each crate is read out at a time, although each CAMAC crate deals with several monitors, since the delay timings are different. A delay timing parameter is set to each delay generator in six crates. After the beam comes, the program reads out and clears all of the data in the ADC's. It repeats this sequence at a rate of about ten times per second.

Then, the next program determines moving averages of the data over cycles in order to reduce any fluctuation of the beam, itself, and noise from klystron modulators; it then converts the units into milliamperes. The results are displayed on a graphic display at the operator's console room. Refreshing of the display once every two seconds is possible. They can be stored on a disk file upon a request from an operator for the later reference.

So far, operators have tended to manipulate the accelerator equipment while observing the current monitor just downstream. This process may cause problems in beam tuning of the linac. A beam-current distribution graph along the linac displayed at the operator's console room helps operators to adjust the beam correctly.

K. Furukawa

D. RESEARCHES

1. PLASMA WAKE-FIELD ACCELERATOR EXPERIMENT

Plasma accelerators are proposed as one of the probable next-generation high-gradient accelerators; among them the plasma wake-field accelerator (PWFA) is based on the simple principle that a plasma wake-field excited by drive bunches accelerates trailing bunches.

An experiment to test this principle has started utilizing an intense electron beam for positron production. The experimental apparatus, as shown in Fig. 12, was located at the positron generator beam-dump area: A plasma chamber (1 m long, 30 cm in diameter) was newly fabricated; it confines an Argon plasma with a maximum density of 10^{12} cm^{-3} during 5 ms during each beam burst time. A 60°-bending magnet was temporarily moved from the 500-MeV beam switchyard of the 2.5-GeV electron linac. A streak-camera system, which observes air-Cherenkov radiation from the beam, was employed not only for temporal separation of the bunch signal but also for intensity and dispersion analysis of the energy-analyzed image.

After the positron production target was taken out of the beam axis, a 250-MeV, 10-A, 2-ns electron beam was adjusted to be transported and focussed into the plasma chamber. This beam contains 6 micropulses bunched at intervals of 350 ps (=1/f, f=2856 MHz: acceleration frequency). These bunches cause a plasma wake-field, of which the wavelength depends on the plasma density; the intensity depends on the charge and the size of each bunch.

The first result was taken in July 1989. The energy of the beam passing through the plasma chamber was analyzed as a function of the

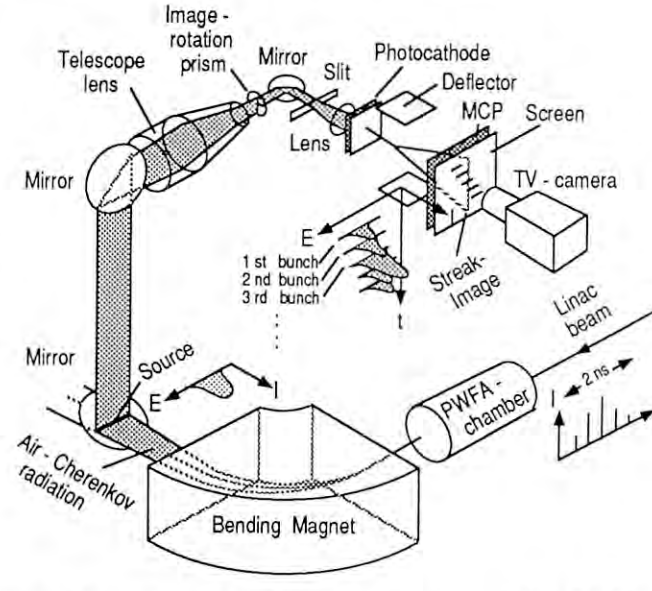

Fig. 12. Apparatus for the plasma wake-field accelerator (PWFA) experiment.

plasma density. Figure 13 shows the energy shift of the 5th bunch when the plasma density changes from 2 to 6 $\times 10^{11}$ cm^{-3}; the plotted points give the mean of the distributed energy in bunch, and the associated line is a calculation using a linear two-dimensional model. The result shows a resonance around a plasma density of 4 $\times 10^{11}$ cm^{-3}. This point corresponds to a plasma frequency of 2f (=5712 MHz); the 5th bunch decelerates by a few MeV.

A. Enomoto

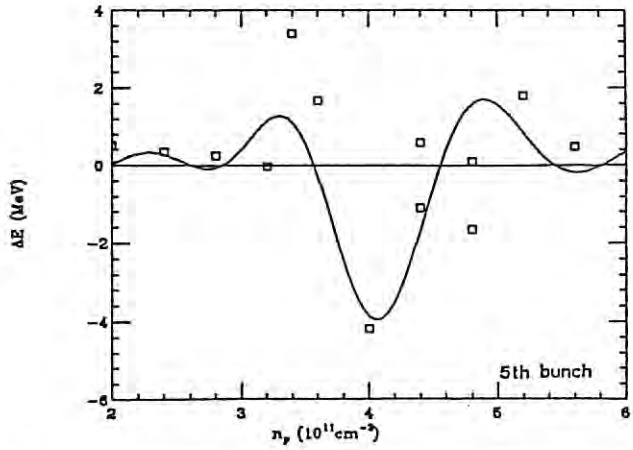

Fig. 13. Energy shift of the 5th bunch at a plasma density of around 4×10^{11} cm^{-3}. The solid curve shows expected energy shifts by a linear two-dimensional model.

2. CHANNELING RADIATION EXPERIMENT

Since Kumakov's publication in 1976, channeling radiation by high-energy electrons (positrons) has been noticed to be an attractive (Coherent, monochromatic, polarized and energy - variable) $\gamma(x)$-ray source. Experiments using 2.5-GeV positron beam, which is expected to give about 8-MeV γ, had been proposed by a group which included staff members of Tokyo, Nagoya and Osaka Universities; this program was supported by the linac division and approved by the PF PAC. During this period (until July 1989), a beam line for this purpose was newly constructed in the linac-end beam switchyard; also, a beam monitor for a low-intensity positron beam was preliminarily tested.

The channeling experiment requires the following conditions:

(1) A beam divergence of less than the critical angle, Ψ_c (= $(2U/E)^{1/2}$, where U is the channeling potential by crystal, E the positron energy); 0.13 mrad for Si at E=2.5 GeV.

(2) An acceptance angle θ of the detector, which determines the observed photon frequency, ω ($=\omega_m/(1+\gamma^2\theta)$, $\gamma=E/mc^2$); 0.1 mrad for $\omega/\omega_m=0.8$.

(3) Positron number restriction per pulse (2 ns) in order to reduce pileup events due to the longer recovery time (230 ns) of the NaI scintillator; ~10^3 positrons / pulse.

Figure 14 shows the new beam line deviated by two 18°-bending magnets. Between them, two lead collimators at an interval of 6.8 m restrict the beam divergence. A silicon crystal of 100 μm is installed in a goniometer chamber. After the crystal, incident positrons are dumped by a sweep magnet; only the channeling photon enters the NaI scintillator 15-m downstream of the crystal. The photon acceptance angle is limited by a lead entrance slit of 1 mm-φ aperture.

For beam transportation, two plastic scintillator beam monitors were prepared behind the collimators and in front of the crystal. As a positron counter, the photodiode detector of a 200-μm thick depletion layer was tested with a charge-sensitive preamplifier; it successfully gave a signal with a sufficient S/N ratio in the range of 10^3 positrons.

A. Enomoto

3. RF GUN

R&D of a thermionic microwave gun with a mesh grid was started at the end of 1988.

A microwave gun is expected to supply a brilliant electron beam because of its high accelerating field near the cathode surface. The high electric field makes it possible to extract a dense electron beam and to reduce emittance growth at a low-energy region. As a cathode of the microwave gun, a photo-cathode or a thermionic cathode can be selected. In the former case, since electron emission is caused by laser irradiation, a laser system is necessary and the bunch length control is performed by laser pulsation. In the latter case, the bunch length is controlled by an additional system, since electron beam emission occurs at almost one half the period of an rf cycle; heat control around the cathode is

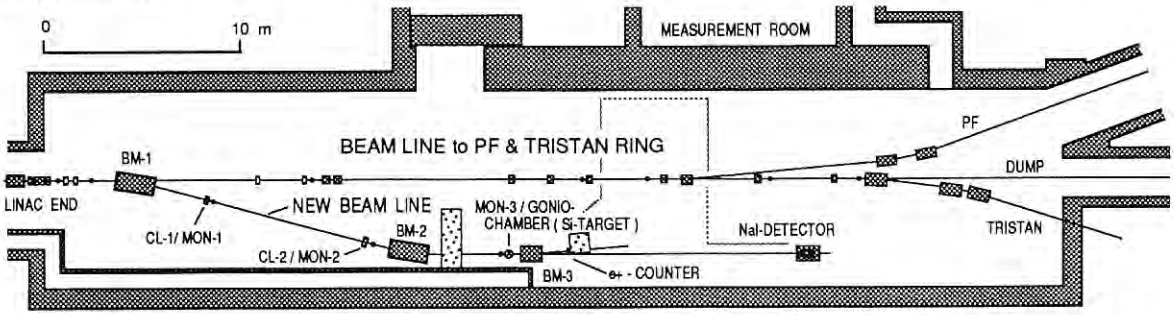

Fig. 14. A new beam line for the channeling radiation experiment. BM1,2: Bending magnets; CL1,2: Collimators.

rather complicated because the cathode is bombarded by reversely accelerated electrons at another half rf period.

A thermionic cathode was chosen in this work. In order to solve the back-bombardment problem we try to control the pulse width of emitted electrons by using a cathode with a mesh grid.

A pillbox-type cavity was designed and manufactured during the first stage of this work in order to investigate the basic features of the thermionic rf gun and to find problems in manufacturing the cavity. The cavity diameter is 79.5 mm and the resonant frequency is 2856 MHz, the same as that of our 2.5-GeV electron linac. The resonant frequency is finally tuned by a cylindrical plunger at a beam-extracting hole of the cavity. A grid mesh is made of a molybdenum foil 0.1 mm thick and attached to the end plate on the cathode side, which is demountable in order to test several structures of the mesh grid and cathode. The cavity and the tapered waveguide are made from oxygen-free copper block. At critical coupling, a loaded Q-value of 5,000 was achieved, though over-coupling will be required at a high-power beam test because of its very heavy beam loading.

The low power characteristics of the cavity were measured during several stages of manufacturing in order to find problems in lathing or soldering. Fortunately, we found that the soldering had no serious effect on the characteristics of the cavity.

We employ a lanthanum hexaboride (LaB_6) cathode with a diameter of 3 mm which can supply a 10 A/cm^2 current density at a temperature of 1,900°K. In order to maintain the temperature of the cavity constant, cooling water flows through both end plates.

T. Urano

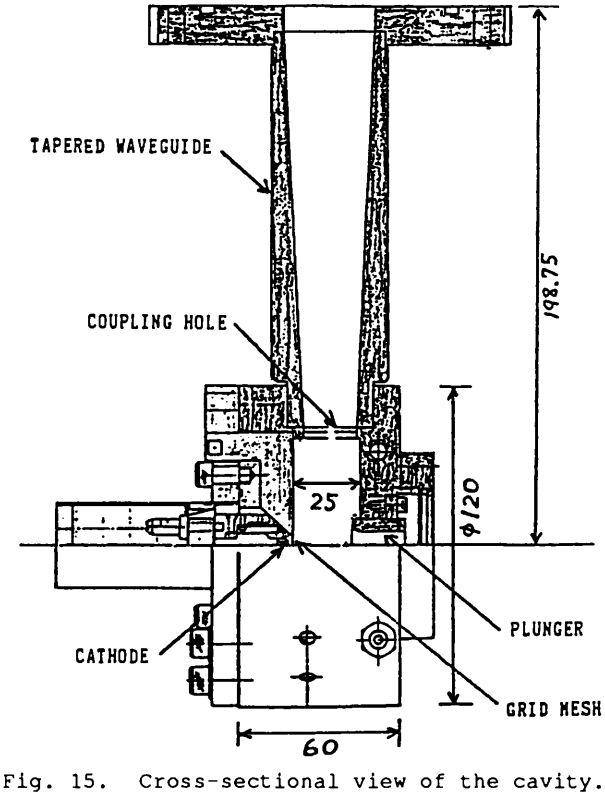

Fig. 15. Cross-sectional view of the cavity.

4. TEST LINAC

A new project to construct a test facility for the 2.5-GeV Linac was started in FY 1989 and is now in progress. Since the total operation time of the 2.5-GeV electron linac is more than 5000 hours per year, it is very difficult to test its components under such busy machine operation. It is desirable to use another facility to examine or estimate the performance of its components. Furthermore, to realize the researchers' desire to understand the physics of the accelerator, it is necessary to have their own. This is the primal motivation to advance this project.

The main purposes of this project are the research and development of acceleration technology. The leading aims of this facility are as follows:

1. High-luminosity beam acceleration experiments.
2. Improvement of the energy spectrum.
3. Experiments involving the free-electron laser.
4. Testing high-gradient acceleration.
5. Development of a newly designed beam-monitoring system.
6. Improvement of the production technique for a positron beam.
7. Experiments concern large peak-current acceleration.
8. Others.

The site of this test linac is situated beside the electron-gun room of the 2.5-GeV Linac. One part of that room is used for the test linac (with a separation provided by shielding blocks).

The intended performance of the Test Linac is as follows: The maximum acceleration energy is 60 MeV at 10 μA for the maximum average beam current. The length of this accelerator is about 14 m.

Experiments with this linac will be started in April, 1990.

T. Kurihara & H. Kobayashi

Light Source Division

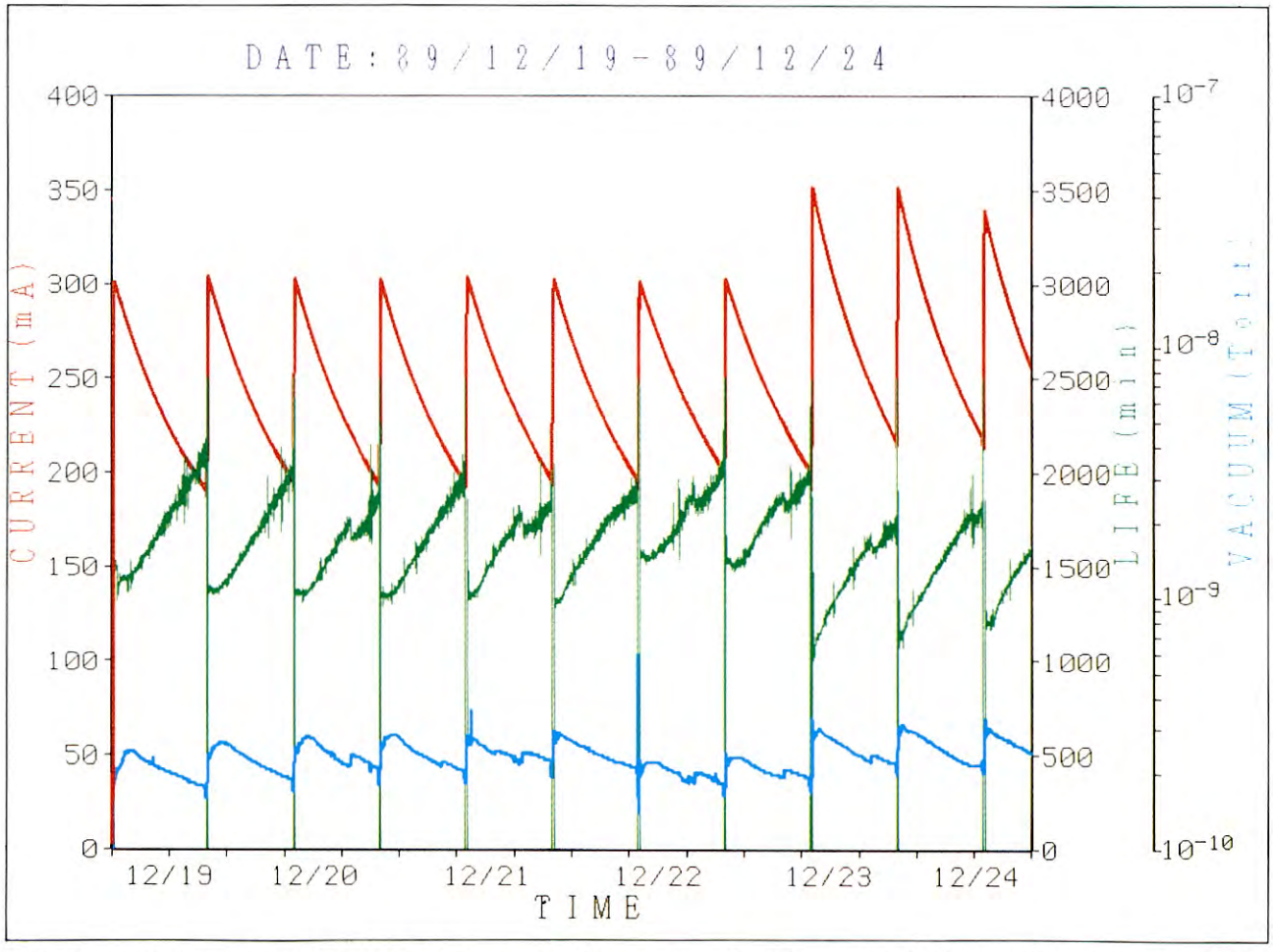

PF ring operation at the end of 1989. Red, green and blue curves show the current, lifetime, and vacuum, respectively.

LIGHT SOURCE DIVISION

A. INTRODUCTION

Construction of the Photon Factory started in 1978 and the storage ring (PF ring) was commissioned in 1982. Since then, several important changes have been made: (1) improving the vacuum system in 1985, (2) reducing the beam emittance, (3) renovating the rf-cavities for suppression of beam instabilities in 1987, and (4) initiating positron operation from 1988.

In the Photon Factory there are 23 spaces in which front-ends (beamlines) can be installed for introducing synchrotron radiation into the experimental hall. Twenty front-ends are available and have been commissioned for experiments, one is now under construction and two are still being discussed.

Six insertion devices have been installed into the PF ring and are now all in operation. An undulator for elliptically polarized light was installed in April, 1989 in beamline BL-28. During the summer shutdown (1989), a vertical wiggler (beamline BL-14) was replaced by a new one, saving 40 minutes of preparation time for every beam injection.

1. SUMMARY OF STORAGE RING OPERATION

From August to December 1988, the storage ring underwent a long shutdown. During this shutdown various modifications were carried out, mainly in preparation for insertion devices to be installed in straight sections B12-13 and B27-28. The chamber for the RF-KO which was located in section B27-28 was moved to the upper stream of the vertical wiggler between B13 and B14. The klystron system for the beam acceleration was reinforced, aiming at high beam-current storage.

The average stored currents and the injection intervals are still growing, as illustrated in Fig. 1. Since July 12, 1988, the storage ring has been operated with positrons. Though the injection rate of positron beams was very low (about 0.05 mA/sec in the beginning), it has now been increased to 0.4-0.5 mA/sec. The initial stored currents are 300-400 mA and the beam lifetime is 15 hours at 300 mA. A stored current of 500 mA was achieved with positrons in January, 1989.

Figure 2 is a plot of $I\tau$ (beam current × lifetime) obtained between October 4 and December 25, 1989. This plot well depicts the machine's general conditions; the recent value of 400 Amin is quite large. At present, beam injections take place every 12 hours. The present limit of the lifetime mainly comes from a narrow vertical aperture (19mm) of the MPW#16-duct. In a recent test with a low beta function at the long straight section where the MPW#16 is located, the beam lifetime increased by 20-30%. This will soon allow 24-hour operation.

Under electron operation we have long been annoyed with various destructive effects, such as a sudden beam loss (lifetime deterioration) due to both ion-trapping and micro-particle trapping. Such phenomena have never been observed with positron beams. As a result, the average lifetime was about 10% longer with positrons than with electrons, as long as the vacuum pressures and other operational conditions were similar. Though this is a remarkable benefit of positron beams, the vertical sizes of positron beams became large at high stored currents; this phenomenon was never observed for electron beams. The reason why such a curious behavior is observed only for positrons is still unknown. To suppress this beam blowup, we must add another octupole field, which results in a shortening of the beam lifetimes due to a reduction of the dynamic aperture. Table I shows the operation statistics for one-year positron runs.

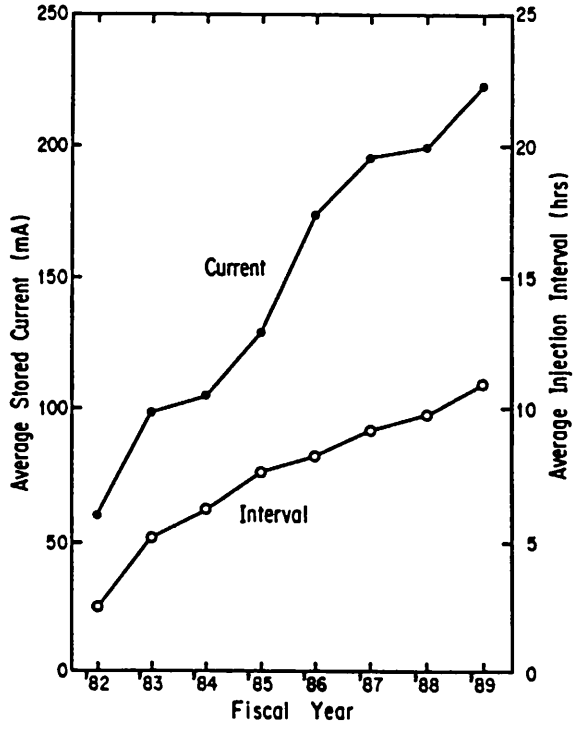

Fig. 1. Average stored currents and injection intervals.

Table 1. Statistics of operation with positron beams for user runs between July 12,1988 and December 25,1989.

Scheduled time (hr)	3677.6
Net user time: T (hr)	3169.0
Time spent for injection (hr)*	299.6
Integrated current in T (Ahr)	685.3
Average current in T (mA)	216.3
Number of injections	308
Interval between injections (hr)	10.3

* Including preparation time for insertion devices.

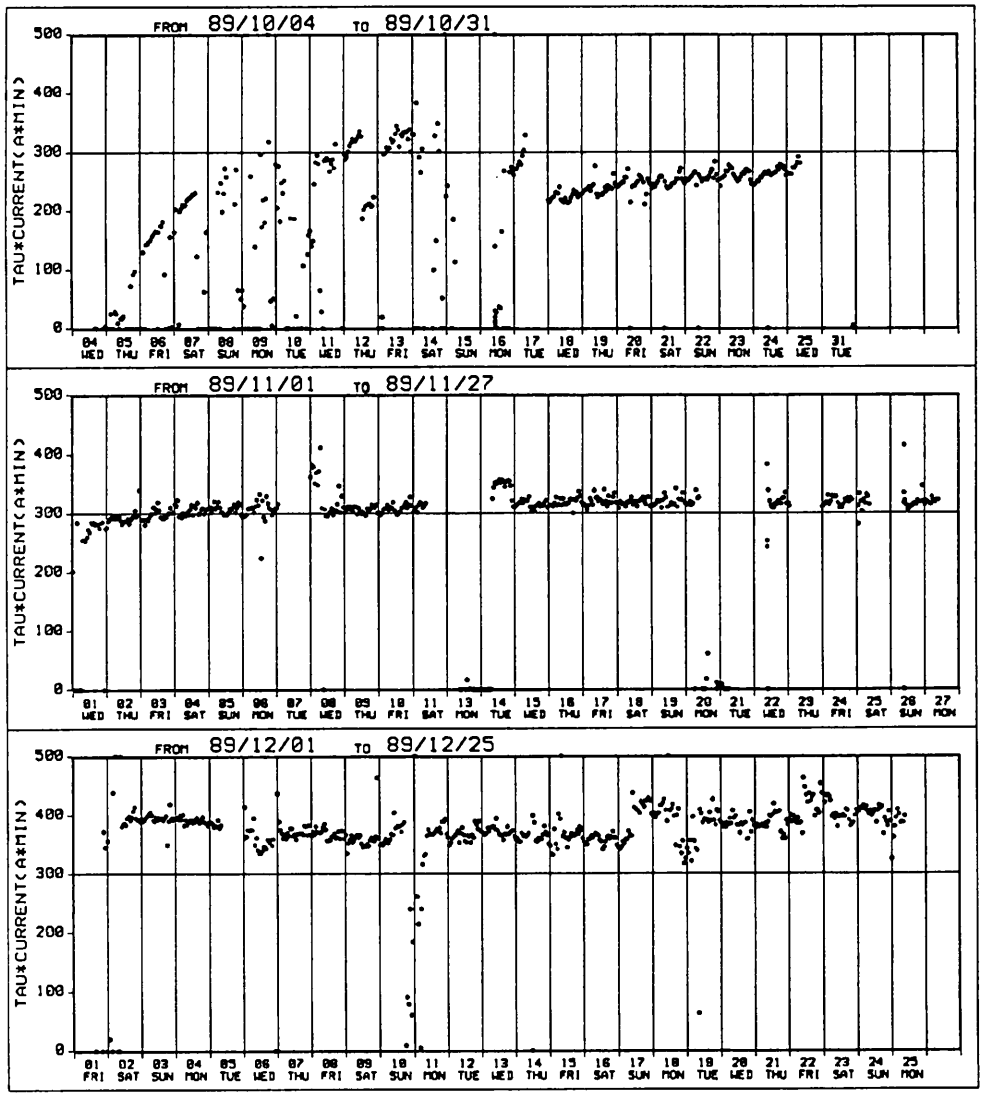

Fig. 2. Plot of Iτ (current × lifetime) from October 4 to December 25, 1989.

The superconducting vertical wiggler which had long been operated at beamline BL-14 was replaced in the 1989-summer shutdown by a new wiggler which is also the vertical bending-type with superconducting magnets. The old one had a narrow horizontal aperture (30 mm) in order to obtain high magnetic fields (maximum 6T). Because this aperture was too narrow for beam injection, a complicated procedure was required during every injection process: lifting the whole cryostat up and down and switching the magnet currents OFF and ON. Such a procedure is unnecessary for the new wiggler, since it has a sufficiently wide aperture (45 mm) to make beam injections (the horizontal rms-beamsize is 0.82mm after the reduction of the beam emittance in 1987). It has resulted in saving of about 40 minutes during every injection.

The movement of the photon beam axes originates from a large number of sources. A drift in the daily period is the largest one among them; its amplitude was enlarged by 3-10 times after reducing the horizontal beam emittance in 1987. Because the drifts were sometimes over 1 mm (measured 12 m from the source point), the experiments were considerably disturbed. A feedback system was employed in order to stabilize the drifting. It corrects any closed-orbit distortions of the entire ring circumference by making reference to the photon beam position at beamline BL-21. This correction works fairly well, though not perfectly; drifts of over 200 μm are still observed in several beamlines.

Such drifts are correlated to the weather and temperature of this area; this suggests that a distortion of the Light Source building due to temperature changes, especially of the building roof, propagates to its floor on which the storage ring is located. Thus, the magnets move by 100-200 μm over the course of a day. Figure 3 shows an example of a change in the average ring radius. The floor also moves vertically by the same amount. Because the circulating beams pass off-center of the quadrupole magnets, the orbits would be greatly disturbed, resulting in large photon-axes drifting at experimental stations.

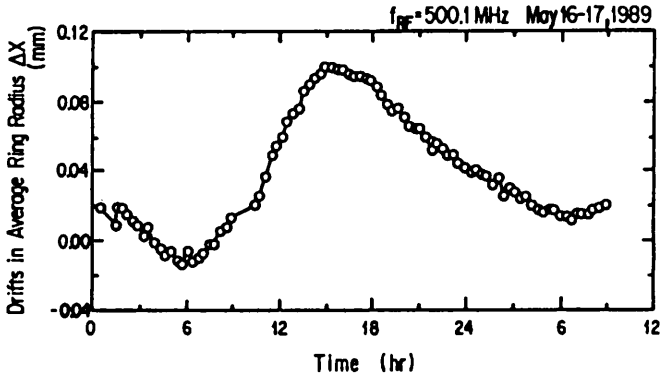

Fig. 3. Changes in the average ring radius over the course of a day.

Drifting in the ring floor level was measured with a water leveling system. Typically, a drift of 200 μm during one day was observed. A computer simulation made by Shimizu Construction Co. Ltd, which constructed this building, shows that the calculated distortions are of the same order of magnitude as those measured. However, the time dependence is not quite similar. The simplest way to eliminate this effect is to make thermal shieldings on the entire roof. Work to cover the roof with urethane-foam mats started on December 1989 and will finish within one month.

H. Kobayakawa

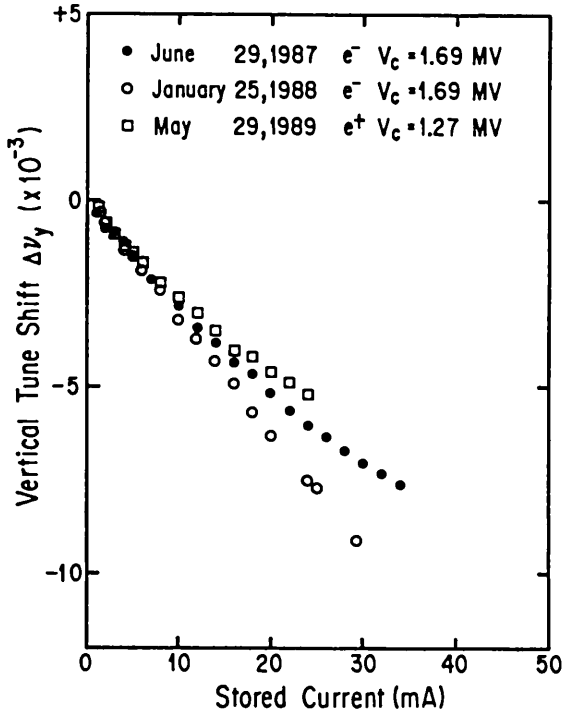

Fig. 4. Shift in the vertical betatron tune with the beam current (single bunch).

B. OPERATION

1. SINGLE-BUNCH OPERATION

1a. Single-Bunch Operation with Positron Beams

Single-bunch operation was undertaken with positron beams on March 13 and May 29, 1989. The charging rate was typically 0.08mA/sec with a repetition rate of 25Hz. The maximum stored current was 45mA. An abrupt deterioration of the beam lifetime, which had occurred frequently in single-bunch operation with electron beams, disappeared with the positron beams. This supports the hypothesis that lifetime deterioration is caused by a trapping of charged dust detached from the chamber wall by a strong electric field produced by the passing bunches.

Shifts in the coherent betatron tunes with the stored current (induced by a transverse broadband impedance of the ring) were observed. Figure 4 shows vertical tune shifts measured three times in the PF ring. For low beam currents, the tune shifted linearly with the current; this current dependence is a measure of the transverse impedance of the ring. The linear tune shifts are seen to be nearly the same in the three cases. This indicates that the transverse impedance has not greatly changed since June 1987, although several vacuum chambers with narrow gaps have been installed for insertion devices.

Bunch-length measurements were made using a new streak camera which detected the visible part of synchrotron radiation. Obtained data are still preliminary and further adjustment is needed to get fully reliable data.

S. Sakanaka

1b. Local Pressure Rise in Single-bunch Operation

Figure 5 shows pressure distributions in the ring under: (a) multi-bunch operation for user runs and (b) single-bunch operation. Abnormal pressure rises were observed at several locations, as shown in Fig. 5(b). There is an all-metal gate valve without an RF shield (GV-A) or a viton-sealed gate valve with a simple RF shield (GV-B) near each of the places. No pressure rise was observed near a gate valve which had a fine RF shield (GV-C). The local pressure rise is attributable to wakefields during single-bunch operation. Figure 6 shows changes in local pressures as a function of the stored current. The pressure near the GV-A rose as the stored current increased; the initial value was restored when the stored current decreased to zero. On the other hand, near the GV-B, the local pressure which had once increased did not recover very quickly. The product of pressure and beam lifetime ($P\cdot\tau$) is inversely proportional to the collision cross section of the beam with residual gases. Its change before and after single-bunch operation is shown in Fig. 7. The beam lifetime was also

degraded during user runs following single-bunch operation. The small values of the product indicate that a relatively large amount of gases with higher atomic numbers was released into the beam space. Some GV-B's were replaced with improved gate valves during the summer of 1989 in order to suppress any outgassing by wakefields.

Y. Hori

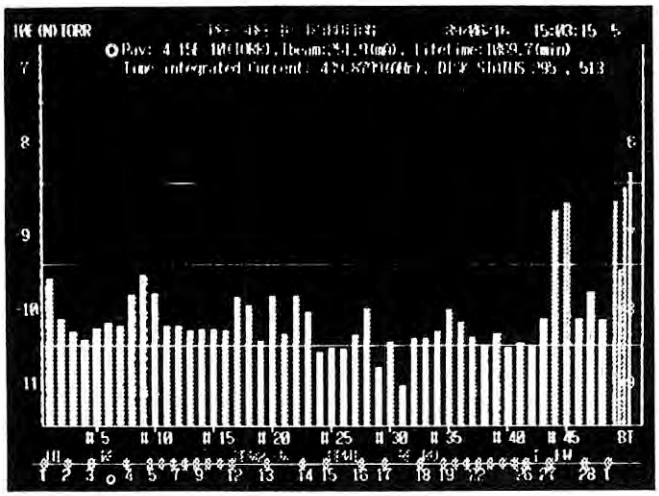

(a)

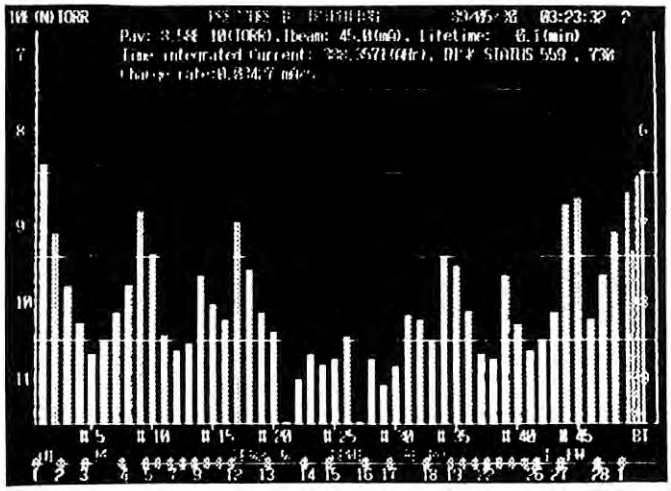

(b)

Fig. 5. Pressure distributions (a) at 250 mA of the stored current during a user run and (b) at 45 mA during single-bunch operation.

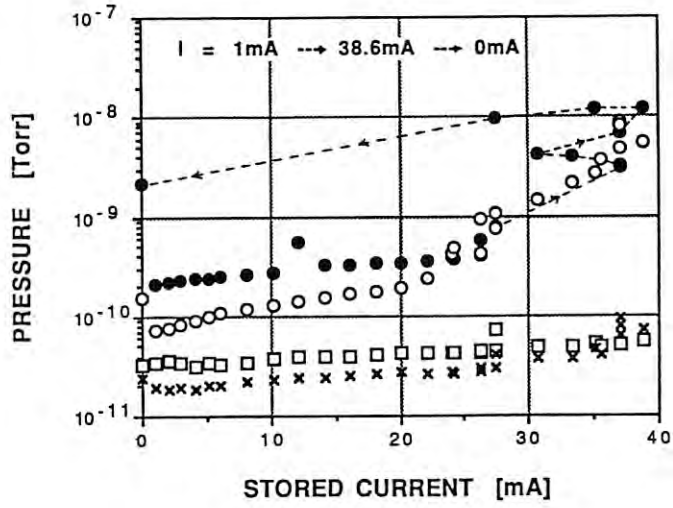

Fig. 6. Change in the local pressures near the GV-A (o), near the GV-B (•), near the GV-C (×), and at the reference point near which there was no gate valve (□) as a function of the stored current.

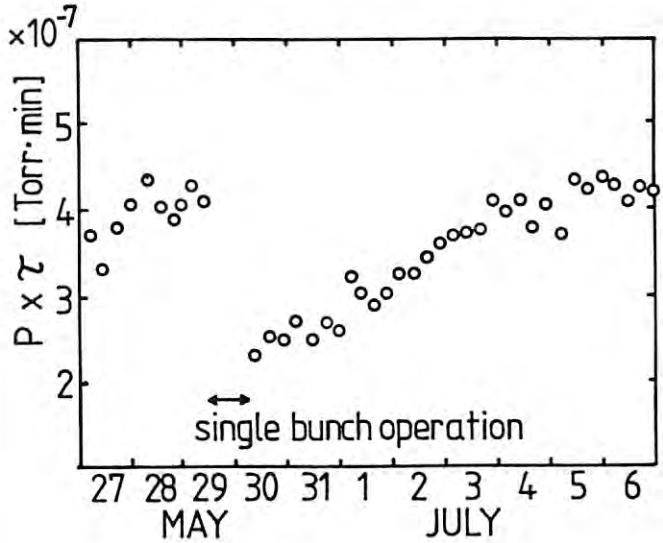

Fig. 7. Change in the product P·τ before and after single-bunch operation.

C. IMPROVEMENTS AND DEVELOPMENTS

1. INJECTION

1a. Recent Progress in the Accumulation Rate of the Positron Beam

The accumulation of positron beams started in July 1988. Since the PF ring was not originally designed for positron operation, there were problems in accumulating positrons into the ring; i.e. the available positron beam had small usable currents and large beam emittances than the electron beam. For the efficient accumulation of positrons, the following improvements were made: 1) development of a 40-nsec linac pulse (semi-long pulse), 2) improvement of the beam-transport efficiency, and 3) replacement of the injection system by a new one. During the last one year, the accumulation rate has increased from 0.05 mA/sec to a maximum rate of 0.58 mA/sec. The transition of the accumulation rate is shown in Fig. 8. The accumulation rate has been increased almost linearly as a function of time. During operation from May 14 to June 6, the timing between the positron beam and RF of the linac was desynchronized, resulting in an accumulation rate of less than 0.1 mA. On July 10, a 70-% probability was found for synchronization of the trigger signal between the linac and the ring. After refinement of this synchronization probability to 98 %, an accumulation rate of 0.4 ~0.5 mA was obtained. The accumulation time in user's time is presently less than 10 min.

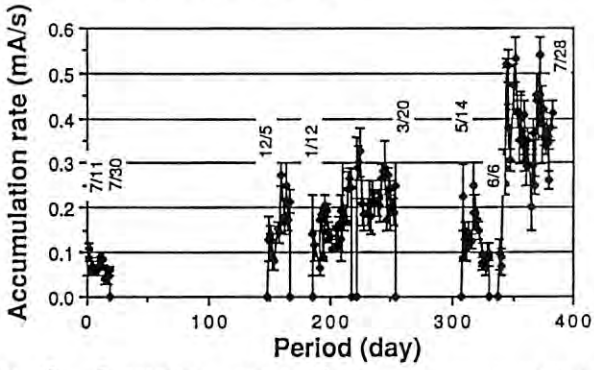

Fig. 8. Progress regarding the accumulation rate.

1b. Wall-Current Monitor for Measurements of Population Distribution Among Bunches.

A wall-current monitor was installed in the ring at a short section between bending magnets B22 and B23. The observed bunch structure in single-bunch operation shows that the bunch length was about 300 psec. Thus, the cutoff frequency of the total system, including that of a 60-m cable, is about 2 GHz. This wall-current monitor was mainly used for measurements of the population distribution among the bunches of the accumulated beam in the ring under ordinal operation. Figure 9 shows an example of the population distribution among the bunches.

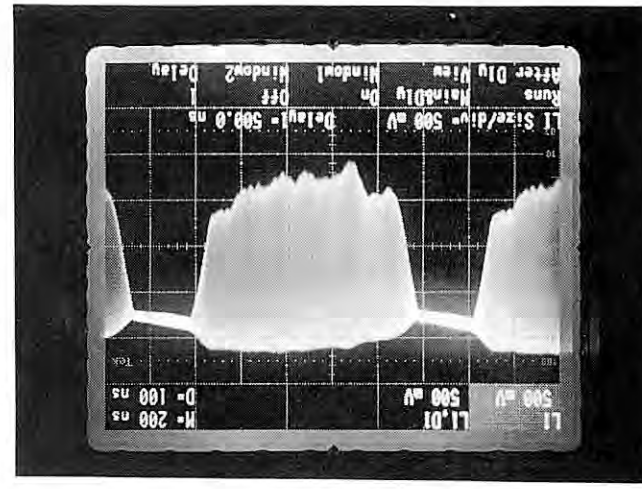

Fig. 9. An example of the population distribution among the bunches.

1c. Aperture Survey for Injected Positrons

Since the ring was built for an electron beam with a smaller emittance, and has many narrow vertical apertures, it is necessary to survey whether the ring aperture is wide enough for the large vertical envelope of the injected positrons. We calculated the emittance of the injected positrons at the injection point in a phase space. Figure 10 shows a result of a simulation of the first six turns of the injected beam; the horizontal and vertical emittances of the positron beam were assumed to be 1.0 mm mrad. The injection pulse bump was set at 20 mm and -1 mrad. The positron beam was injected at 34 mm and -2 mrad. The horizontal emittance of the envelope of the injected beam is expected to be 15.4 mm mrad. In horizontal phase space the emittance of the injected positrons is sufficiently small to pass through the narrow aperture at the injection point. Since other parts of the ring have wider apertures, the injected beam can stay safely in the horizontal. In vertical phase space the matching between the optics of the end of the BT and the injection point of the ring is insufficient; the vertical emittance of the envelope is thus expected to be 4.9 mm mrad. The vertical beam size with this emittance is 18 mm at the entrance of the narrow vacuum duct of an undulator which has a vertical aperture of 20mm. This duct seems to be too narrow for injected positrons. We then measured the current-decay pattern of the injected beam turning around the ring without RF acceleration by means of a ring wall-current monitor. Figure 11 shows the observed current decay of the injected positron beam. The injected beam current decreased from 1.66 mA to 1.0 mA during the first 5-6 turns. This phenomena was caused by kick errors in the pulse bump. The envelope of the current-decay curve after 6 turns is smooth for more than 100 turns, which proves that the ring has a sufficient vertical aperture.

T. Mitsuhashi

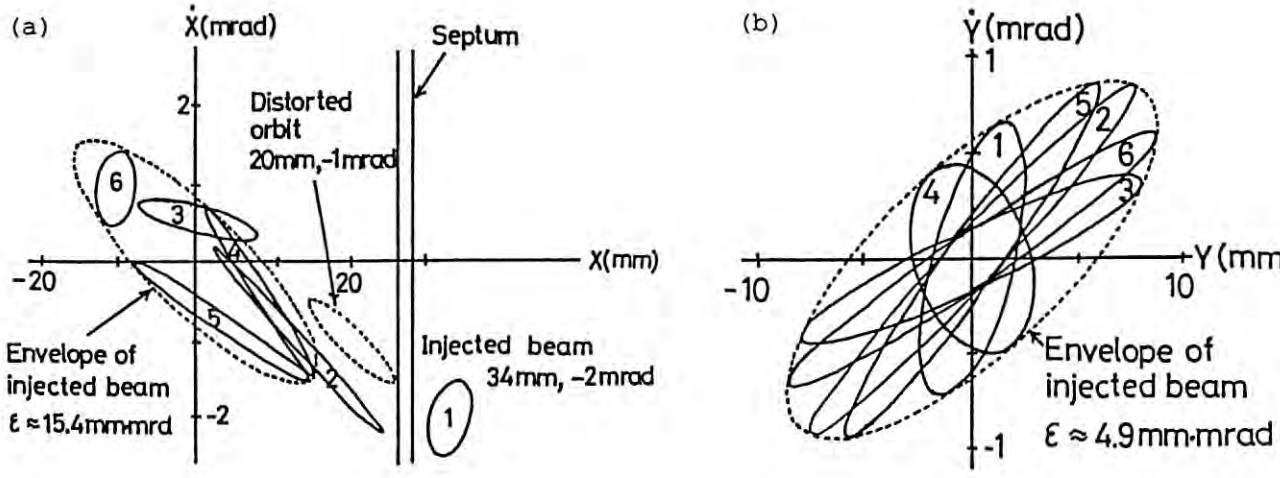

Fig. 10. Injected beam in phase space; (a) horizontal, (b) vertical.

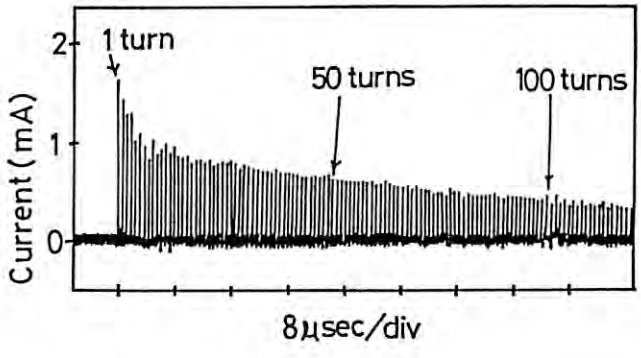

Fig. 11. Observed current decay of the injected positron beam.

2. RF

2a. Reinforcement of the RF-Power Source

Four single-cell cavities are used for beam acceleration in the PF ring. Until July 1988, two 180-kW klystrons (Toshiba E3774) were used for feeding the RF-power into the cavities. The maximum stored current of the ring was 370mA, limited by the available RF-power. In order to store more intense beams, the RF-power was increased by the addition of two klystrons during the shutdown from August to November, 1988. Hence, each cavity was individually driven by a single klystron. Related devices such as a high-voltage power supply for the klystron, a circulator, waveguides and low-level RF circuits were newly installed. A computer software for RF-control was also revised. Figure 12 shows a block diagram of the new RF system.

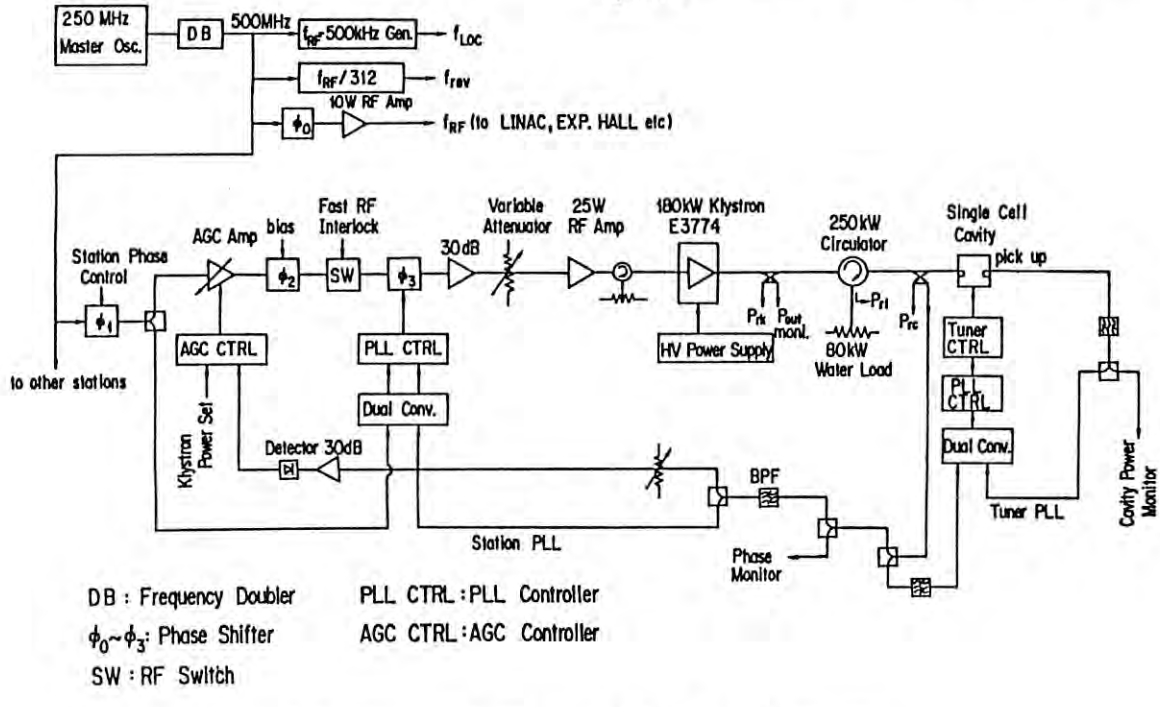

Fig. 12. Block diagram of the new RF system.

The klystrons have also been improved in cooperation with a manufacturer since the construction stage of the ring. With earlier klystrons, the ring operation was sometimes interrupted by klystron failures; breakdowns around the gun assembly, gradual deterioration of a gain or vacuum leakages. Successive improvements were made on a gun assembly, an output coaxial line, an output window and buncher cavities, resulting in the largely improved gain, efficiency and vacuums of the klystrons. The klystrons have recently suffered from fewer problems, only several times per year. An overall view of the recent model is shown in Fig. 13.

Reinforcing the RF-power source allowed us to achieve a stored current of 500mA at 2.5 GeV in January 23, 1989; this had been one of our goals since the design stage of the ring. The RF-power source is capable of attaining higher beam currents up to 800mA. With a stored current of 500mA, violent beam instabilities were observed in both longitudinal and vertical directions, together with heat-up problems in some parts of the vacuum chamber. Further work is needed to get rid of these problems.

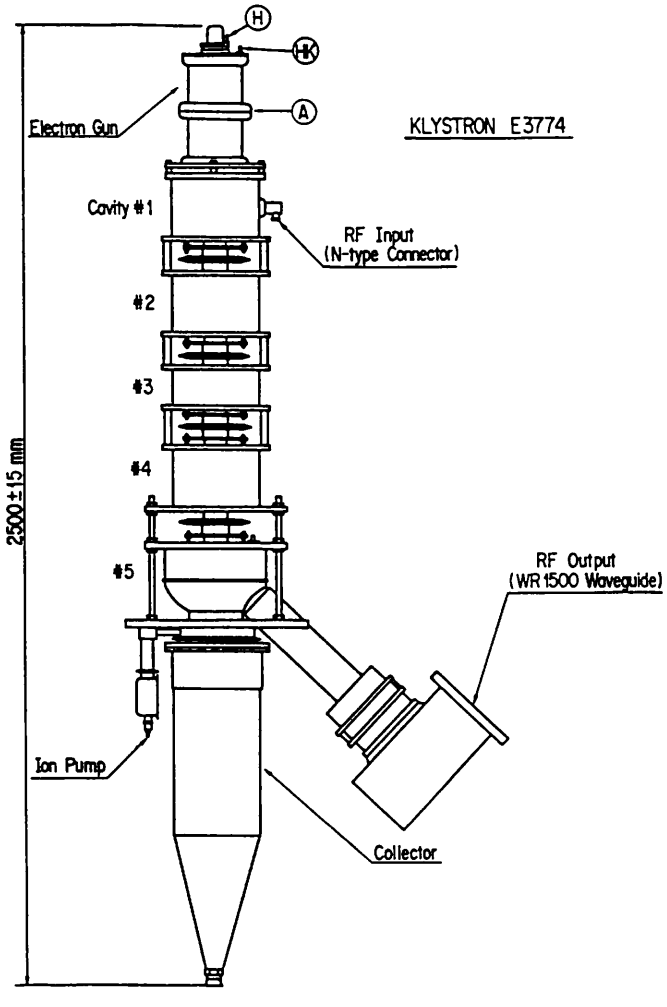

Fig. 13. Recent model of the 180-kW UHF klystron E3774.

2b. Beam Instabilities During Positron Operation

During positron operation, a vertical instability which was not observed during electron operation has appeared. The threshold current of this instability was about 17mA when the octupole magnets were not excited. Though strong octupole field producing a vertical tune spread of $\sim 2\times10^{-3}$ was used to cure the vertical instability, this instability was nevertheless not completely suppressed; the vertical beam size was enlarged at high currents. Figure 14(a) shows the measured vertical beam sizes versus the stored currents. When the vertical instability arose, the following frequency

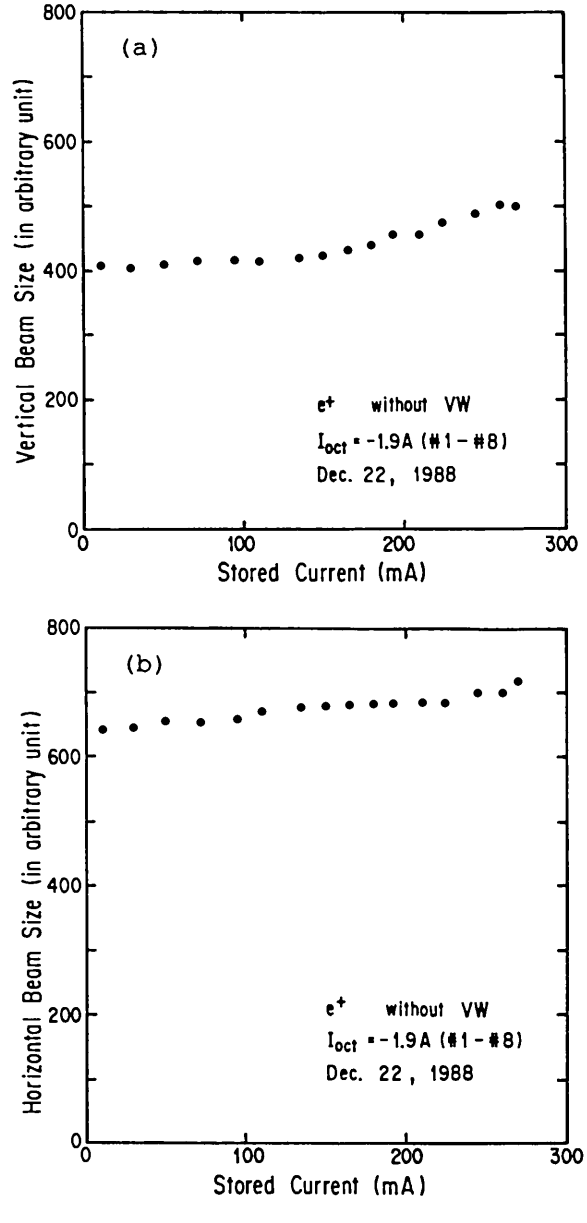

Fig. 14. Beam sizes during positron operation measured at BL-21 with a beam profile monitor. Excitation current of octupole magnets (OCT. #1-#8) was -1.9 A. The vertical wiggler was not excited. The ring was partially filled. (a) Vertical, (b) horizontal.

components appeared in a signal of a button-type position monitor:

$$f_{\mu,n}^{\pm} = n \cdot f_{RF} \pm (\mu \cdot f_r + f_{\beta y}), \qquad (1)$$

where n is an integer, f_{RF} the RF frequency, f_r the revolution frequency, $f_{\beta y}$ the fractional frequency of the vertical betatron oscillation ($=f_r \cdot \delta\nu_y$), μ the mode number with μ=285-300 (typical). This feature implies that the vertical instability is a kind of coupled-bunch instability. Since the instability threshold did not change when the temperatures of cavity cooling water were changed, this instability is likely to be caused by a resonance of some structure of the vacuum chamber.

One plausible reason why no vertical instability appeared in the electron operation is as follows. During electron operation, trapped-ions in the beam caused spreads in the betatron frequencies, thus suppressing the instability through Landau damping. In order to verify this assumption, we measured the spreads in the vertical tune distributions with both electron and positron beams. A coherent betatron oscillation was excited by the output signal of a network analyzer. The signal of the beam oscillation was detected with a quadrature photodiode and fed into the network analyzer to obtain the betatron frequency distributions. The measurement was made by changing the excitation current of the octupole magnets. Figure 15 shows the spreads in vertical betatron tunes, thus obtained. The dependences of the tune spreads on the octupole currents were quite different for the electron and positron beams. The strange behavior with the electron beam was probably caused by trapped-ions, though no detailed mechanism is yet known. Furthermore, the tune spreads with the positron and electron beams were nearly of the same amount when the octupole magnets were not excited. Thus, the reason why no vertical instability arose during electron operation (even with the octupoles off) is still unknown.

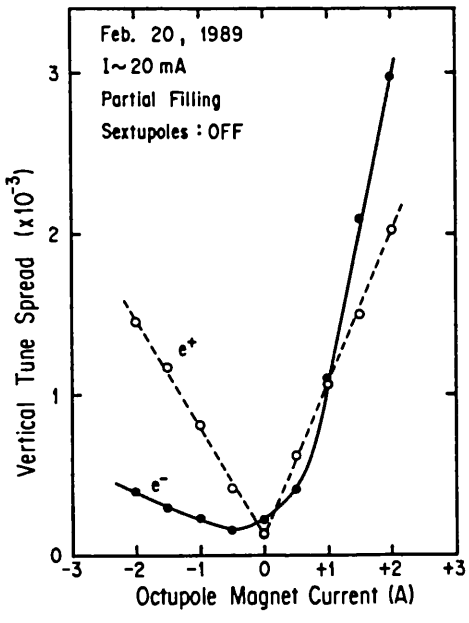

Fig. 15. Dependences of vertical tune spreads on the excitation current of octupole magnets. Eight octupoles (OCT. #1-#8) were used. Open and closed circles represent the tune spreads with the positron and electron beams, respectively. The ring was partially filled and the stored current was about 20mA. All sextupole magnets were off.

No difference in the longitudinal instabilities was observed under positron and electron operation. As mentioned in ACTIVITY REPORT #6, six dangerous coupled-bunch instabilities induced by the cavities had been largely suppressed by careful adjustments of higher-order-mode frequencies. However, several longitudinal coupled-bunch instabilities still exist. The threshold current for the strongest one is about 80mA. When it arose, the following frequency components appeared in the signal of the button-type position monitor:

$$f_{\mu,n}^{\pm} = n \cdot f_{RF} \pm (\mu \cdot f_r + f_s), \qquad (2)$$

where f_s is the synchrotron oscillation frequency and μ=94. At a stored current of 100mA, other longitudinal instabilities with mode numbers of μ=26, 158 and 151 appeared. We have not yet identified whether these instabilities were induced by higher-order-mode resonances of the cavities or by resonances of some structures of the vacuum chamber. The horizontal beam size was enlarged at high currents due to longitudinal instabilities, as shown in Fig. 14(b). A partial filling of RF buckets with about a 25% gap was found to ease the longitudinal instabilities to some extent. The ring is routinely operated with this filling.

S. Sakanaka

3. VACUUM

3a. Improvements of the Vacuum System

The main improvements during FY 1988 were as follows:

1) Several beam ducts were replaced for improvements of the magnet system, installation of an insertion device and a newly approved beam line. Several gate valves and rough pumping systems were also rearranged or installed in the ring.

2) Non-evaporable getter (NEG) pumps were installed in place of distributed ion pumps (DIP) in vacuum ducts at bending magnets B20 and B27.

The present vacuum system components are schematically shown in Fig. D-5.

3) A shape transition piece connecting ducts with different cross sections is necessary to minimize beam-wall interactions which are large at the stepwise undulation of the inner surface. Some flanges have pocket spaces, because the cross section of commercially available flanges is round and that of the vacuum ducts is nearly elliptic. These flanges and some steep

transitions were heated up, depending on the filling pattern of bunches. The heat-up is attributable to wakefields. To suppress the beam-wall interactions, the transitions were replaced with smoother ones and the pocket spaces were filled with specifically designed copper gaskets. This improvement was effective in suppressing the heat-up, even under single-bunch operation.

3b. Performance of the NEG Pump

In the summer of 1988 two DIP's in ducts B20 and B27 were replaced by NEG's in order to test their pumping performance under actual ring operation. The NEG module is St707 WP38/950 supplied by SAES GETTERS S.P.A. Each NEG set comprises four modules. Duct B20 had been fully outgassed by "self-cleaning" and duct B27 was newly constructed when the NEG was installed. Ducts B06 and B13, in which the DIP's were installed, were chosen as observation points. Duct B06 had been fully outgassed, and an SR absorber in duct B13 was replaced with new one. Thus, the outgassing rate in ducts B27 and B13 was higher than that in ducts B20 and B06. We monitored the total and partial pressures in the B ducts using B-A gauges and quadrupole mass spectrometers (QMS's) just downstream of the B duct.

The ring vacuum is evaluated by "normalized pressure", namely, the pressure divided by the stored beam current, since the outgassing is approximately proportional to the beam current. Also, the operation time of the ring is evaluated by the time-integrated beam current (called "integrated current" hereafter).

After the 1988 summer shutdown the ring was operated from December 1988 to March 1989. The normalized pressure in each B duct decreased almost linearly with the integrated current in logarithmic scales. The pressures in ducts B27 and B13 were about ten times as high as those in ducts B20 and B06. This difference was caused by the different outgassing rates. However, no obvious difference was observed between the DIP and the NEG. Two NEG modules in duct B27 were reactivated when the normalized pressure reached about 1×10^{-11} Torr/mA, and two NEG modules in the duct B20 when it reached about 7×10^{-12} Torr/mA. The normalized pressures in both B ducts decreased stepwise after reactivation. Also, when the normalized pressures in both B ducts reached almost 1×10^{-12} Torr/mA, the four NEG modules in each B duct were reactivated. However, no obvious pressure decrease was observed after reactivation. Dry nitrogen was introduced into duct B27 in May 1989, and a new insertion device was installed at the downstream of duct B27. The outgassing rate thus again became high in duct B27. Then, only the NEG in duct B27 was fully activated during baking.

Figure 16 shows the normalized pressures in ducts B06, B13, B20 and B27 between May and July 1989. The stored beam current was 150 - 350 mA during user runs. The arrows indicate the flashing of TSP's (titanium sublimation pumps). The normalized pressures depend strongly upon

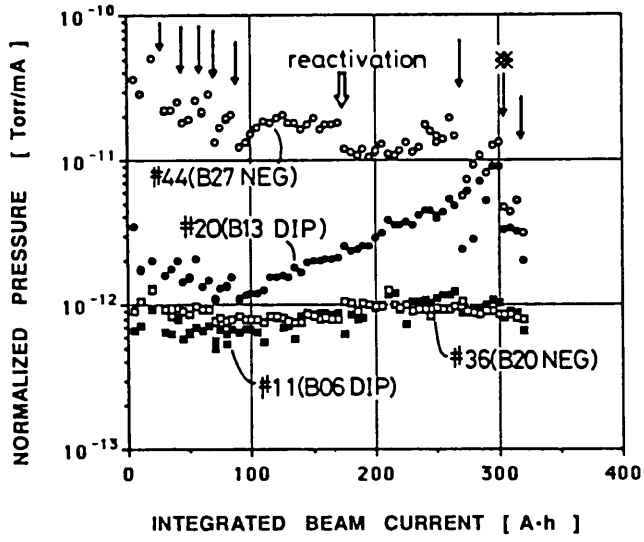

Fig. 16. Normalized pressures in ducts B06, B13, B20 and B27 as a function of the time-integrated stored beam current from May to July 1989. Arrows indicate flashings of titanium sublimation pumps. Changes in the partial pressures at the time denoted by an arrow with a ※ are given in Fig. 17.

the flashing of the TSP's, especially in ducts B13 and B27. No TSP was flashed from 90 to 275 A·h of the integrated current. During this period, the normalized pressure in duct B13 increased by about seven times. The normalized pressure in duct B27 increased only by about twice, and then maintained its value, though there was more outgassing from the newly installed downstream insertion device. We found that the NEG could sufficiently pump such large amounts of gas. Also, the pressure in duct B27 decreased by one half after reactivating the NEG, and then increased again. A gradual pressure increase was observed in duct B06. Such an increase was not observed in duct B20, though the pressure slightly increased after the reactivation. The difference was that the NEG in duct B27 worked in the 10^{-9} Torr range and the NEG in duct B20 worked in the 10^{-10} Torr range. Even considering the amount of absorbed hydrogen in the NEG, the hydrogen equilibrium pressure should be far below 1×10^{-10} Torr at room temperature. The NEG would have a high pumping speed in the 10^{-9} Torr range and a relatively low pumping speed in lower pressure ranges. The normalized pressure did not go down far below 1×10^{-12} Torr/mA, despite the reactivation of the NEG or the flashing of the TSP. This ultimate value corresponds to a photodesorption yield below 1×10^{-6} molecules/photon.

Detected residual gases were H_2, CO, CH_4, Ar, H_2O and CO_2. The partial pressures of the first four gases depended not only upon the effectiveness of the pumps but upon the stored beam current. The introduction of argon conceivably arises from discharge cleaning,

which was previously done. Figure 17 shows the changes in the QMS signal intensities of the four gases (H_2, CH_4, CO and Ar) over 24 hours. Each QMS was not calibrated. The flashing of the TSP was effective for H_2 pumping, and especially for CO pumping in ducts B13 and B27, though not so effective for pumping all of the gases in ducts B06 and B20. Residual gas analyses showed that the reactivation of the NEG was not so effective for pumping CO.

We tried to calculate the NEG pumping speed by examining the responses of the total and partial pressures when the adjacent pumps were switched on and off. The estimated pumping speed of the NEG for H_2 was 10% of the nominal value or less, and that for CH_4 was almost zero.

We obtained the following conclusions and suggestions. The NEG worked well in the range 10^{-11} to 10^{-9} Torr as did the DIP. Additional pumping is necessary to pump methane. The pumping speed of the NEG for hydrogen seems to be less than the nominal value, and an equilibrium pressure seems to be in the 10^{-10} Torr range, even at room temperature.

Y. Hori

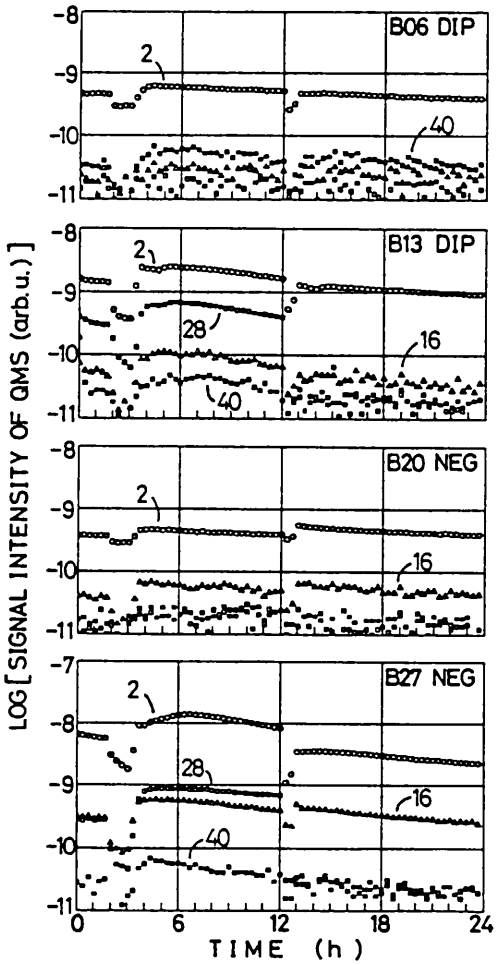

Fig. 17. Changes in QMS signal intensities of H_2, CH_4, CO and Ar over one day in ducts B06, B13, B20 and B27. The positron beam was injected to 350 mA at 3:00 and 12:30, and the titanium sublimation pumps were flashed during the second injection.

4. MAGNET

4a. General

During FY1988 and FY1989 the following improvements were carried out in the magnet system. Four quadrupole magnets (QM's), which were not used in the present low emittance optics, were removed from the ring in order to produce free space. Octupole magnets (OCT's) were reinforced and some of them were moved to locations where better performance was expected. Dodecapole magnets were installed for testing. Two electronic loads were installed to correct the tune shift produced by a new multipole wiggler (EMPW#28). Power supplies (PS's) of the QM's were so improved that polarity changes could be carried out with manual switches instead of changing the connections of electric cables at the PS's.

4b. Improvements of Octupole Magnets

In positron operation, the vertical beam size increased with beam current. This is attributable to a vertical coupled-bunch instability. The beam-size growth could be suppressed with the OCT's at low currents. However, even with the maximum field strengths of the OCT's, the beam-size growth was still observed at beam currents above 300 mA. For high-current operation, the OCT's were reinforced by mounting iron blocks on the original magnetic poles, and the vacuum chambers at the OCT's were also replaced with those of smaller diameters. This resulted in an increase of field gradients ($B^{(3)}1$) by factors of 1.5 to 3. The measured excitation curves are shown in Fig. 18. Furthermore, water-cooling pipes were mounted on the OCT's. Two OCT's were moved to places where the betatron functions were large, so as to increase the tune spread produced by the OCT's. After all these improvements, the OCT's are now able to produce a vertical tune spread of about 2×10^{-3}, which is larger than the earlier value by a factor of 3.

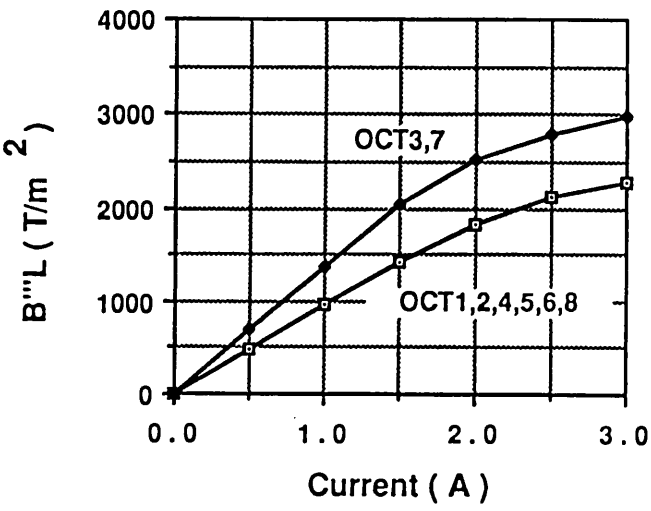

Fig. 18. Measured excitation curves of octupoles.

4c. Dynamic Aperture with Strongly Excited Octupole Magnets

Under positron operation, the OCT's had to be strongly excited to suppress the vertical instability. However, the beam lifetime was reduced with an excitation of the OCT's (Fig. 19(a)). A calculation showed that the dynamic aperture shrank upon exciting the OCT's, and could be smaller than the physical aperture (Fig. 19(b)). To improve the dynamical problem associated with the OCT's, six dodecapole magnets were installed in the ring and under testing.

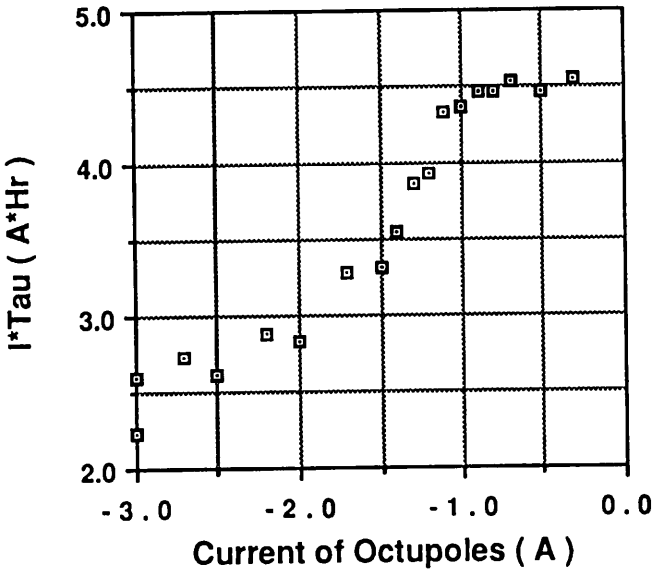

(a)

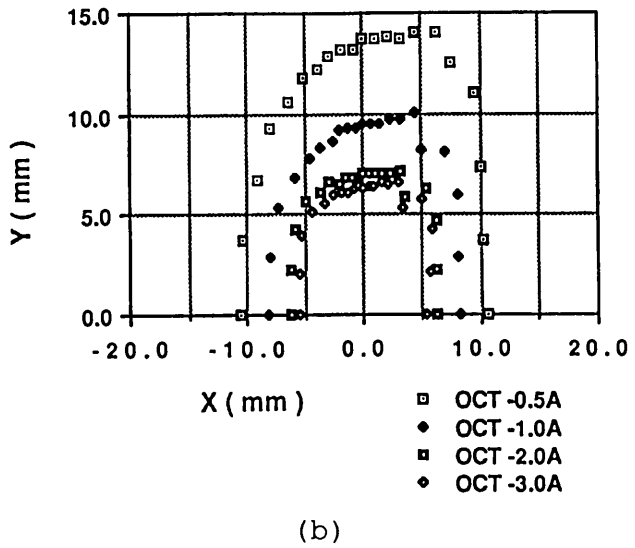

(b)

Fig. 19. (a) Dependence of lifetime on octupole current. (b) Calculated dynamic aperture at a long straight section with octupoles excited.

4d. Low-β Optics

The beam lifetime is considered to be mainly determined by Coulomb scattering. Unless the OCT's are excited so strongly, scattered positrons (or electrons) are likely to be lost at MPW#16 where the vacuum chamber is effectively narrowest in the ring, taking into account the betatron functions. To increase the beam lifetime, a modified version of the low-emittance optics was calculated. In this optics, the vertical betatron function at MPW#16 was decreased by a factor of about 2 (Fig. 20). The new optics has been under testing in machine studies. The measured values of the betatron functions agreed well with the calculated values, (Fig. 20).

M. Katoh

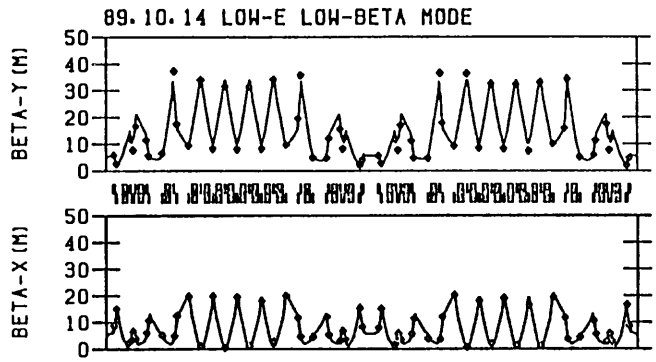

Fig. 20. Measured betatron functions.

5. INSERTION DEVICES

5a. 5-pole Superconducting Vertical Wiggler

1) Construction

A superconducting vertical wiggler was installed into the PF ring in Aug. 1989. The wiggler has 5 magnetic poles and is operated in the permanent-current mode with a field strength of 5 Tesla. The characteristics and a schematic drawing of the wiggler are shown in Table 2 and Fig. 21, respectively.

The wiggler cryostat includes two layers of thermal shields located between the vacuum chamber and helium vessel, as shown in Fig. 21. The estimated heat loads into each shield and the helium vessel are shown in Table 3. Each shield is cooled down by refrigerators with capacities of 130 W at 80 K and 12 W at 20 K. Since the current leads are mainly responsible for the heat load, they are pulled up from the helium vessel in the permanent-current mode. As a result, the total heat load into the helium vessel was calculated to be 2.63W and was measured to be 1.4 W (2 L/h). The helium consumption was reduced to 0.04-0.25 L/h with a helium re-liquefier with a capacity of 3 W at

Table 2. Characteristics of the new vertical wiggler.

Maximum field strength on the beam orbit	5 Tesla
Magnet gap	66 mm
Magnet pole size (widthxhight)	40 mm × 260 mm
Number of magnetic poles	5 poles arranged every 200 mm
Rated exciting current	220 A at 5 Tesla
Superconducting wire	NbTi : Cu 1 : 1 size 1.70 × 0.85 mm^2
Cross section of coils	65 mm × 70 mm
Number of turns	2520
Liquid helium consumption in the permanent current mode	0.1 L/h
Damping rate of the permanent current	1.4×10^{-5}/h
Inductance	1.31 H/coil

Table 3. Heat load.

	80 K	20 K	4.2 K
Radiation	11.37	0.62	0.001
Conductivity through the support rod	16.4	2.19	0.30
Current lead		2.09	2.20 (0.16)*
Helium inlet and instrument		2.56	0.13
Total heat inflow	27.77	7.46	2.63 (0.59)

* (): current leads are disconnected

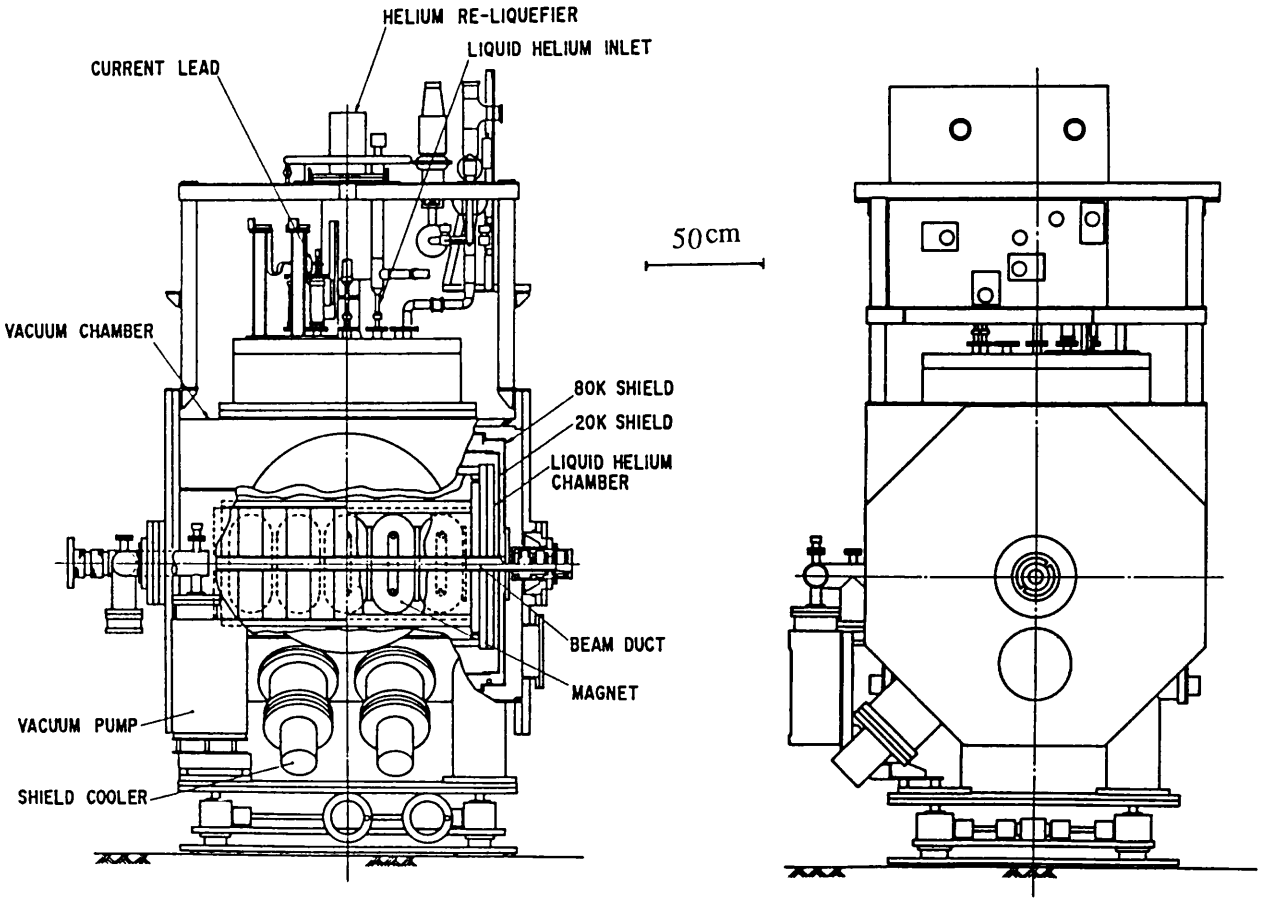

Fig. 21. Side and front views of the superconducting wiggler.

4.2 K. While the exciting current is being supplied, the current leads are connected to the superconducting coils in the helium vessel and superconducting switches warmed up by 4 heaters of 2 W each, resulting in an increased helium consumption of about 10L/h.

After some training, a field strength of 5.01 Tesla was achieved at the center of the wiggler magnet with an exciting current of 223.6A. The magnetic field along the center line of the wiggler magnet was measured by using a calibrated hole probe. The measured field distribution is shown in Fig. 22, in comparison with that calculated with program code JMAG.

K. Ohmi

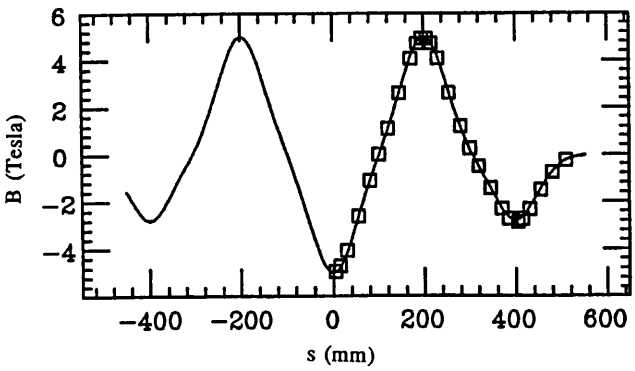

Fig. 22. Magnetic field distribution along the center line of the wiggler. Solid line and squares show the results of the measurement and calculation, respectively.

2) Operation

The wiggler was operated with 3 magnet poles because of the experimental requirements. The inner 3 poles were used for the operation, since the orbital distortion in the wiggler section became small. The center coil can produce a field of 5 Tesla with both side coils canceling the field integral along the center line of the magnet.

The wiggler was excited by two power supplies with current capacities of 150 and 300 A. The operating currents of the center and side coils were determined by the condition that the stored positrons were not damped. Moreover, such operation did not disturb beam injection. When the PF ring was operated with the wiggler off, the beam injection was disturbed by a remanent field with a strength of 2.2×10^{-3} Tesla·m. The remanent field was canceled by two normal steering magnets.

Beam wiggles on the vertical y-plane. The effect of edge focusing gives a finite horizontal tune shift $\Delta\nu_x$, while it cancels out for vertical tune shift $\Delta\nu_y$. $\Delta\nu_y$ could be caused by the gradient of the nonlinear field d^2B_x/dy^2 on the vertically wiggled orbit; however, the nonlinearity was estimated to be very small with a resultant negligible tune shift. The measured tune shifts are shown in Fig. 23. $\Delta\nu_x$, originating from edge focusing, was larger than $\Delta\nu_y$ arising from nonlinearity. The tune shift was corrected by changing the currents of nearby quadrupole magnets located in the same straight section with the wiggler. Another nonlinearity of d^2B_x/dx^2 does not cause tune shifts, but affects the dynamic aperture of the ring. The nonlinearity was expected to be mostly canceled as a result of integration along the beam orbit. The residual nonlinearity was difficult to estimate by field calculations, but was found to be negligible by measuring the vertical closed orbit distortion upon changing the horizontal orbit.

In the permanent-current mode the current gradually decreased due to the resistance of junctions between the coils. The mean lifetime of coil currents was 7.3×10^4 hours. An orbit distortion due to the current decrease was automatically corrected with a computer by using the normal steering magnets. The wiggler was operated continuously without any problem for a few weeks and without supplying a current.

A wiggler duct made of aluminum has an aperture of 45mm in width and 31 mm in height and is cooled by water. Upon increasing the wiggler field its radiation comes to hit the duct with energies of several kilo-Watts at stored currents above 300 mA. One part of the scattered photons which pass through the duct wall reached the helium vessel, resulting in the consumption of a large amount of helium. The wiggler could not be operated continuously with 5 Tesla. The wiggler has been operated at 4 Tesla with helium consumption of 1.1 L/h for experiments since October 1989. The duct will be improved during summer 1990.

K. Ohmi & M. Katoh

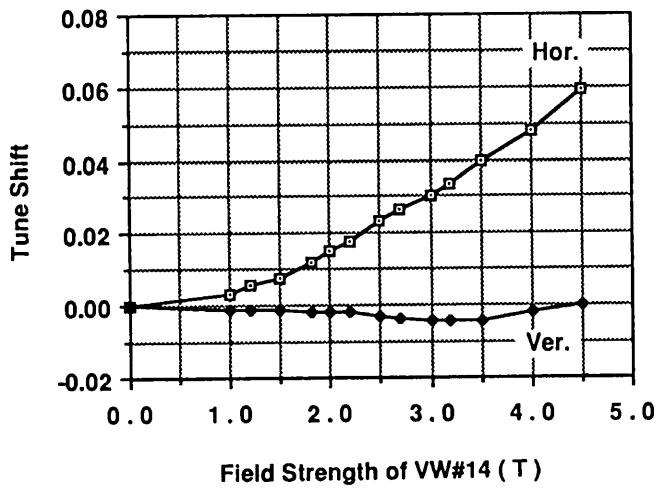

Fig. 23. Tune shifts vs. field strength of VW#14.

5b. Multipole Wiggler: MPW#13

A multipole wiggler, MPW#13, has been constructed and commissioned.[1-3] This device will deliver hard X-ray radiation while in its wiggler mode, and both vacuum ultraviolet and soft X-rays while in its undulator mode.

1) Construction

A hybrid configuration of Nd-Fe-B permanent magnets and a vanadium-permendur pole piece was adopted for generating a magnetic field of up to 1.5 T. The specifications of the magnetic component are listed in Table 4. The expected spectra are shown in Fig. 24. In the photon energy region from 1 to 30 keV, brilliancies 30 times as high as those of bending-magnet radiation can be obtained with the wiggler mode. For photons from 1 eV to 1 keV, brilliancies up to 100-times higher than those of bending-magnet sources can be obtained with the undulator mode using up to the 5th harmonics.

The magnetic components are mounted on 2 parallel stainless-steel I-beams, which can be moved along the vertical direction to control the magnetic field on the device axis. Most of the parts of the supporting frame of these I-beams and the magnetic components are made of stainless steel. For the supporting frame, techniques used for numerical control machines were adopted for the precise control of the gap width. The vacuum chamber is made of stainless steel and has pockets in which the pole pieces are placed so that the gap between the pole piece faces can be as close as 27 mm while ensuring the inner gap of the chamber to be 24 mm; this is necessary so as not to reduce the beam lifetime. The chamber is evacuated by two 60-l/s ion pumps and eight titanium sublimation pumps.

The magnetic field optimization was performed after mounting the magnetic components. The field strength of each magnetic pole was tuned with magnet rods, steel rods and/or steel bolts, so that the field distribution along the device axis could reach as close as possible to the ideal sinusoidal distribution over the full gap range. The tuning was repeated until the relative error of the absolute value of peak magnetic field became less than 0.4% over all gap range.

Table 4. Parameters of the device, MPW#13.

Number of poles, N_{pole}	27
Period length, λ_u	18 cm
Width of magnetic pole	12 cm
Gap between magnet poles	27 ~ 250 mm
(wiggler mode)	27 ~ 58 mm
(undulator mode)	77 ~ 225 mm
Magnetic field, B_0	0.02 ~ 1.5 T
(wiggler mode)	0.75 ~ 1.5 T
(undulator mode)	0.03 ~ 0.5 T
Deflection parameter, K	0.34 ~ 25
(wiggler mode)	13 ~ 25
(undulator mode)	0.5 ~ 8

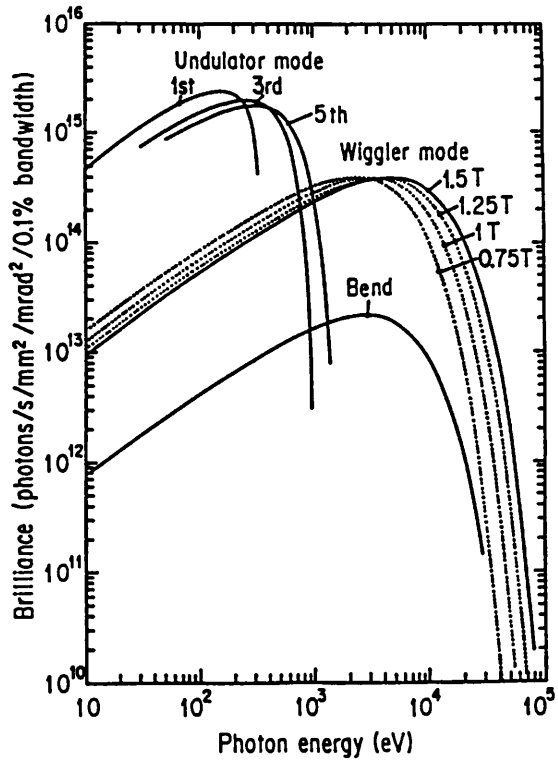

Fig. 24. Expected on-axis spectra of synchrotron radiation from MPW#13, calculated with the parameters in Table 4 and the ring parameters of σ_x=1.7 mm, σ_y=0.22 mm, $\sigma_{x'}$=0.15 mrad, and $\sigma_{y'}$=0.024 mrad. For the undulator mode, the curves represent traces of the peaks of the fundamental and higher harmonics, with the field scanned from 0.03 to 0.5 T.

Suppressing closed-orbit distortion (C.O.D.) was the next step of optimization. Current values supplied to the electro-magnets attached at both ends of the device were obtained so as to suppress the overall field integral and double integral along the device axis.

2) Commissioning

Machine studies of the storage ring were performed with the mutipole wiggler installed. There are two major influences of the device on the storage ring: tune shift and closed-orbit distortion. The tune shift was measured as a function of the peak magnetic field. As shown in Fig. 25, the tune shift is proportional to the square of the peak magnetic field of an insertion device according to the beam dynamics. This quadratic dependence was confirmed.

C.O.D. correction parameters were determined by minimizing the deviation of the values of the position monitors from a certain reference value at every gap setting. The values obtained in the magnetic-field optimization were taken as initial values for the C.O.D. correction study. The result of the final correction parameters for the C.O.D. is shown in Fig. 26.

S. Sasaki

References

1) S. Sasaki, S. Yamamoto, T. Shioya, and H. Kitamura: Rev. Sci. Instrum. 60, 1859(1989).
2) S. Sasaki, M. Hara, S. Yamamoto, T. Shioya, and H. Kitamura: RIKEN Accel. Prog. Rep., 21, 252 (1987).
3) S. Sasaki, M. Hara, S. Yamamoto, T. Shioya, M. Kato, and H. Kitamura: RIKEN Accel. Prog. Rep., 23, (1989), to be published.

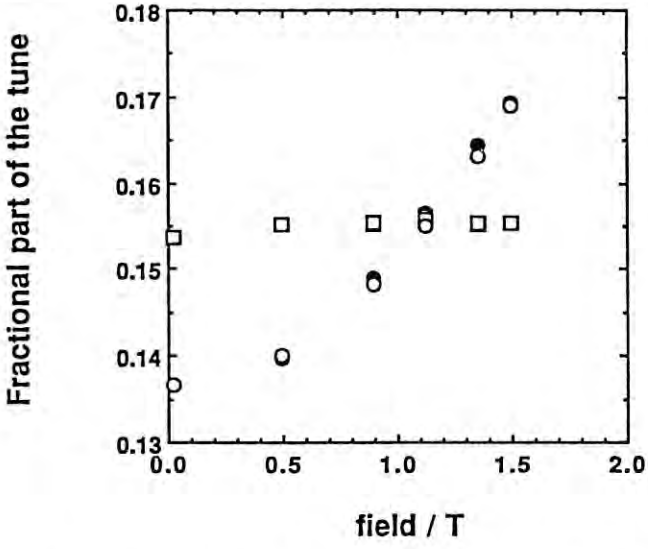

Fig. 25. Fractional part of the tune against the peak magnetic field of MPW#13. Closed circles, measured vertical tune, ν_y; open circles, calculated vertical tune, ν_{ycalc}; open squares, measured horizontal tune subtracted by 0.25, ν_x-0.25.

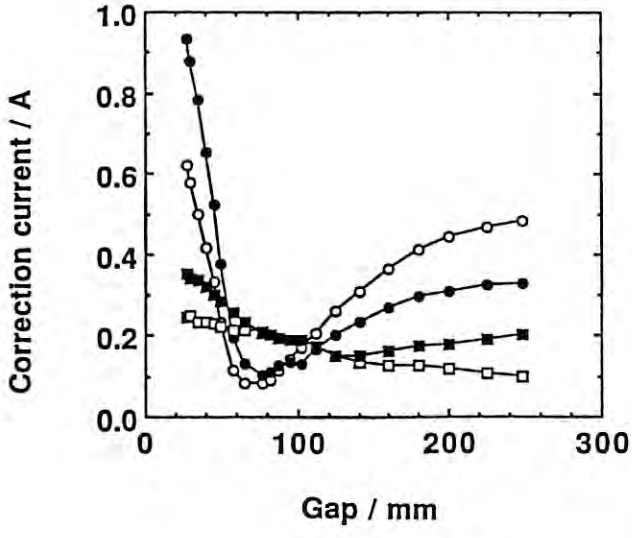

Fig. 26. C.O.D. correction current against the gap width. Open circles, upstream horizontal correction currents; closed circles, downstream horizontal correction currents; open squares, upstream vertical correction currents; closed squares, downstream vertical correction currents.

5c. Multipole Wiggler as a Source of Elliptically Polarized Radiation: EMPW#28.

For generation of intense circularly polarized synchrotron radiation, a multipole wiggler, EMPW#28, was constructed and installed during FY 1988. Studies for user's easy access to EMPW#28 have been under way. As a similar device, EMPW#NE1 had already been utilized as a strong source of circularly polarized hard x-rays[1,2] in the Synchrotron Radiation Facility at the TRISTAN Accumulation Ring.

The mechanism of EMPW#28 is based on a proposal for the generation of circularly polarized synchrotron radiation;[3] its structure is basically the same as that of EMPW#NE1 as reported in detail elsewhere.[1,4] EMPW#28 is shown in Fig. 27. The wiggler has horizontal and vertical pairs of permanent-magnet arrays with the period number of N=12 and the periodicity of λ_u=16cm in the pure Halbach-type configuration.[5] The magnets are made of Nd-Fe-B alloy with a remanent field of B_r=12kG and the coercivity of iH_c=17kOe. One pair generates a sinusoidal magnetic field with a phase difference of $\pm\pi/2$ relative to the other. The peak field strength is controllable by changing the magnet gap. The horizontal field ranges up to 2 kG and the vertical one up to 10kG. A relativistic electron travelling through EMPW#28 produces radiation with several thousand harmonics having quasicircular polarization over a wide energy range.[3] This is a direct result of the electron orbit of a deformed helix in the field given as a superposition of the above vertical and horizontal fields. The deflection parameter, which characterizes the radiation, is defined as

$$K_{x(y)} = 9.34 \times 10^{-5} B_{xo(yo)}\,(\mathrm{G})\,\lambda_u\,(\mathrm{cm}),$$

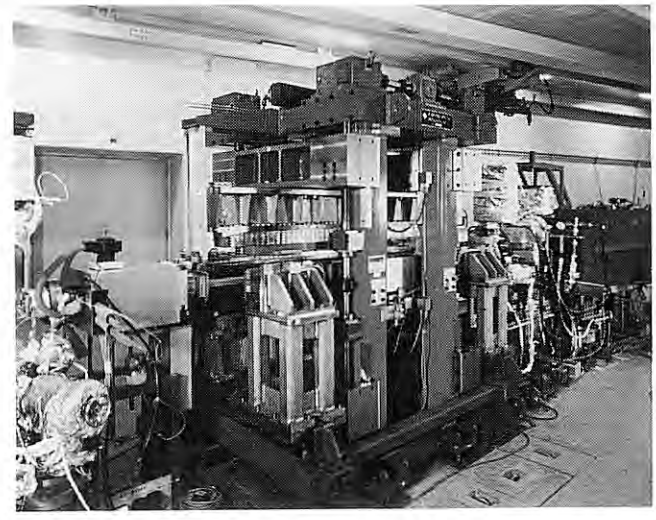

Fig. 27. Photograph of the multipole wiggler EMPW#28 constructed for the Photon Factory.

where K_y (K_x) is for the horizontal (vertical) deflection corresponding to the vertical (horizontal) field. A maximum value of K_y =15 is obtained with a peak vertical field of B_{yo}=10 kG at a minimum vertical magnet gap of 30mm, and a maximum of K_x =3 is obtained with a horizontal peak field of B_{xo}=2 kG at a minimum horizontal gap of 110 mm.

The radiation characteristics of EMPW#28 are illustrated in Fig. 28; the degree of circular polarization, P_c, and the brilliance are shown as functions of the photon energy for both undulator ($K_x \approx 1$ and $K_y \approx 1$) and wiggler ($K_x \approx 1$ and K_y =15) modes. These quantities were calculated[3,4] by taking into account the finite beam emittance in the PF ring. Radiation having a very high $P_c \geq 0.9$ is available as both the undulator and wiggler radiation, in the energy range from 20 to 10 keV. In the undulator mode, the brilliance is 10^3-times higher than that of linearly polarized radiation of PF bend sources, whereas in the wiggler mode the brilliance is about 30-times higher. EMPW#28 will serve as a new source in the region from VUV to soft x-rays.

S. Yamamoto

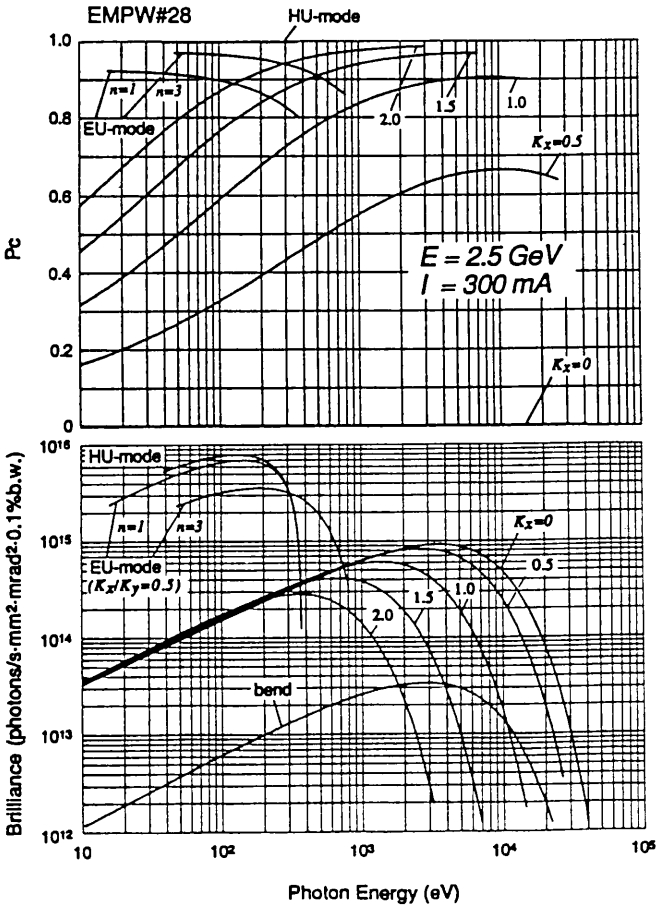

Fig. 28. Calculated spectral and polarization characteristics of the radiation from EMPW#28. Spectra in the undulator mode are shown for K_x/K_y = 0.5 as EU-mode, and for $K_x = K_y$ as HU-mode. Each curve represents a locus of the peak position of the radiation for the n-th harmonic. BM denotes radiation from a bending magnet. Curves with K_x = 0-2.0 denote the radiation in the wiggler mode (K_y = 15).

References

1) S.Yamamoto, Photon Factory Activity Report 1988, R14 (1989).
2) S.Yamamoto, H.Kawata, H.Kitamura, M.Ando, N.Sakai and N.Shiotani, Phys. Rev. Lett. 62, 2672 (1989).
3) S.Yamamoto and H.Kitamura, Jpn. J. Appl. Phys. 26, L1613 (1987).
4) S. Yamamoto, T. Shioya, S. Sasaki and H.Kitamura, Rev. Sci. Instrum. 60, 1834 (1989).
5) K.Halbach, Nucl. Instrum. Methods 187, 109 (1981).

5d. Trial Construction of an Undulator Using Metal-plated Permanent Magnets

Conventional and ordinary types of undulators have *a fixed aperture* for the circulating beam in a storage ring, since its magnetic field is applied to the beam through the ring-duct wall. The aperture of this type of undulator must be sufficiently wide so that the undulator can correspond to all operational modes of the ring, even if the wide aperture reduces the magnetic capability of the undulator.

If undulator magnets can be brought into a ring vacuum system the degrees of freedom to operate such an undulator and the ring would be largely enhanced. This is because the undulator aperture can be changed so as to satisfy the requirements for the storage-ring operation: (1) when the undulator radiation is used, the desired strength of the magnetic field can be obtained by closing the magnet gap, and (2) in the injection or other modes where a wide aperture is required, the desired field strength is obtained by opening the gap. In fact, when this type of undulator (hereafter, designated as the "in-vacuum" type undulator) is inserted in a storage ring of 6-8 GeV, it is possible to obtain undulator x-rays by adopting a short magnet periodicity of λ_u=2-4cm with a gap of the order of 1cm. This small gap is required for the generation of a sufficient strength of the magnetic field under the above values of λ_u.

In order to examine the vacuum compatibility and the magnetic characteristics of the in-vacuum type undulator, we have constructed a trial model. Its structure is shown in Fig. 29. This model undulator consists of a pair of arrays of metal-plated permanent magnets arranged in the pure Halbach-type configuration (λ_u=3cm and a number of periods,

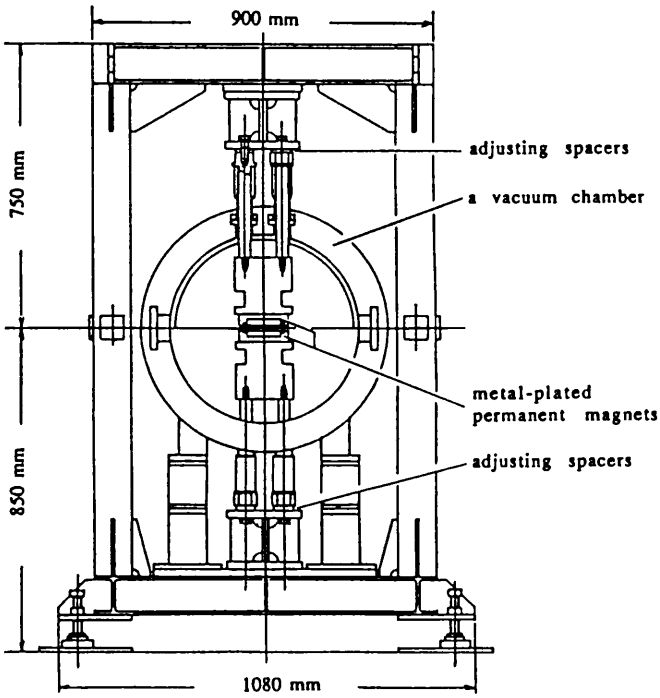

Fig. 29. Cross-sectional view of a trial in-vacuum-type undulator using metal-plated permanent magnets.

N=32), a vacuum chamber, and a mechanical frame which controls the magnet gap through linear motion feedthroughs using belows. A driving system is not included in the present model, and the magnet gap is controlled by changing the thickness of adjusting spacers. Each magnet block made of porous material is plated with Ni (25μm thick) and Cu (100 μm thick) for vacuum-sealing. With this sealing method, the effective aperture of the undulator is almost equal to the magnet gap. This is another advantage of the in-vacuum undulator using metal-plated magnets. As a magnet material, we have selected a Nd-Fe-B alloy with the remanent field of B_r=11kG and the coercivity of iH_c=21kOe (NEOMAX30SH manufactured by Sumitomo Special Metals Co. Ltd.) because of its high endurance against high temperatures. Demagnetization of magnets made of NEOMAX30SH is negligibly small over a range up to 120°C; the whole vacuum system must be baked out at a temperature for achieving an ultrahigh vacuum of 10^{-9} to 10^{-11} Torr.

The examination of the magnetic and vacuum characteristics of this in-vacuum undulator are now in progress. We summarize below the results of preliminary examinations using the sample magnets.

1) Vacuum properties

The vacuum compatibility of the plated magnets was examined on the sample blocks with a size of 8×6×30mm^3 of NEOMAX30SH (not magnetized). Each block is plated with Ni 25μm thick. The total surface area of the plated blocks is 1150 cm^2.

A test chamber with these sample magnets installed was evacuated at a pumping speed of 1000 l/s after a bakeout at 120°C for 48hrs. The pressures of the test chamber are shown in Fig. 30 as a function of pumping time with 1000 l/s; the open circles denote the vacuum of the empty chamber, and the crossed circles denote the vacuum with the sample magnets. The result shows that the ultimate pressure of the system with the plated magnets is one order-of-magnitude higher than that of the empty chamber. On the contrary, when the plated magnets were baked at 250°C for 24hrs, the vacuum compatibility of the plated magnets was satisfactory, as shown by closed circles in Fig. 30, even if they were exposed to the atmosphere for 3 days after the 250°C-baking. The surface area of the magnets used in the model undulator (Fig. 29) was about 10-times larger than that in this test. Therefore, even if the ultimate pressure (2 ×10^{-11} Torr) is caused by the outgassing from the plated magnets alone, the vacuum system of the model undulator could be evacuated down to 2 ×10^{-11} Torr by using an adequate pumping power. This pressure is satisfactory for a stable operation of the storage ring.

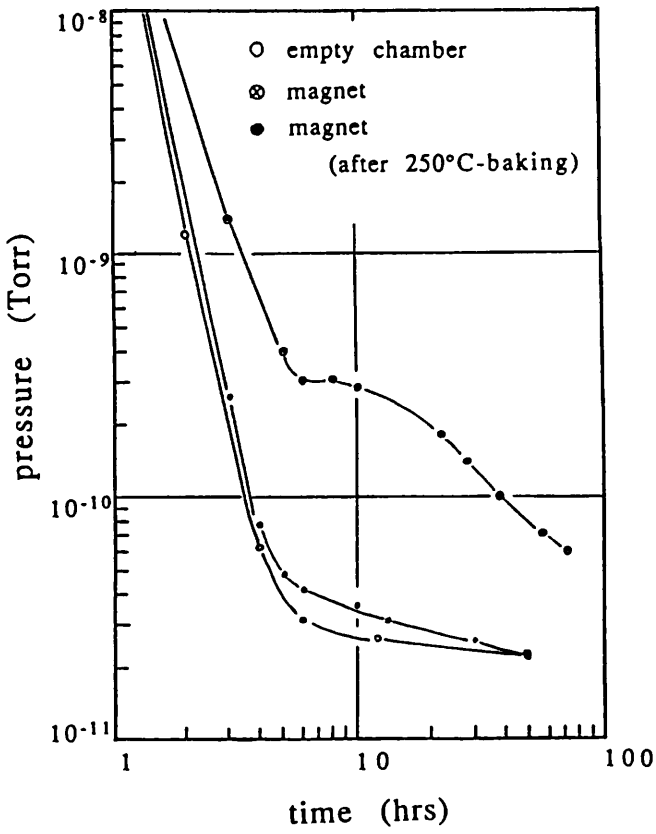

Fig. 30. Vacuum compatibility of Ni-plated sample magnets after bakeouts at 120°C and 48hrs. Open, crossed and closed circles denote, respectively, the property of the empty chamber, that without the 250°C-baking of the plated magnets, and that after the 250°C-baking.

2) Magnetic characteristics

As can be seen from the above section, it is important to study the high-temperature characteristics of magnets placed in the configuration in a real undulator, in which each magnet feels a strong magnetic field in a direction reversed to its own. In order to study the high-temperature characteristics of the magnets, we made several units of a single magnetic pole (made of NEOMAX30SH). Using a mirror-image effect, we can simulate the undulator field by surrounding a single-pole unit by the ferromagnetic plates (e.g. Fe plate). The field strength was measured by a Hall generator placed on the center of the Fe plate which opposes the pole face. Figure 31 shows the results of a cyclic heat treatment for the single-pole units (A to D); the field strength measured after each treatment (heating at 120°C or 125°C for 24hrs) is shown as a function of a cycle number. The reduction in the field strength is relatively large during the first cycle, but is negligibly small after the second cycle (about -0.02 to 0.00% at 120 to 125°C). This result strongly suggests that the field deterioration at high temperatures (up to 120-125°C at least) could be avoided by a heat treatment at the same temperature in advance. Thus, the deviation from the ideal field which is obtained by adjusting the undulator magnets could be suppressed during the baking process for a ultrahigh vacuum, once the magnets were heated before any adjustment.

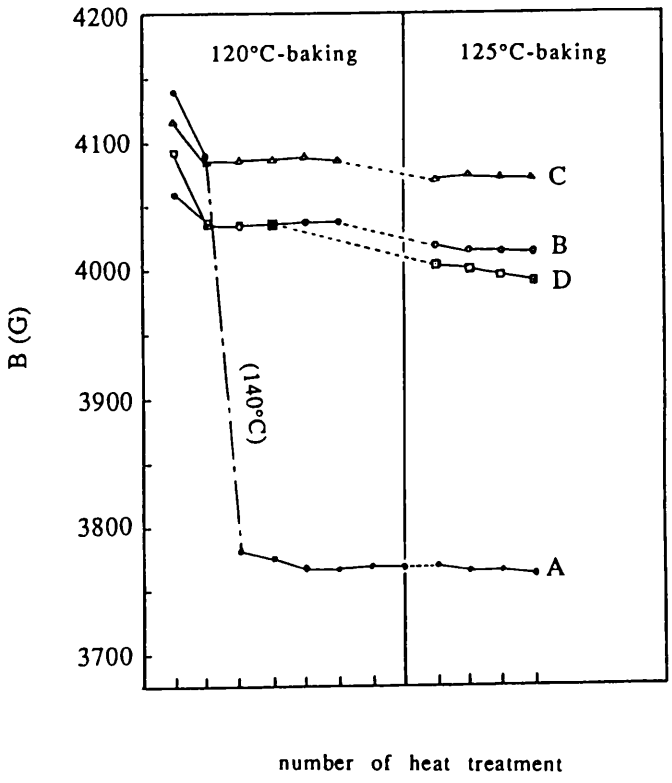

Fig. 31. Effects of cyclic heat treatments (heating at 120°C or 125°C for 24hrs) on the magnetic field of the simulated undulator field (see text). Each temperature shows the temperature at which the heat treatment was carried out.

In the present construction of the trial in-vacuum undulator we started examination and adjustment processes of the magnetic field after a heat treatment at 120°C. Each plated magnet had already been magnetized after outgassing at 250°C. The magnetic field will be examined after a bakeout at 120°C for achieving an ultra-high vacuum, and compared with the result before the bakeout. The results will be reported in the near future.

S. Yamamoto

6. MONITOR

A further study on the relation between diurnal beam motion and building distortion was made. In addition, a new feedback system was constructed to suppress horizontal diurnal orbit movement (see the previous issue of this report for a stabilizing system of vertical beam orbit).

6a. Measurement of Storage Ring Distortion[1)]

The shape of the horizontal orbit, being displaced diurnally from its reference orbit, resembles that of a dispersion function in the ring, where the orbit displacement was measured with 45 beam position monitors. We interpreted this fact as an effect due to an expansion of the ring building and carried out a preliminary measurement of the building expansion for a portion of the ring circumference. The distance between bending magnets B02 and B03 located near a long straight section was measured by using a high-precision laser measuring machine. The result is shown in Fig. 32. The total amount of the ring expansion from 7:00 to 16:00 was estimated to be about 1.8mm, by assuming that the expansion rate is constant over the ring circumference (187 m). By using relation between the ring circumference and the horizontal orbit displacement, the ring expansion was also estimated to be about 1.2mm, which agrees well with the result obtained above from the distance measurement.

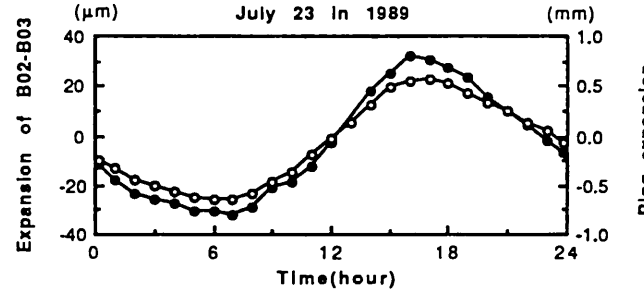

Fig. 32. Measured expansion between bending magnets B02 and B03 (filled circles) and expansion of the ring circumference obtained from the horizontal orbit displacement (open circles).

The diurnal vertical orbit displacement was dominated by the third-harmonic component associated with the vertical betatron tune of about 3.1. Speculating that some magnets were displaced owing to building distortion, we surveyed the vertical displacements of quadrupole magnets with a WILD N-3 precision optical level. Two quadrupole magnets (Q012 and Q013) located at both ends of the undulator were chosen. The displacement of Q013 relative to Q012 is shown in Fig. 33. The time dependence of the magnet displacement is similar to that of the diurnal beam motion.

These results support the speculation that the diurnal orbit motion resulted from a distortion of the ring building. However, the extent of this measurement was still limited. A measurement of the distortion over the entire ring is under way in order to obtain more quantitative consistency with the diurnal orbit movement.

K. Haga & N. Nakamura

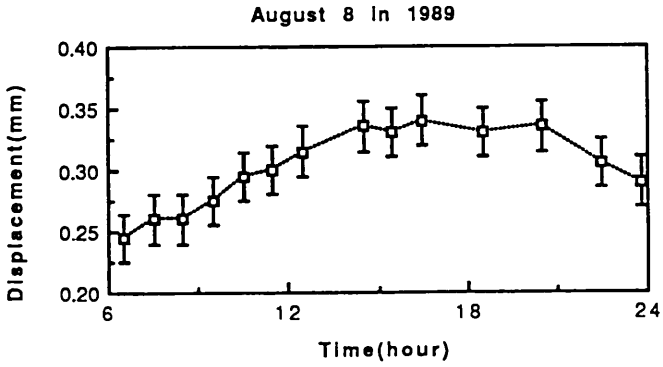

Fig. 33. Relative vertical displacement of two quadrupole magnets.

6b. Feedback System for Horizontal Orbit Movement[2)]

We made a horizontal feedback system in order to stabilize the horizontal orbit. In this system, expansion and contraction of the ring circumference are compensated by varying the RF frequency. The horizontal closed orbit is measured every ten minutes with position monitors. The difference(Δx_i) between the horizontal closed orbit and its reference orbit was minimized by changing the RF frequency(f_{RF}) as

$$\frac{\Delta f_{RF}}{f_{RF}} = \alpha \Sigma \frac{\Delta x_i \eta_i}{\eta_i^2} \qquad (i=1,2,\ldots,45),$$

where η_i is the dispersion function at the i-th position monitor and α is the momentum compaction factor. Figure 34 shows the horizontal orbit displacements with and without feedback. The feedback system has reduced the horizontal orbit displacement by a factor of five.

K. Haga & N. Nakamura

References

1) N. Nakamura, A. Araki, K. Haga, Y. Kamiya, T. Katsura and Y. Inoue, Submitted to the 14th Int. Conf. on High Energy Accel. 1989, Tsukuba, Japan.
2) K. Haga, Y. Kamiya, M. Katoh, T. Katsura, T. Mitsuhashi and N. Nakamura, Submitted to the 14th Int. Conf. on High Energy Accel., 1989, Tsukuba, Japan.

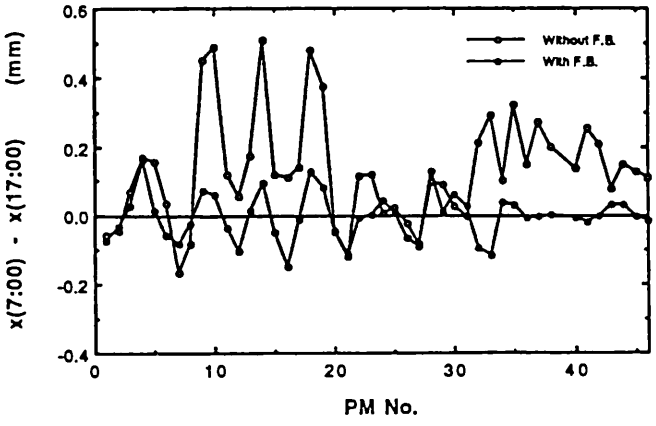

Fig. 34. Horizontal orbit displacements with and without the feedback system.

6c. Test of Beam-Position Feedback System for Beamline NE-5 of the TRISTAN Accumulation Ring

1) SR Beam Position Monitor and Observation of Beam Position Fluctuations on beamline NE-5

A split-cathode photoemission chamber(SEC) was employed for BL-NE-5.[1)] The monitor is located 5 m away from the source point, as shown in Fig. 35. Because the guide duct for the SR beam on BL-NE-5 was not evacuated, the SEC was mounted in a small vacuum chamber which was evacuated down to a pressure of about 1 Pa with a rotary pump. The chamber has a 1 mm-thick aluminum window for the SR beam to go through.

Observed fluctuations of the SR beam position are shown in Fig. 36. The SR beam drifted by 300 to 500 μm for about 30 min after acceleration from 2.5 to 5.8 or 6.0 GeV. Ripples of 20 to 30 μm were also observed. As a first step to identify the origins of these fluctuations, we measured the temperature variation of the cooling water at the outlet of the coil of a bending magnet and a quadrupole magnet. The result is also shown in Fig. 36. The SR beam position and the cooling-water temperature show a similar time dependence. However, the cause-and-effect relation between them is not clearly understood yet.

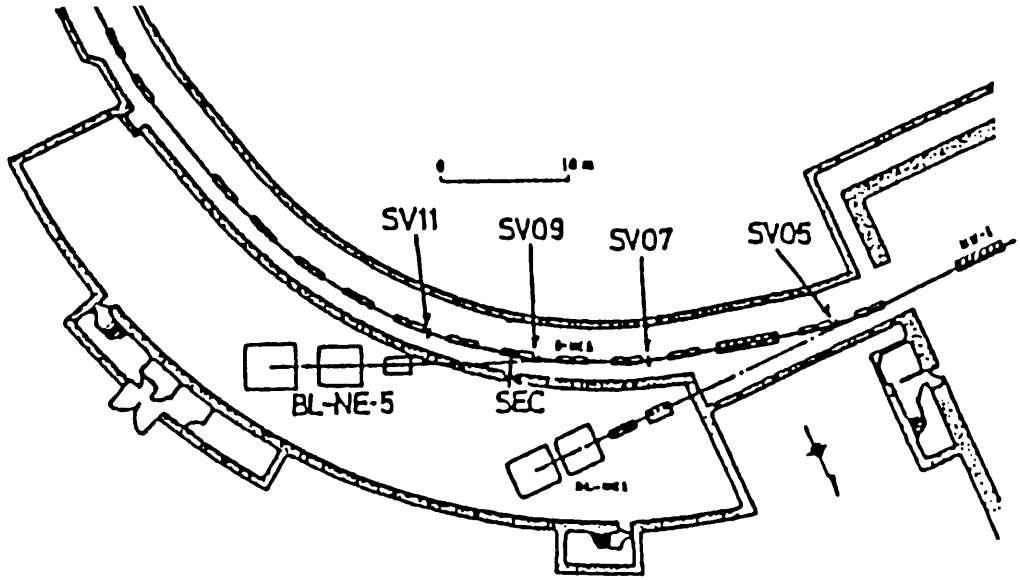

Fig. 35. Location of the SEC and the correctors.

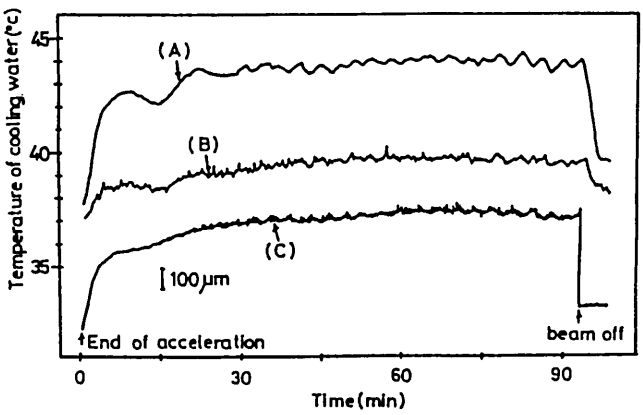

Fig. 36. Fluctuations of the SR beam position and the cooling-water temperature of magnets. (A) temperature at the outlet of a bending magnet coil, (B) temperature at the outlet of quadrupole-magnet coil and (C) SR beam-position fluctuations.

2) Stabilization of the SR Beam Position by an Orbit-Bump Feedback

Stabilization of the SR beam position by an orbit-bump feedback system was tried for 5.8 GeV operation in the SR mode. The system controls the SR beam position by steering the slope of the electron orbit at the source point.

The four correctors (SV05, SV07, SV09 and SV11) shown in Fig. 35 are usually used to correct the closed orbit distortion (COD) and produce an orbit bump at the source point. The angular resolution of the steering control at the source point has been estimated to be ±2 μrad at 5.8 GeV. The feedback program is executed on the control computers of the TRISTAN accelerators. The present response time of the feedback loop is about 30 sec. A result of the orbit feedback is shown in Fig. 37. When the feedback system is activated, the variation of the SR beam position remains within ±50 μm.

T. Mitsuhashi

References

1) T. Mitsuhashi, K. Haga and T. Katsura, Proce. of the 1988 IEEE Particle Accel. Conf., p.576(1988).

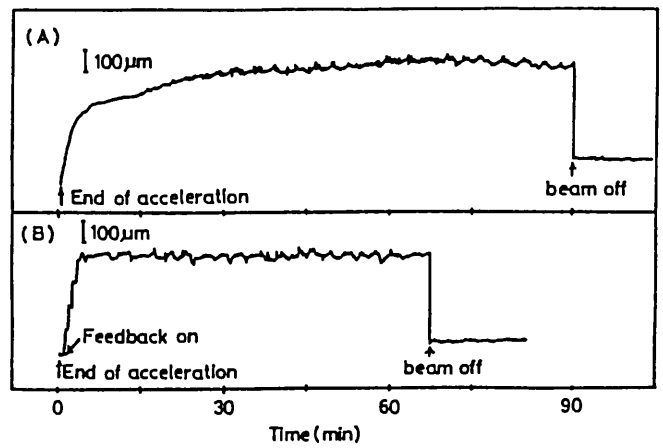

Fig. 37. Stabilization of SR beam position (A) without feedback and (B) with feedback.

7. CONTROL

7a. Database for Operation Logging

We applied a relational database (RDB) to an operation logging system of the PF storage ring since RDB has great flexibility and can be easily constructed and maintained.

Data collected during operations are transferred from the front-end control computers to a large main-frame computer (FACOM M-360MP from Fujitsu) through a network.[1] A master job which is always active in the large computer receives the classification codes of data to be received; it then initiates the related receiver jobs. The latter jobs actually receive data and store them into the proper entries of the database.

We used the AQL (Advanced Query Language)[2] for defining, manipulating and controlling data in the RDB. The AQL is very similar to SQL (Structured Query Language),[3] which is becoming, it seems, the standard in the RDB world. AQL is a command language which can be used directly from a terminal or in an application program. On-line programs for data saving and off-line programs for data retrieval are written using FORTRAN77 with "embedded" AQL statements.

As interactive software tool, ILM (Interactive Log data Manager), was developed in order to retrieve databases and to make graphic representations of results without requiring any special programming ability.

How to use the ILM:

- First define a time range to search by typing in dates and times.
- The beam current is then plotted and the existence of available data is displayed below for the selected time range (Fig. 38).
- It is possible to re-define the time range by setting a graphic cursor on the picture (if necessary).
- Select the type of graphic plot (time trend, correlation,···).
- Define the kinds of data to be retrieved by typing data names.
- Define the search condition (if necessary).
- The result of a data search is plotted (Fig. 39).

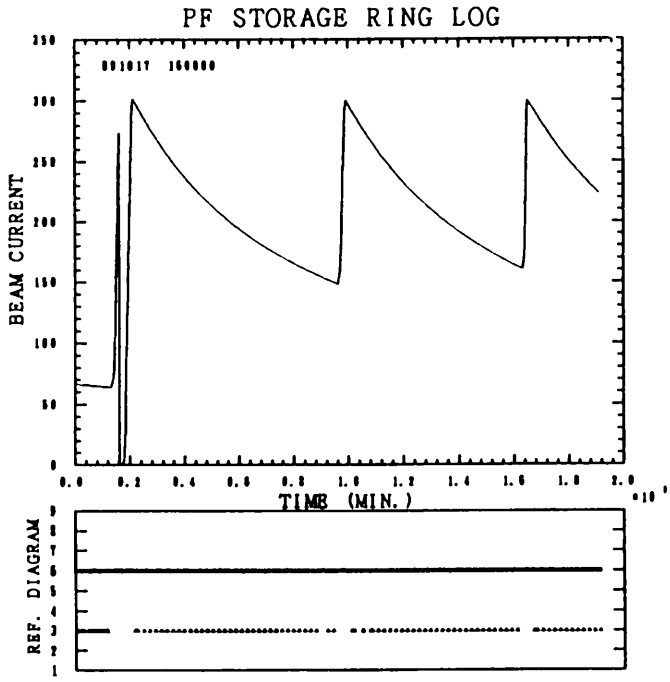

Fig. 38. Beam current plots and data reference diagram. A small triangle of "REF. DIAGRAM" represents an existence of available data. Number 3 corresponds to beam position data and 6 to rf data.

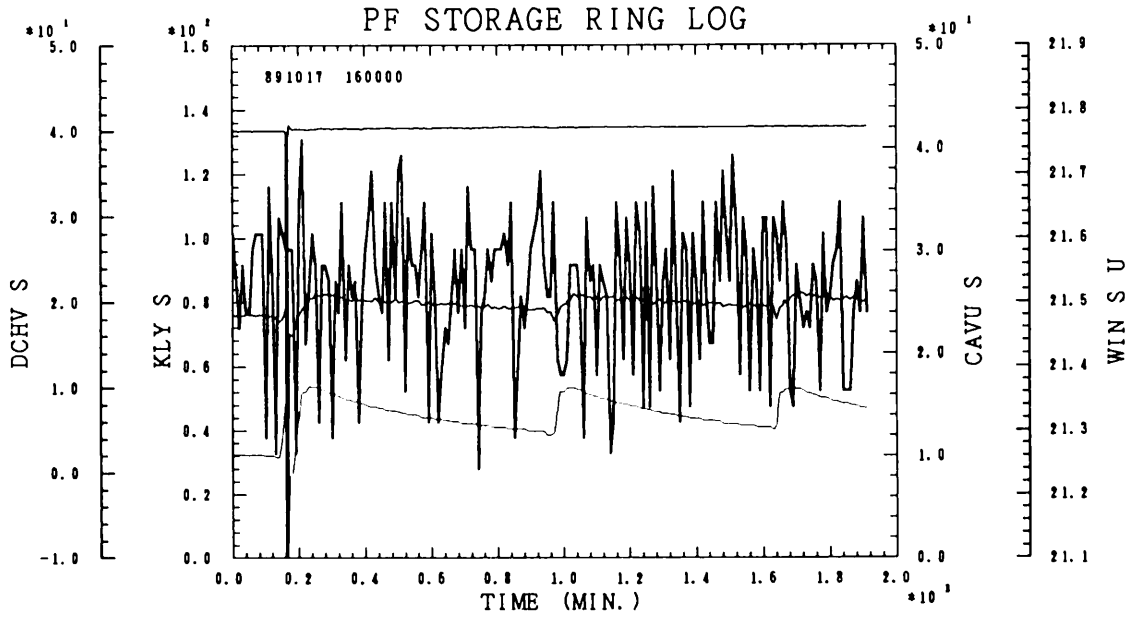

Fig. 39. Plot example by the ILM: klystron power, cavity power, dc high voltage and temperature of cooling water of rf system are plotted on a same time scale. Original plots are distinguished by colors.

- It is also possible to edit the obtained graph, for example, by changing scales, sizes or other graphic attributes using editor commands.

The ILM was developed on the basis of a utility called GRAPHMAN (Graphic Man-machine interface for Scientific Calculation Results),[4] which comprises a set of commands for such activities as calculation, executing control and graphic manipulation. The GRAPHMAN is available for both interactive and batch use. It accepts external commands in the form of a load module written in a high-level language. The essence of the ILM is a set command macros of GRAPHMAN, including external modules written in FORTRAN77 with embedded AQL.

At present, data concerning the rf and beam orbit are logged. The rf data are stored at a rate of 400 bytes every 10 minutes under stable operation (storage stage), and more frequently under a transient state (injection stage). The beam orbit data are saved at a rate of 2 kbytes every 10-30 minutes. The daily data acquisition rate is typically 300 kbytes It will not be long before data on vacuums, magnet power supplies and other important items are also available. The final acquisition rate is expected to be more than 1 Mbytes per day.

There are several possible ways for refining the database system: database tuning, subdividing large tables into hierarchical structures, using ordinary files indexed by keys in the database and increasing the computing power.

C.O. Pak

References

1) C.O. Pak, Nucl. Instr. Meth. A277 (1989) 501.
2) Fujitsu Limited, AIM/RDB Reference manual, 70SP-4583-1 (1989) in Japanese.
3) There are many references about the SQL. For example, C.J. Date, A guide to the SQL Standard (Addison-Wesley, 1989).
4) Fujitsu Limited, GRAPHMAN users manual, 78AR-5170-3 (1989) in Japanese.

8. BEAM CHANNEL

The main beam lines as of FY1989 are summarized in Table D-12. Beam lines BL-3, BL-13, BL-18, and BL-28, which were under construction in FY1988, have been into operation this fiscal year. Two new beam lines, BL-20 and BL-27, are currently being designed.

8a. New Beam Lines

Beam line BL-20 is being designed to extract a 35-mrad horizontal fan of synchrotron radiation which is divided among two branch lines BL-20A and BL-20B. Branch line BL-20A is intended for high-resolution high-flux VUV spectroscopic studies, utilizing 28 mrad of radiation. A first-mirror chamber will be installed in the ring tunnel to accept the large horizontal fan of the beam. A 3-m normal-incidence monochromator is now under design, with provision for a possible future accommodation of a grazing-incidence monochromator. Branch line BL-20B is intended for use in x-ray experiments. A double beryllium-window assembly is to be attached at the downstream termination of the front end. The construction of BL-20B is expected to be funded by the Australian Government, though no final decision has been made yet.

The design of beam line BL-27 is a joint project between Japan Atomic Energy Research Institute and the Photon Factory. The beam line is intended for exclusive use for experiments on radioactive substances such as actinide compounds, materials irradiated by electron or heavy-ion beams etc. Radiation detectors as well as many diaphragms will be installed in the beam line to prevent pollution with radioactive materials. Beam line BL-27 is designed to have two branches BL-27A and BL-27B. BL-27A, which will utilize a 5-mrad horizontal divergence of the beam, is a soft x-ray branch line for photoemission experiments and radiation effects on biological species with RI tracer elements. BL-27B is an x-ray branch line expected for use in EXAFS and diffuse-scattering experiments, using a 4 mrad of radiation.

8b. Temperature Measurements of Beryllium Windows in Multipole-Wiggler Line BL-16

Multipole wigglers produce total powers two orders-of-magnitude higher than those generated by bending magnet sources. Handling the intense power is essentially important in the design of beam-line components of the front end.[1] Temperature measurements have been made for beryllium windows in multipole-wiggler line BL-16.

Figure 40 shows a schematic of a graphite foil/beryllium window assembly.[2] Six graphite foils are placed upstream of two beryllium windows to reduce the thermal loads on the beryllium foils. The temperature rise was measured for upstream beryllium window B_1 with an infrared camera and for edges of two windows B_1 and B_2 with thermocouples attached to their support frames. The temperature was also measured for water cooling the entire assembly. Figures 41(a) and 41(b) show the temperature distribution in window B_1 and the temperature rise of each portion as a function of ring current, respectively. The measurement for B_1 (Fig. 41(a)) was made at a maximum wiggler field of 1.47 T. The increase in temperature is seen to be nearly proportional to the ring current, as naturally expected. However, a saturation was observed at high currents, the reason for which is not clear at present. The observed rise in water temperature indicates that powers only up to 1 KW were removed by flowing water. The temperature of the beryllium windows is too high to maintain their high performance and the heat-removal mechanism should be improved.

T. Koide

References

1) T. Koide et al., Rev. Sci. Instrum. 60, 1877(1989).
2) S. Sato et al., Rev. Sci. Instrum. 60, 1965(1989).

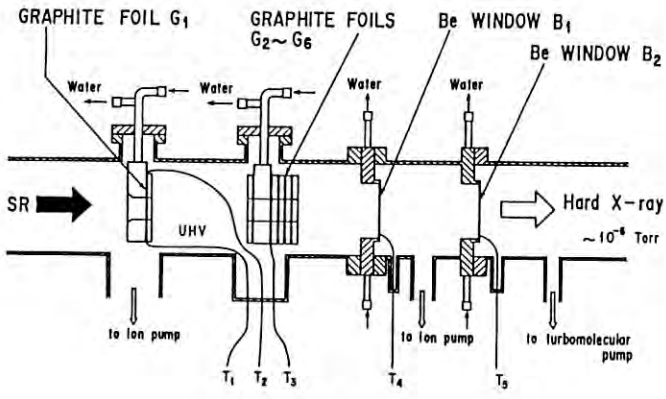

Fig. 40. Configuration of beryllium-window assembly.

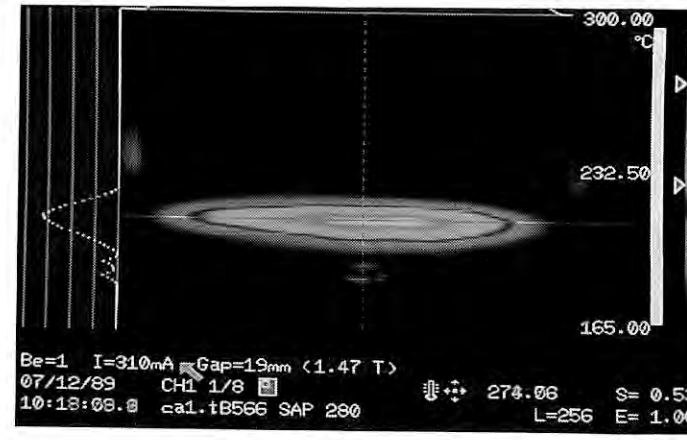

(a)

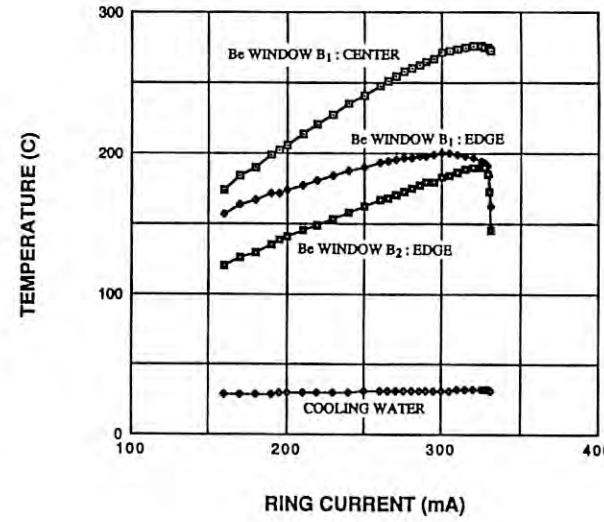

(b)

Fig. 41. (a) Temperature distribution in the upstream beryllium window measured with an infrared camera. (b) Temperature rise of beryllium windows B_1 and B_2 and cooling water as functions of ring current.

D. LIGHT SOURCE SPECIFICATIONS

This section contains major specifications of the PF and AR rings to provide quick and handy information for users and machine physicists.

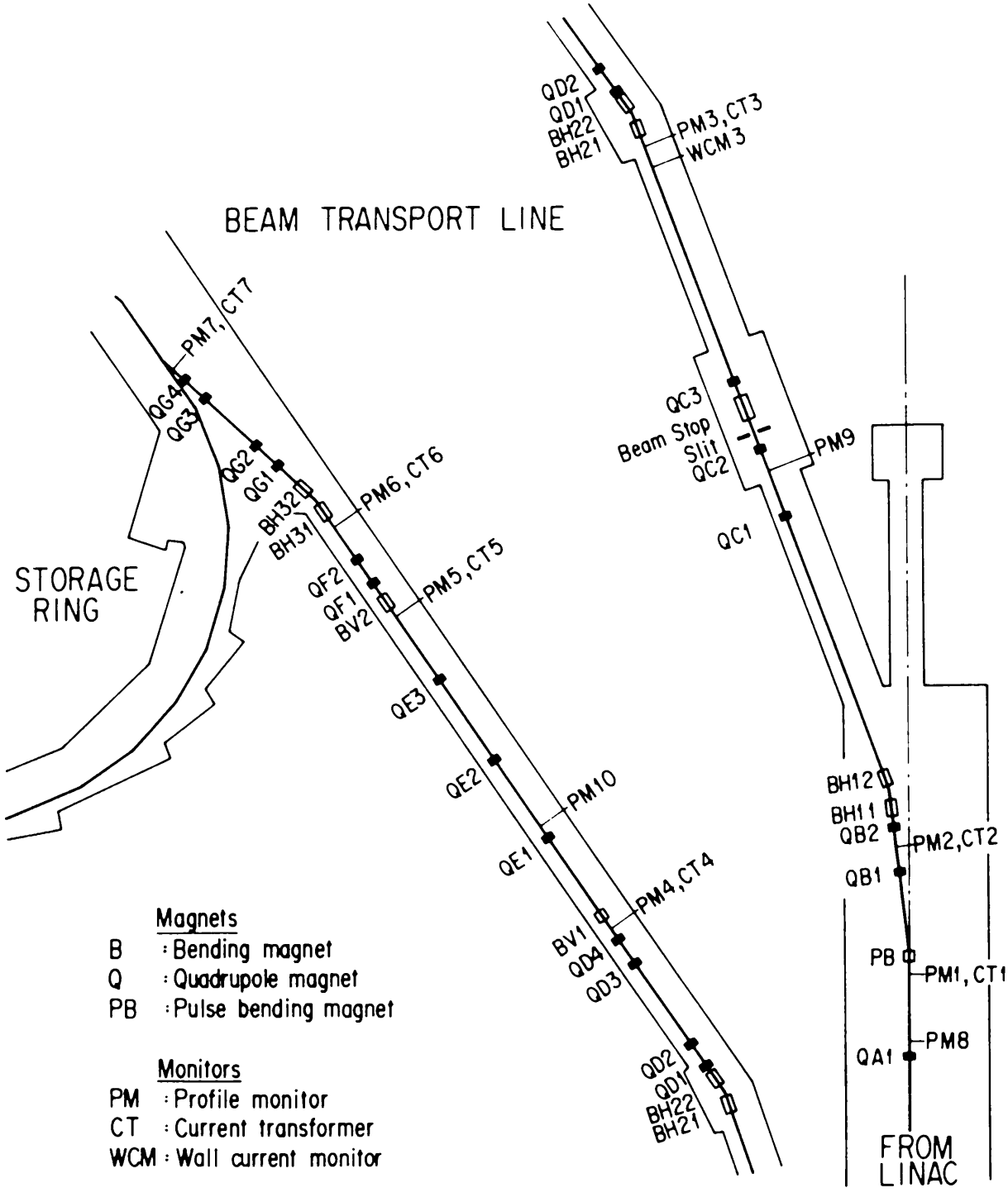

Fig. D-1. Beam transport line.

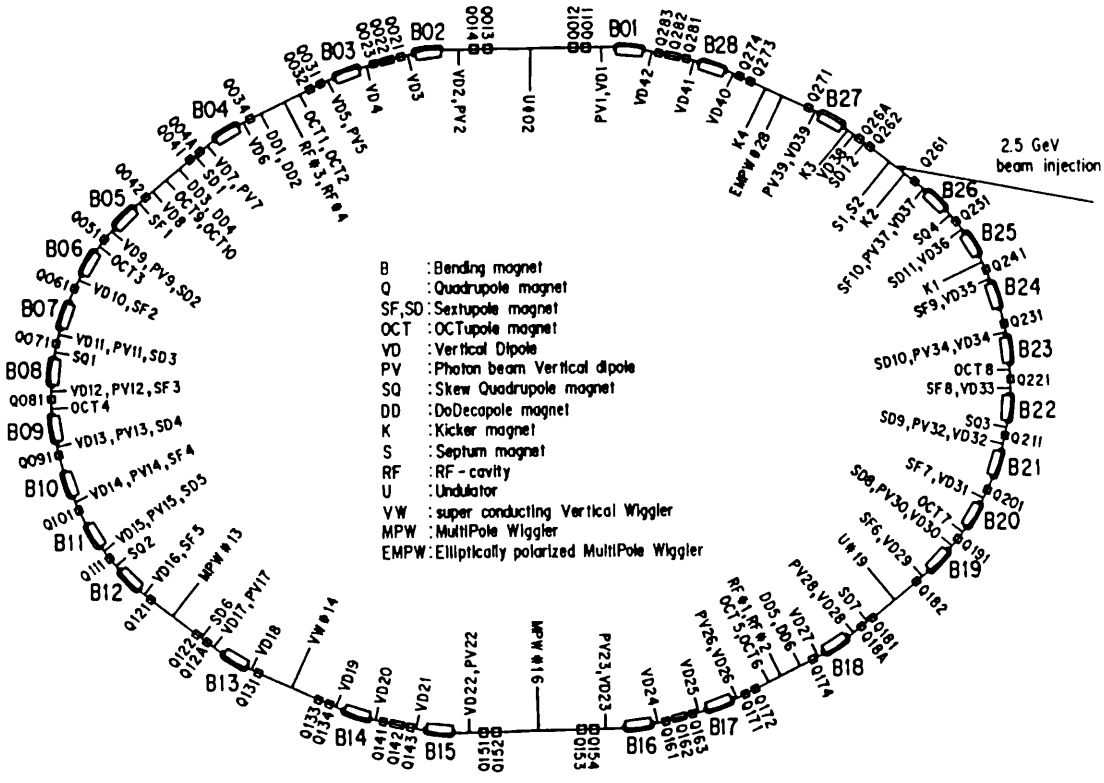

Fig. D-2. Ring lattice components.

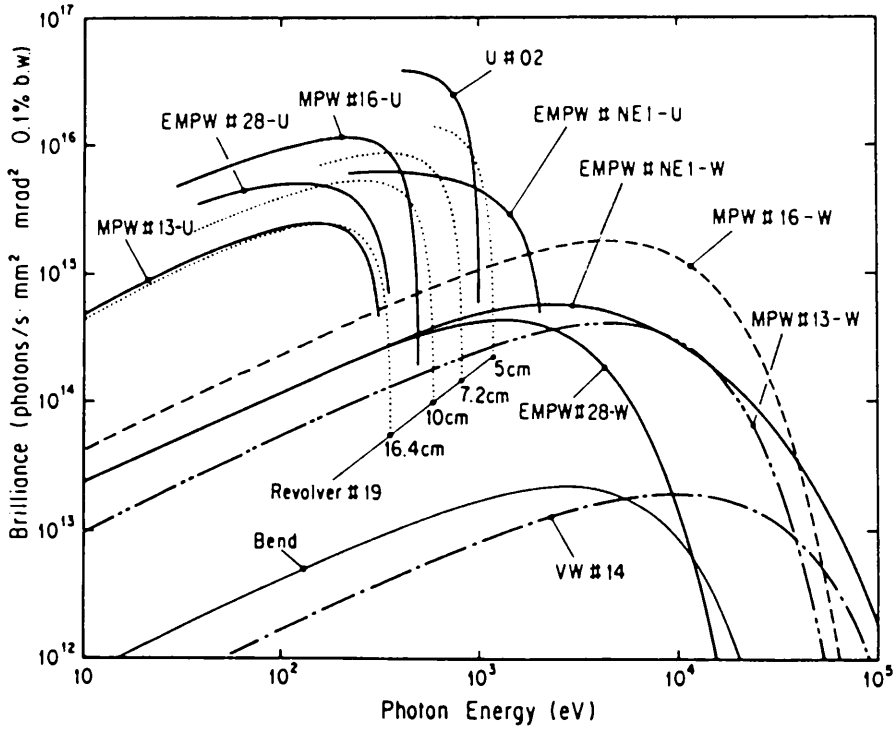

Fig. D-3. Synchrotron radiation spectra.
Brilliance of radiation vs. photon energy for the insertion devices (U#01, MPW#13, VW#14, VPW#16, Revolver#19 and EMP#28) and the bending magnet (Bend) of the PF, and for the insertion device (EMPW#NE1) of the AR. The name of each source is assigned in Table D-1. Several insertion devices have both undulator and wiggler modes, which are denoted by U or W, respectively. The spectral curve of each undulator (or undulator mode of multipole wiggler) is a locus of the peak of the first harmonic within the allowable range of K-parameter. Spectra of Revolver#19 are shown for four kinds of period lengths.

Table D-4. Insertion devices.

Calculated spectra from the bend source and 6 insertion devices, and one insertion device at the PF E/I: beam energy and current, λ_u: period length, N: number of periods, L: length of undulator or wiggler, $G_y(G_x)$: minimum vertical (horizontal) gap height, $B_y(B_x)$: maximum vertical (horizontal) magnetic field, P: pure configuration, H: hybrid configuration, S.C.: superconducting magnet, $\sigma_{x,y}$: horizontal or vertical beam size, $\sigma_{x,y}$: horizontal or vertical beam divergence, $K_y(K_x)$: horizontal (vertical) deflection parameter, $\varepsilon_1/\varepsilon_c$: photon energy of the first harmonic and critical energy of band source or wiggler, P_c: degree of circular polarization, : brilliance (photons/s·mm^2·mrad^2·0.1%b.w.), P_T: total radiated power, P_D: angular power density (kW/mrad^2). Different operating modes of undulator and wiggler are denoted by U and W, respectively.

Name	E/I GeV/mA	λ_u cm	N	L m	$G_y(G_x)$ cm	$B_y(B_x)$ T	Type of magnet	σ_x mm	σ_y mm	$\sigma_{x'}$ mrad	$\sigma_{y'}$ mrad	Energy range keV	$K_y(K_x)$	$\varepsilon_1/\varepsilon_c$ keV	ℬ	P_T kW	P_D
Bend	2.5/250							0.75	0.33	0.39	0.047	<30		4.0	2.1E13		0.043
U#02		6.0	60	3.6	2.8	0.3	P($SmCo_5$)	0.63	0.22	0.20	0.017	0.4～3	1.7	0.40	3.7E16	0.33	1.3
MPW#13-W		18.0	13	2.5	2.7	1.5	H(NdFeB)	1.65	0.21	0.15	0.023	<70	25.0	6.2	4.4E14	5.0	2.1
-U												0.03～1	1.0	0.22	2.0E15	0.01	0.042
VW#14					5.0	5.0	S.C.	1.17	0.15	0.19	0.026	<100		20.8	1.6E13	8.8	0.17
MPW#16-W		12.0	26	3.1	1.9	1.5	H(NdFeB)	0.63	0.22	0.20	0.017	<70	16.8	6.2	1.8E15	7.1	4.5
-U												0.03～1	1.0	0.33	9.4E15	0.02	0.12
Revolver		5.0	46	2.3	3.0	0.28	H(NdFeB)	1.65	0.21	0.15	0.023		1.3	0.64	1.3E16	0.18	0.89
#19		7.2	32			0.41	H(NdFeB)					0.007～1.1	2.7	0.18	7.3E15	0.37	1.3
		10.0	23			0.53	H(NdFeB)						5.0	0.044	2.5E15	0.66	1.3
		16.4	14			0.62	P(NdFeB)						9.5	0.0078	4.2E14	0.88	0.97
EMPW#28		16.0	12	1.9	3(11)	1(0.2)	P(NdFeB)	1.17	0.15	0.19	0.026						
-W												<15	15(1)	4.2(Pc=89%)	1.8E14	1.9	1.1
-U												0.04～0.35	1(1)	.18(Pc=99%)	4.0E15	0.02	0.069
EMPW#NE1		16.0	21	3.4	3(11)	1(0.2)	P(NdFeB)	0.95	0.08	0.14	0.053						
-W	6.0/50											<100	15/2	24(Pc=80%)	9.1E13	3.8	8.5
-U												0.2～2	1/1	1.1(Pc=97%)	3.5E15	0.03	0.52

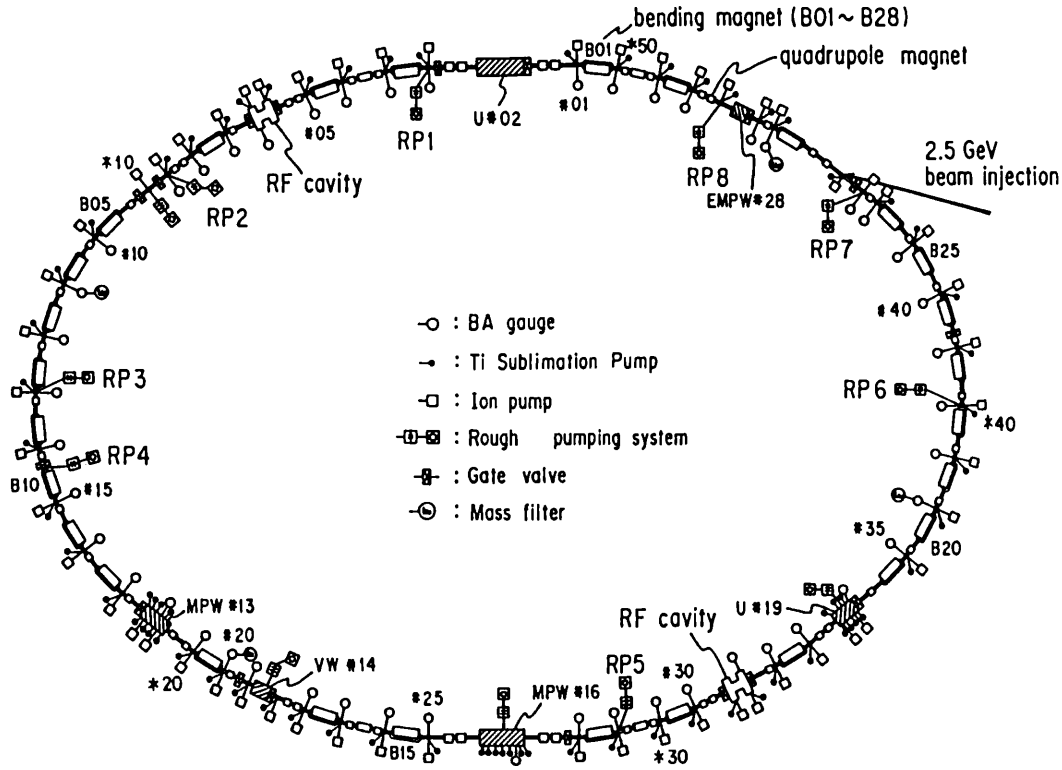

Fig. D-5. Vacuum system components.

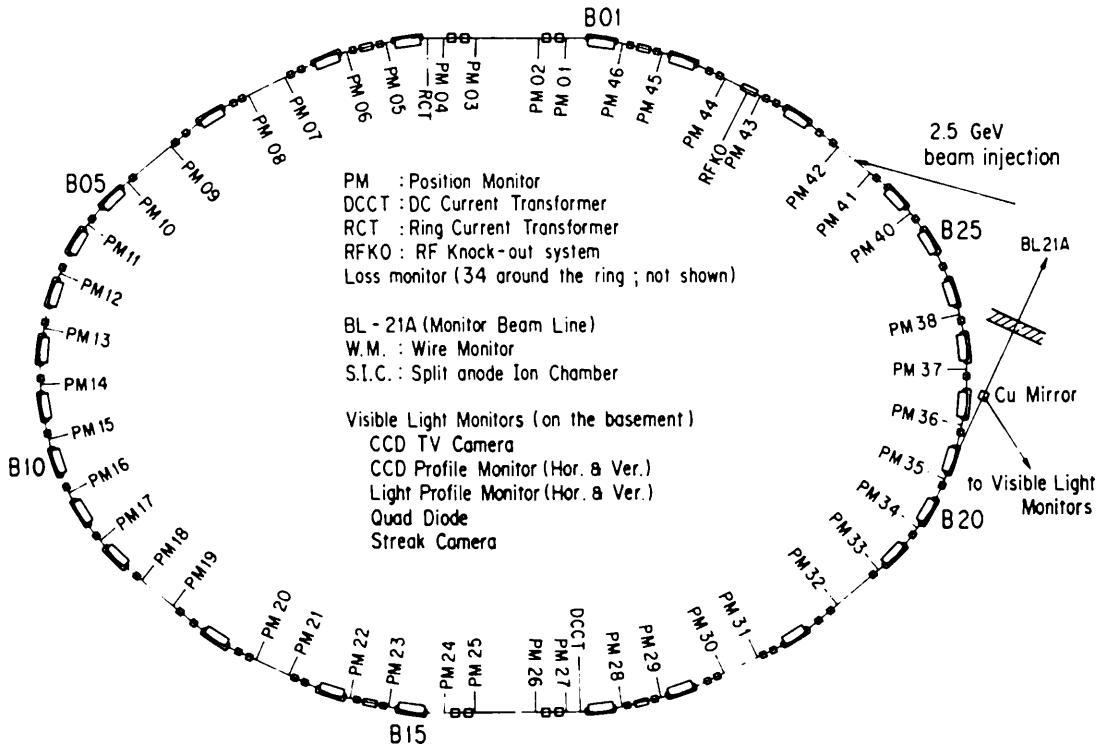

Fig. D-6. Beam monitors.

Table D-7. General parameters of the storage ring.

Energy	2.5 GeV	(1.6 GeV to 3 GeV)
Initial stored current	300 mA	(250 mA with vertical wiggler) (max. 360 mA)
Emittance	130nm·rad(horizontal) ~2nm·rad(vertical)	
Circumference	187m	(bending radius=8.66m)
RF frequency	500MHz	(harmonic number=312)
Injection	2.5GeV Linac	(positron/electron)
Beam lifetime	20 h (at 300 mA)	$I \cdot \tau \gtrsim 5.8$ A·h (at ~150 mA ~ 350 mA)
Vacuum pressure	3×10^{-10} Torr (at 300mA) $P/I \lesssim 1\times10^{-9}$ Torr/A (at ~150 mA ~ 350 mA) 3×10^{-11} Torr (at 0 mA)	
Insertion devices	Superconducting vertical wiggler 5T 60 period undulator K=1.78~0.1 26 period multipole wiggler/undulator 1.5T~0.04T Four way revolver type undulator 14 period multipole wiggler Elliptically polarized multipole wiggler	
SR channels	SR experiment 20 (5 under installation, 1 under design) Beam diagnosis 3	

Table D-8. Beam parameters.

Horizontal tune ν_x	8.38
Vertical tune ν_y	3.14
Compaction factor α	0.015
Natural chromaticity ξ_x	-15.8
ξ_y	-8.6
Bunch length σ_z	1.5cm
Transverse damping time	7.8msec
Longitudinal damping time	3.9msec
Energy spread	7.3×10^{-4}
Radiation loss	400keV

Table D-9. Principal parameters of the accelerator system.

Magnet system

	number of magnets	number of power supplies
Bending	28	1
Quadrupole	58	12
Sextupole	22	2
Octupole	11	10
Skew quadrupole	4	4
Dodecapole	6	6
Vertical steering	42	42
Photon beam steering	20	20
Others		
Backleg winding of bending magnet	28	
Electric shunt for tune compensation	12	

RF system

Number of RF stations	4
Number of klystrons	4 (180kW/klystron)
Number of RF cavities	4 (single cell cavity)
Shunt impedance	32MΩ (four cavities)
Unloaded Q	39000
Total power dissipated in cavity wall	89kW
Total cavity gap voltage	1.7MV
Synchrotron frequency	37kHz

Vacuum system

main pumping system

pump	pumping speed	number
SIP (Sputter Ion Pump)	128 l/sec	54
DIP (Distributed Ion Pump)	150 l/sec	26
Ti sublimation	---------	71
NEG (Non-Evaporable Getter)	---------	2

total effective pumping speed = 2×10^4 l/sec (for CO)

Rough pumping system

	pumping speed	number
TMP (Turbo Molecular Pump)	300 l/sec	12

Measurement

	number
B-A gauge	48
mass filter	4
cold cathode gauge	16 (for baking)

Sector gate valve

	number
all metal with RF shield	3
all metal without RF shield	4
Viton seal with RF shield	10

Injection system

Septum magnet

name	Septum I (S1)	Septum II (S2)
core material	laminated silicon steel (passive type)	
length [mm]	1500	1000
maximum current [A]	6000	6000
deflection angle [degree]	7.0	5.0
pulse width [μsec]	88	60

Kicker magnet

name	K1 , K2 , K3 , K4
core material	ferrite (window frame type)
core length [mm]	300
maximum current [A]	3500
maximum deflection angle [mrad]	4.4
pulse width [μsec]	5

Superconducting vertical wiggler

Maximum field strength on the beam orbit	5 Tesla
Magnet gap	66 mm
Magnet pole size (widthxhight)	40 mm × 260 mm
Number of magnetic poles	5 poles arranged every 200 mm
Rated exciting current	220 A at 5 Tesla
Superconducting wire	NbTi : Cu 1 : 1 size 1.70 × 0.85 mm^2
Cross section of coils	65 mm × 70 mm
Number of turn	2520
Liquid helium consumption in the permanent current mode	0.1 L/h
Damping rate of the permanent current	1.4×10^{-5}/h
Inductance	1.31 H/coil

Monitor system

PM(Position Monitor)	45
RCT(Ring Current Transformer)	1
DCCT(Direct Current Current Transformer)	1
RFKO(Radio Frequency Knock-Out system	1
LS(Loss monitor)	43
Visible Light Monitor	
CCD TV Camera	
CCD Profile Monitor (H&V)	1
Light Profile Monitor (H&V)	1
Quad Diode	1
BL-21A(Monitor Beam Line)	
W.M. (Wire Monitor)	1
S.I.C. (Split anode Ion Chamber)	1

Control system

		number	memory
Control computers	FACOM S-3500	4	16 Mbyte
Library computer	FACOM M-780/10R	1	32 Mbyte
Computer network (type : optical token ring) number of nodes = 5 (max. 256)			

D-10. Beam size and divergence at source point.

location	σ_x [mm]	σ_y [mm]	σ'_x [mrad]	σ'_y [mrad]
B15&B01	0.53	0.09	0.35	0.038
B02&B16	0.84	0.07	0.33	0.038
B03&B17	0.54	0.20	0.33	0.013
B04&B18	0.49	0.21	0.37	0.038
B05&B19	1.51	0.21	0.47	0.038
B06&B20	0.78	0.25	0.43	0.039
B07&B21	1.31	0.21	0.40	0.037
B08&B22	0.80	0.25	0.38	0.038
B09&B23	1.21	0.20	0.39	0.038
B10&B24	0.88	0.25	0.39	0.037
B11&B25	1.25	0.21	0.44	0.039
B12&B26	0.99	0.26	0.46	0.038
B13&B27	0.38	0.25	0.39	0.038
B14&B28	0.82	0.21	0.31	0.013

D-11. General parameters of the Accumulation Ring.

Energy		6.0 GeV (2.5 GeV to 8 GeV)
Initial stored current		20 mA (max. 50 mA)
Emittance		130 nm·rad (horizontal)
		~ 2 nm·rad (vertical)
Circumference		377 m
Long straight sections		2 × (19.5 + 19.1) m
rf frequency		508.6 MHz
Bending radius		23.2 m
Number of bending magnets		72
Energy loss per turn		4.85 MeV
Damping times	τ_x	3.11 ms
	τ_y	3.11 ms
	τ_E	1.56 ms
Partition numbers	J_x	1.0
	J_E	2.0
Natural energy spread		1.06E-3
Momentum compaction factor		7.1E-3
Natural chromaticity	ξ_x	-22.2
	ξ_y	-12.8

Table D-12. Summary of Beamline in FY 1989.

Beamline	Affiliation	Source	Spectral range	Status
BL-1	NTT	bending magnet (B1)	VUV and soft X-ray	in operation
BL-2	KEK-PF	60-period permanent magnet undulator	soft-X-ray	in operation
BL-3	KEK-PF	bending magnet (B3)	VUV and soft X-ray	in operation
BL-4	KEK-PF	bending magnet (B2)	X-ray	in operation
BL-5	KEK-PF	permanent magnet wiggler/undulator (under design)	VUV and soft X-ray	under installation
BL-6	KEK-PF	bending magnet (B6)	X-ray	in operation
BL-7	University of Tokyo	bending magnet (B7)	VUV and X-ray	in operation
BL-8	Hitachi Ltd.	bending magnet (B8)	VUV and X-ray	in operation
BL-9	Nippon Electrical Co. (NEC)	bending magnet (B9)	VUV and X-ray	in operation
BL-10	KEK-PF	bending magnet (B10)	X-ray	in operation
BL-11	KEK-PF	bending magnet (B11)	VUV and soft X-ray	in operation
BL-12	KEK-PF	bending magnet (B12)	VUV	in operation
BL-13	The Institute of Physics and Chemical Research*)	27-pole wiggler	hard X-ray	in operation
BL-14	KEK-PF	superconducting vertical wiggler	hard X-ray	in operation
BL-15	KEK-PF	bending magnet (B15)	X-ray	in operation
BL-16	KEK-PF	53-pole permanent magnet wiggler/undulator	soft X-ray	in operation
BL-17	Fujitsu Ltd.	bending magnet (B17)	VUV and X-ray	in operation
BL-18	ISSP and KEK-PF	bending magnet (B18)	VUV and X-ray	in operation
BL-19	ISSP and KEK-PF	permanent magnet multi-undulator	VUV	in operation
BL-20	KEK-PF	bending magnet (B20)	VUV and X-ray	under design
BL-21	KEK-PF	bending magnet (B21)	white, visible light and X-ray (branch line)	in operation
BL-27	Japan Atomic Energy Research Institute	bending magnet (B27)	soft X-ray and X-ray	under design
BL-28	KEK-PF	25-pole permanent magnet wiggler/undulator	circularly polarized VUV and soft X-ray	in operation
AR Test Port	KEK-PF	bending magnet of Accumulation Ring (AR)	hard X-ray	in operation
AR-BL-1	KEK-PF	41-pole wiggler	hard X-ray and soft X-ray	in operation

*) Branch lines are constructed by following national institutes; National Research Laboratory of Metrology, National Institute of Researches in Inorganic Materials, Electrotechnical Laboratory, and National Chemical Laboratory for Industry

Instrumentation Division

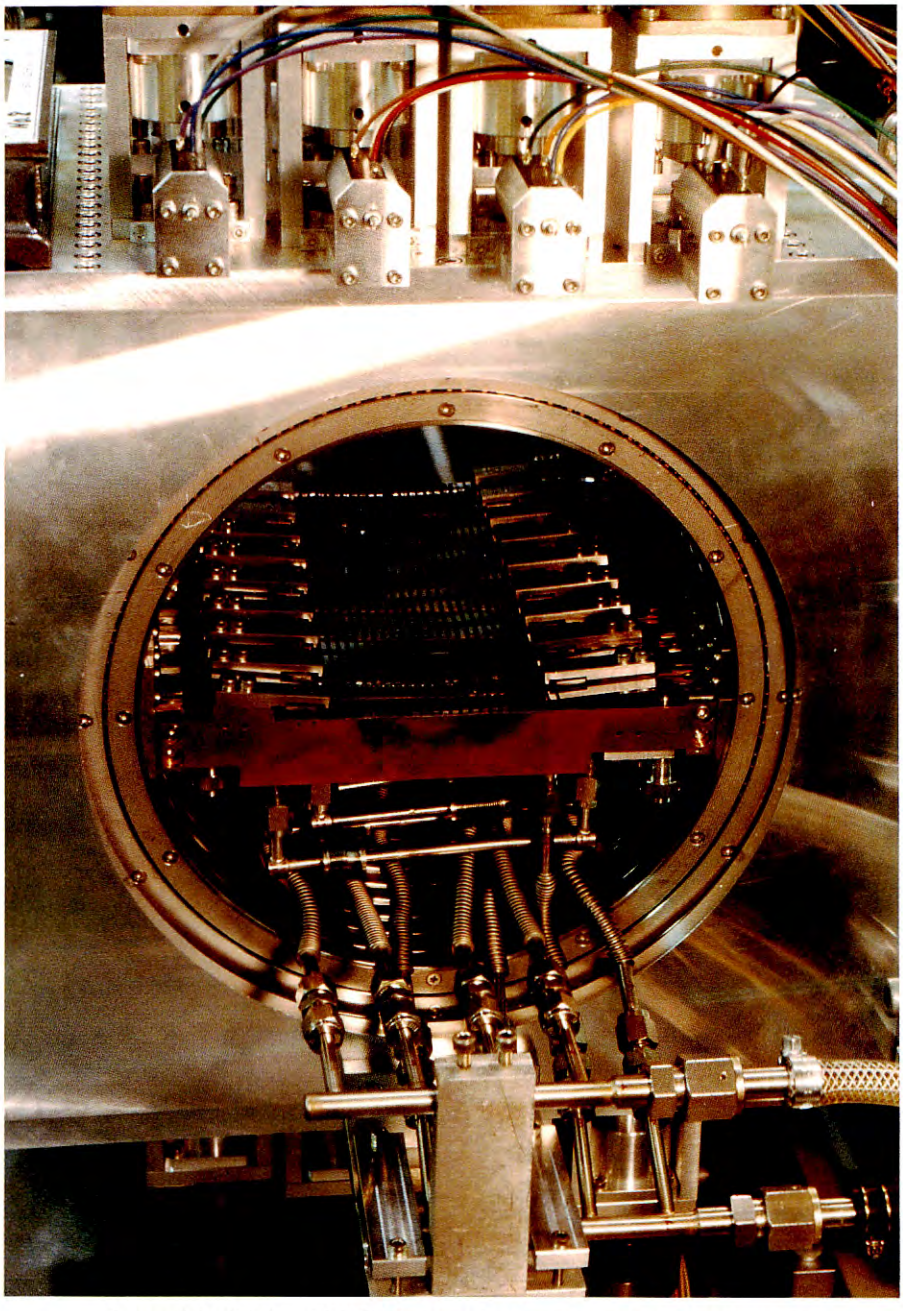

A quasi-doubly-bent (Q-D-B) crystal monochromator composed of 20 pieces of singly-bent crystals on AR-NE1-A1 beamline.

INSTRUMENTATION DIVISION

A. INTRODUCTION

To meet the increasing needs for utilizing synchrotron radiation in various kinds of scientific fields and industrial applications, a great deal of efforts have been made to construct new beamlines and to make improvements of existing beamlines and instrumentations.

In 1989 emphasis is placed on the construction of beamlines which are connected to insertion devices and accept radiation having higher brilliance or particular polarization. In addition to these, beamlines are being under construction which have an optical system of collecting widely divergent radiation from the bending magnet and thus providing high photon flux at the sample position. All of these are called "purpose-oriented beamlines", at which innovative experiments using synchrotron radiation will be made.

In Tables 1-4, summary is given of the detailed parameters of the beamlines. A list of the apparatuses for synchrotron radiation experiments is also given in Table 1. The last two figures show the latest overviews of the Experimental Hall of AR and the 2.5 GeV PF Ring.

H. Iwasaki

B. BEAMLINES AND INSTRUMENTATIONS OF 2.5 GEV PF RING

BL-3, A Purpose-oriented Beamline

BL-3A, X-ray Diffraction and Scattering Beamline

A double-crystal monochromator and two mirror chambers were installed for monochromatizing, collimating and focusing the SR X-ray beam. An outlook of the optical system at BL-3A is shown in Fig. 1. The first crystal of the monochromator is flat Si(111) and the second Si(111) crystal is of a sagittally focusing type with the triangular bending mechanism. The first flat mirror is used for adjusting the vertical angular divergence in the parabolic curvature. The second mirror is used for refocusing the monochromated beam at 28 m from the source and adjusting down the beam at the sample position. Each of the first and second mirror systems consists of three Pt coated SiO_2 flat mirrors: 700 × 140 × 20 mm at the center and two of 400 × 140 × 20 mm. The

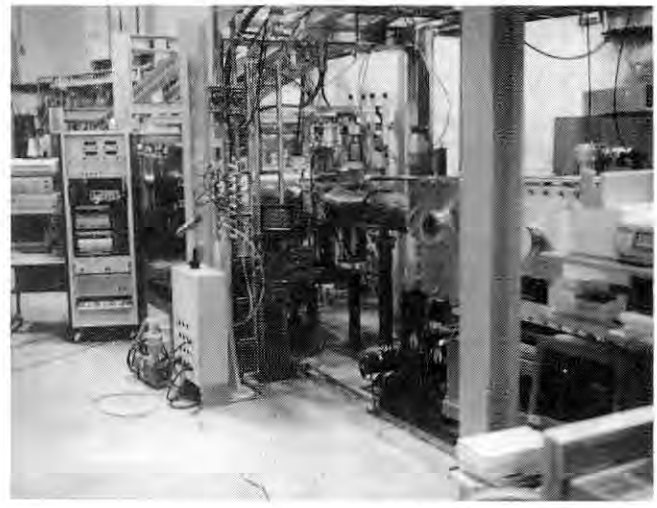

Fig. 1 A view of BL-3A

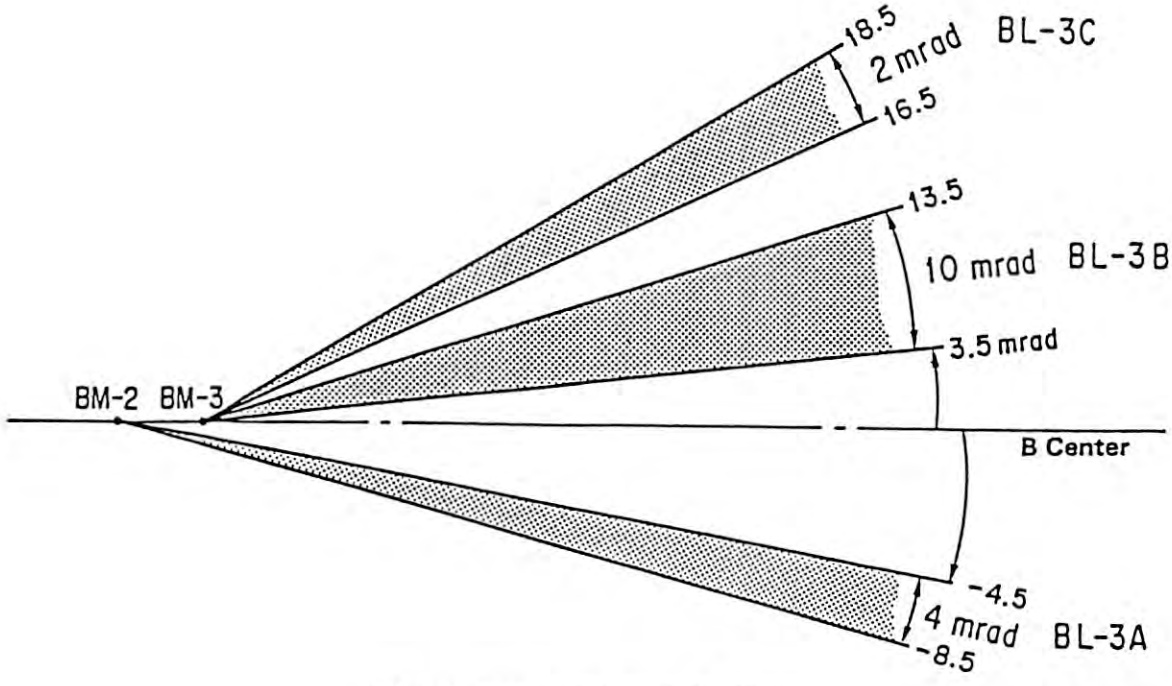

Fig. 2 Beam acceptance at BL-3

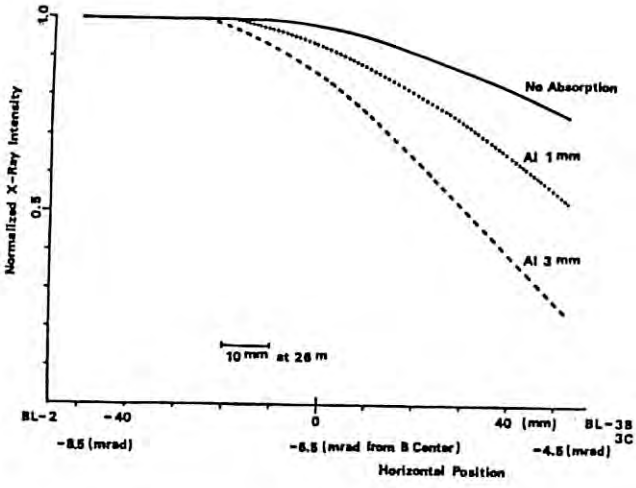

Fig. 3 Horizontal variation of X-ray intensities measured at BL-3A

critical energy of the incident beam can be varied from 5 to 25 KeV by the change of the glancing angle of the mirrors and automatical adjustment of beamline components. BL-3A has the horizontal acceptance of 4 mrad (Fig. 2).

We succeeded to lead both white and monochromated X-rays to the experimental hutch on December 10th, 1989. Figure 3 shows the horizontal intensity variation of the incident beam generalized by the bending magnet BM-2. The fringe effect at the end of the bending magnet was measured using the X-ray slit and ionization chamber. The reduction of the intensity was observed within the region between -4.5 and -7 mrad from the center between BM-2 and BM-3 (B Center). The normalized intensity is weaker apart from the center of the bending magnet BM-2 (toward the right side in the figure). Also, the intensity of higher energy X-rays is weaker than that of total SR spectra at the end of BM-2.

A newly designed triple-axis diffractometer was installed in the BL-3A by a joint group of Nippon Steel Corporation and Photon Factory. The diffractometer shown in Fig. 4 consists of three kinds of goniometer system: (1) θ_c-$2\theta_c$ axes on the monochro-collimator system, (2) four-circle goniometer as sample handling, and (3) θ_a-$2\theta_a$ axes for the analyzer crystal with a scintillation detector. The crystal orientation can be adjusted quickly and simply through the well-aligned goniometers, half-slits, and computer system. The diffractometer is guaranteed for the high precision movement of

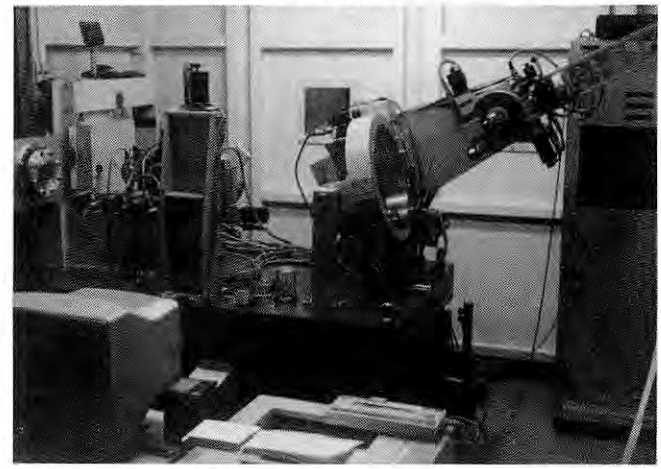

Fig. 4 Four-circle diffractometer with the crystal-collimator and crystal-analyzer system

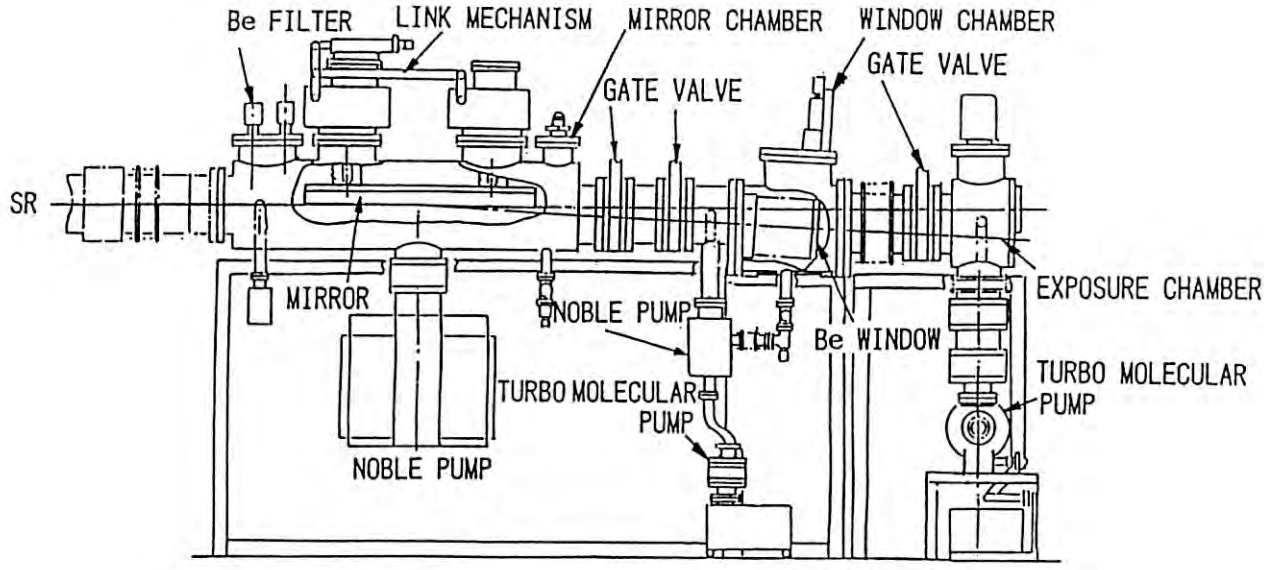

Fig. 5 Schematic layout of the instrument

each axis: for example, the minimum step the ω arc is 0.1 second per pulse with the accuracy of 5 seconds.

S. Sasaki

BL-8, Hitachi Beamline

BL-8C, New Experimental Apparatus

Synchrotron radiation (SR) is the most suitable light source for X-ray lithography in regard to resolution and throughput. The small divergence in the vertical direction, however, requires methods to obtain a reasonable exposure field, say 30 × 30 mm. For this purpose, optical systems using plane scanning mirrors have been investigated so far. However, the divergence in the beam at the mask and the change in the beam direction cause penumbra[1] and run-out error (distortion), which cannot be neglected for 0.2 μm feature size. To solve three problems, we have developed a new optical system using an aspherical scanning mirror.

The instrument consists of a mirror chamber, a window chamber and an exposure chamber as shown in Fig. 5. A water-cooled Be filter absorbs low energy component of SR. The divergent beam strikes a paraboloidal mirror at 25 mrad grazing angle and is collimated. This mirror was fabricated using a numerically controlled flycutting machine.[2] To keep an angle of incidence constant, the mirror is rotated about an axis outside the mirror by a link mechanism. Thus, the direction of the reflected beam and the reflectivity is always constant.

The beam then passes through a vacuum-tight Be window. This window must withstand atmospheric pressure. Further, a thin window is desirable to obtain high transmittance. To meet these requirements, the window of which height is the same as that of the beam moves perpendicular to the beam direction.

The instrument was installed at BL-8C in August 1989 and the initial tests were carried out. The case pressure in the mirror chamber is 1×10^{-6} Pa. A field of 30 × 30 mm is exposed with good uniformity of illumination at a constant scanning speed. We plan to evaluate the resolution in the near future.

References

1. J. Warlaumont: Nucl. Instrum. Methods, A246(1988)687.
2. S. Moriyama, et al.: Opt. Eng. 27(1988)1008.

M. Itou and S. Moriyama

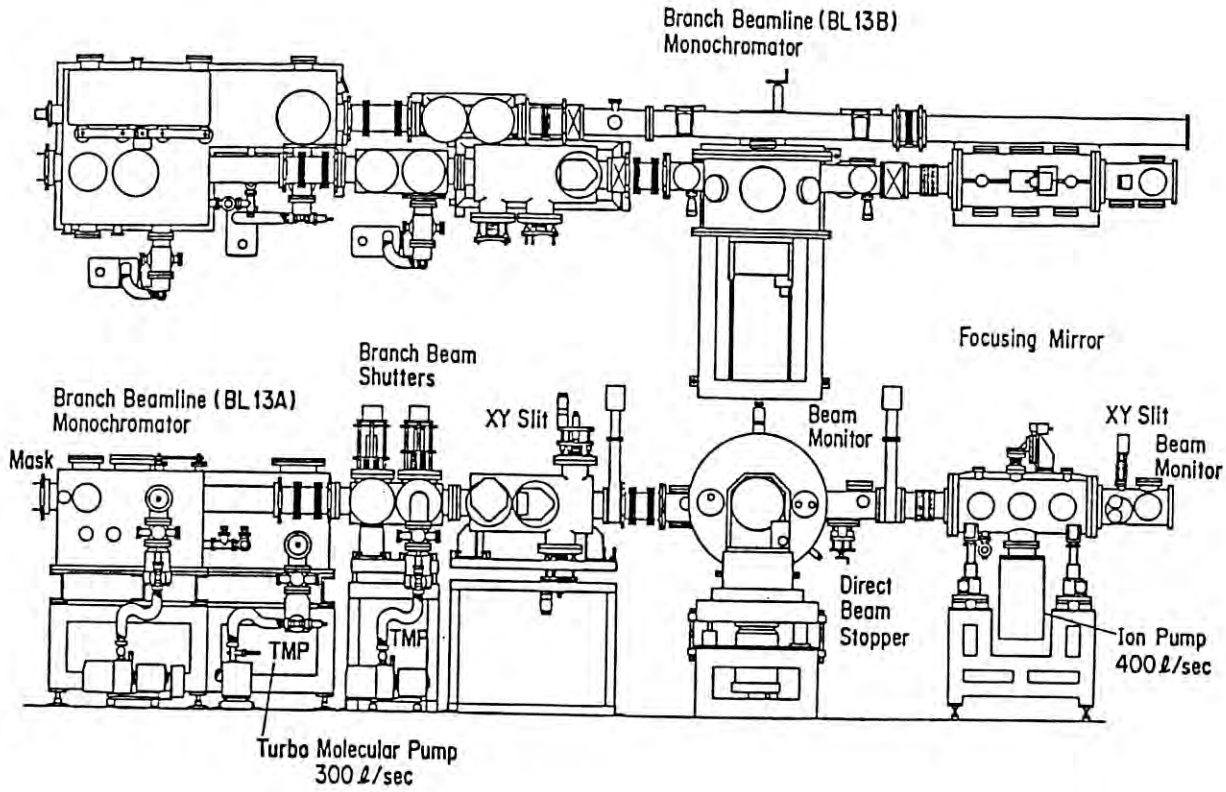

Fig. 6 Vertical and horizontal views of the optical components of BL-13

BL-13, A MPW/U Bexmline of National Institutes of STA and MITI

BL-13A & B, A Hard X-ray Beamline

BL-13 was designed and built in FY 1986-87 as a multipole wiggler(MPW)/undulator(U) beamline in the hard (4 - 25 KeV) or the soft (50 - 1000 eV) X-ray region. The 29-pole magnet and its front end were constructed and inserted between bending magnets B12 and B13 in FY 1987. BL-13 consists of two branch beamlines BL-13A and BL-13B which are both hard X-ray beamlines separated with an upstream front-end UHV section by Be windows. Fig. 6 shows the outlook of the major optical components of the two branch beamlines. The branch beamline BL-13B accepts the central part (4 mrad) of the MPW radiation which is sagittally focused at either one of the two tandem arranged experimental hutches, while BL-13A simultaneously accepts a fraction (1 mrad) of the side beam by a grazing-incidence reflection using an asymmetrically-cut crystal.

The first beam from the BL-13MPW introduced into the branch beamline BL-13B on June 26, 1989 with the ring current of 150 mA and the wiggler magnet field of 1.25 T. On Oct. 16, the BL-13-MPW was operated with the full power, i.e., 300 mA, 1.5 T, for which the total power is calculated to be 6.73 kW. The graphite absorbers consisting of five 0.13 mm thick foils were inserted in front of water-cooled Be windows (200 μm × 2). Upon exposure to the MPW radiation, the temperature of graphite absorber increased to 110 °C, while the initial vacuum near the Be windows dropped from 4 × 10^{-9} Torr to 5 × 10^{-7} Torr, which improved to 1 × 10^{-7} Torr in a few hours.

A direct water cooling scheme proposed by Oversluizen et al.[1] was used to cool the first crystal, Si(111). the surface temperature and its distribution were measured by an infrared TV camera. The cooling fin width and the channel width were 1 mm and 0.8 mm, respectively. With the regulated water temperature of 20 °C and the water flow of 16 l/sec, the maximum surface temperature was 26 °C for the ring current of 300 mA and the wiggler magnetic field of 1 T. The crystal deformations are presently studied by double-crystal rocking curves.

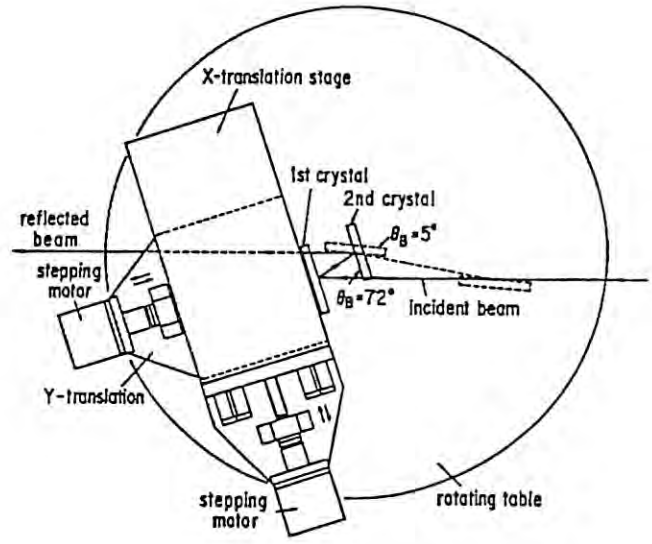

Fig. 7 Schematic of a variable beam-height double-crystal monochromator

A schematic of a sagittal-focusing double-crystal monochromator is shown in Fig. 7. In this monochromator design, a computer-controlled XY stage replaced a mechanical link of the original design by Matsushita et al.[2] The X,Y positions of the first crystal is controlled in order to obtain the constant output beam height according to simple equations, i.e., $X = H/2\cos\theta_B$, $Y = H/2\sin\theta_B$, where H is the difference between the incident and output beam positions θ_B is the Bragg angle. Moreover, a negative feedback of the deviation of the beam position can remove the output beam position fluctuation.

References

1. T. Oversluizen, T. Matsushita, T. Ishikawa, P. M. Stefan, S. Sharma and A. Mikuni: Rev. Sci. Instrum., 60(1989)1486.
2. T. Matsushita, T. Ishikawa and H. Oyanagi: Nucl. Instrum. Methods A246(1986)377.

H. Oyanagi

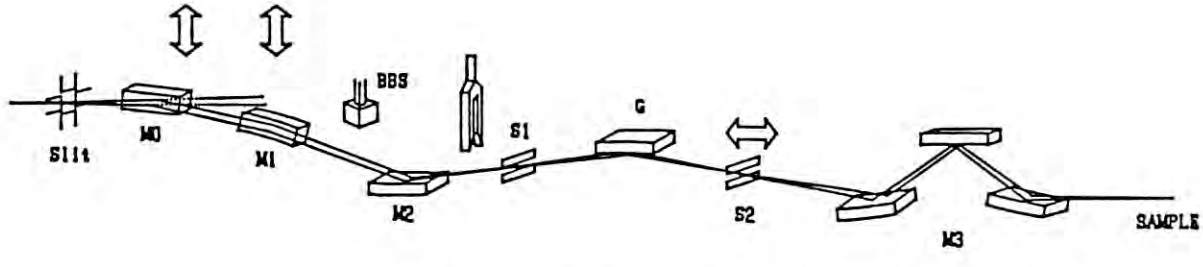

Fig. 8 The optical arrangement of BL-13C

BL-13C, A Soft X-ray Beamline

BL-13C is intended to utilize soft X-rays of 200 - 1000 eV with high resolution and high flux using a highly brilliant source through an undulator. The optics was designed following the "Dragon" type monochromator reported by Chen et al.[1] and optimizing for BL-13 as SiC schematically shown in Fig. 8. A branching plane SiC mirror (M0), a horizontal focusing mirror (M1), a branch beam shutter (BBS), a vertical focusing mirror (M2), an entrance slit (S1), a SiC grating (G), an exit slit (S2), and refocusing mirrors (M3) are located on the branch beamline in this order. All optical elements are cylindrical or planar to separate horizontal focusing and vertical focusing.

The first mirror (M0) deflects horizontally from the main beamline (BL-13A and B) at 3° and the second mirror (M1) deflects further at 4°. Both mirrors are cooled by water. M1, which is a cylindrical mirror with 441 mrad, horizontally focuses soft X-rays on a sample. The third mirror (M2) vertically deflects up at 3.76° and focuses X-ray on the entrance slit (S1). The grating (G) is cylindrical with 50 mrad and mechanically ruled at the groove density of 750

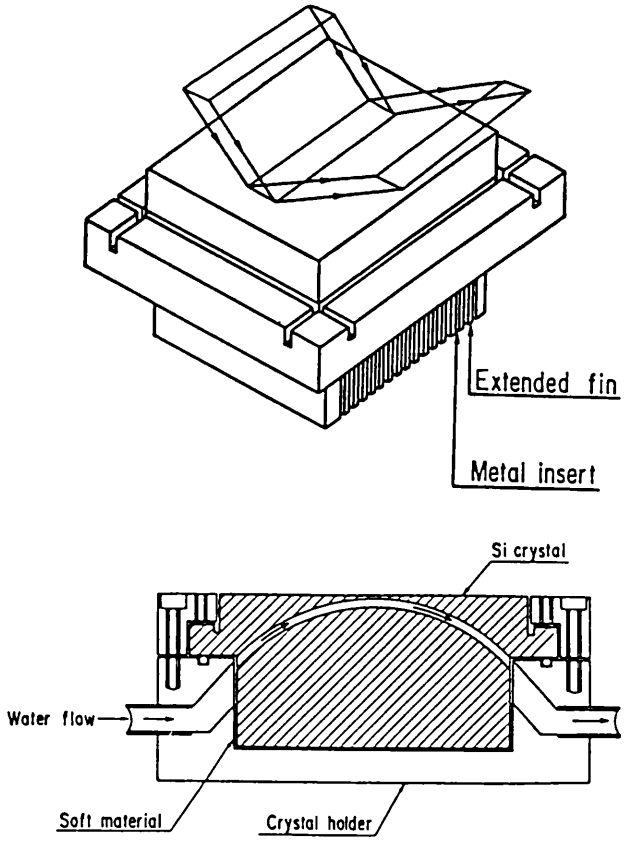

Fig. 9 Directly water-cooled crystal with extended stiffening ribs

l/mm. The deviation angle is constant at 173.2°. The exit slit (S2) is movable to follow the focus with scanning wavelengths. Refocusing mirrors (M3) are intended to remove higher order components.

Three of optical components, M0, M1 and G are produced by the end of FY 1989. Others will be installed in FY 1990.

Reference

1. C. T. Chen and F. Sette, Rev. Sci. Instrum., 60(1989)1616.

N. Matsubayashi

BL-16, A Multipole Wiggler/Undulator (MPW/U) Beamline

We modified the design of the directly water-cooled monochromator crystal on the X-ray branch of this beamline. The crystal of the previous design has a shape of a 21 mm thick flat disk having semi-circular water channels below the irradiated surface. In the new design, fins between these water channels are extended outwards to make the total thickness of

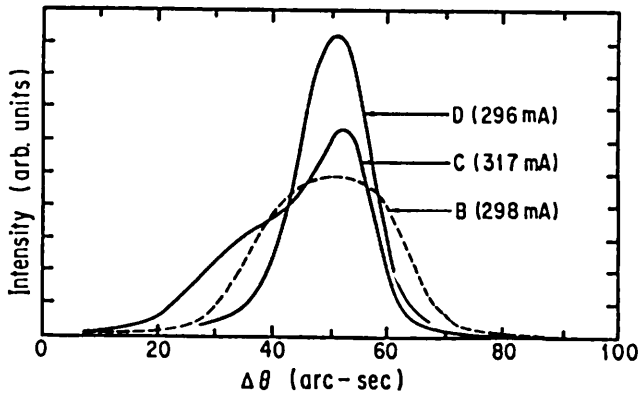

Fig. 10 Rocking curve obtained with the new (shown in Fig. 9) crystal is compared with that for the crystal without extended stiffening ribs

the crystal 40 mm, as illustrated in the Fig. 9. These fins work as stiffening ribs to avoid bending of the crystal which is caused by the thermal expansion of the irradiated surface. Fig. 10 gives rocking curves obtained with the previous crystal (B) and the new crystal (D). The peak reflectivity is almost twice higher, and the curve width is narrower with the new crystal. Although the radius of curvature is about 200 m for the new crystal when the 53 pole wiggler is operated at 2.5 GeV, 300 mA and 1.5 T, the output intensity on this beamline is 20 - 30 times higher than bending magnet X-ray beamlines. As the second crystal, a triangular crystal with stiffening ribs is used to horizontally focus the X-ray beam. The intensity of the X-ray beam at the sample positron is increased by a factor of 10 - 20 with this sagittal focusing crystal. Several experiments have already been done on this beamline.

In collaboration with Dr. T. Harada of Hitachi, Ltd., a significant progress has been

made on the development of SiC gratings used on the undulator branch of this beamline. The grating grooves were mechanically ruled on the surface of gold films deposited on the CVD-SiC substrate. The gold master gratings survived a long term irradiation of the intense undulator radiation.

T. Matsushita

BL-17, Fujitsu Beamline

BL-17B, A VUV Beamline

We modified the design of the directly water-cooled monochromator crystal on the X-ray branch of this beamline. The crystal of the previous design has a shape of a 21 mm thick flat disk having semi-circular water channels below the irradiated surface. In the new design, fins between these water channels are extended outwards to make the total thickness of the crystal 40 mm, as illustrated in the Fig. 9. These fins work as stiffening ribs to avoid

A new branch line, BL-17B, has been constructed for the study of VUV-induced photochemical processing by Fujitsu Laboratories in collaboration with the Photon Factory at National Laboratory for High Energy Physics. (Fig. 11)

For photochemical processing, it is necessary to use an intense VUV light and gases in the reaction chamber without any window material. BL-17B was designed to perform this function.

SR beam from B-17 bending magnet is reflected upward by Pt coated SiC toroidal mirror that is placed at 12 m point from the source. The mirror accepts 8 mrad horizontal and 1 mrad vertical divergence of SR. The incident angle of the toroidal mirror is 85 degrees, so a white beam with a photon energy up to 600 eV is utilized.

For allowing the use of reaction gases at the reaction chamber, the vacuum protection system against the upstream beamline and the electron storage ring was carefully designed. A differential pumping system with turbo-molecular pumps and rotary-pumps allows a pressure of up to 10 Torr in the reaction chamber while the pressure in the beamline is maintained on the order of 10^{-9} Torr. A fast-closing valve with a 12 ms closing time is installed between the toroidal mirror chamber and the differential pumping system to prevent accidental vacuum breakdown. The vacuum quality in the toroidal mirror chamber is also monitored continuously by a quadruple mass analyzer. The upstream valve shuts when the reaction gas signal is detected.

The toxic reaction gas is eliminated to less than ppm level by a removal system. The concentrations of reaction gas at the exhaust gas line and several environmental points are always monitored by sensors. The gas supply stops immediately stopped when gas leakage is detected.

Y. Nara

BL-18, ISSP Beamline

The beamline 18 is designed to accept dipole radiation emitted from BL-18 and divided into three branch beamlines; BL-18A, BL-18B and BL-18C. The construction of BL-18A was completed in 1989 under collaboration between the Synchrotron Radiation Laboratory of the Institute for Solid State Physics, the University of Tokyo, and the Photon Factory.

BL-18A

This beamline is designed for experiments of photoelectron spectroscopic studies of surfaces and interfaces in VUV region. Synchrotron Radiation with horizontal acceptance of 1.5 mrad is reflected by a SiC cylindrical mirror to a grazing incidence monochromator with two constant deviation angles (152 ° and 167.5 °) and focused onto a spot with diameter less

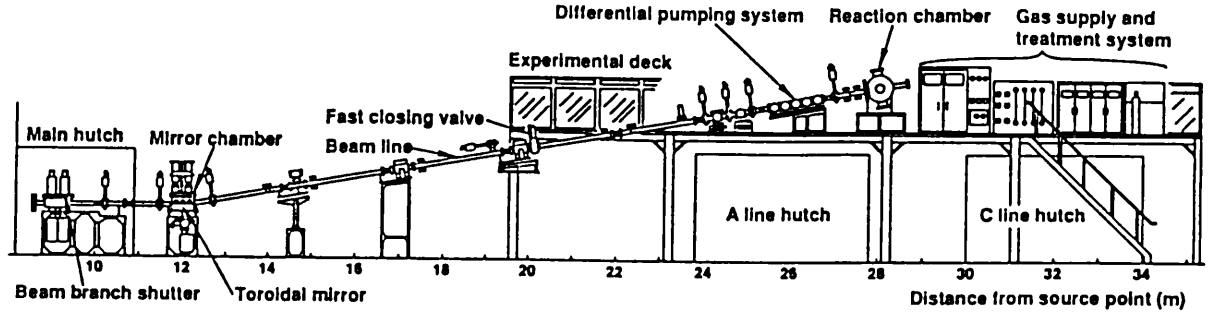

Fig. 11 Layout of BL-17B

than 0.5 mm. This monochromator (CDM-18A) covers the photon energy range from 10 to 150 eV by changing four spherical gratings. From the photoelectric yield spectra of gold we have estimated the photon flux to be 3 ~ 5 × 10^{10} photons/sec in whole photon energy region (Fig. 12), with resolving power better than 1000. The angle resolved photoelectron spectroscopy by using VG-ADES500 spectrometer are now proceeding.

A. Kakizaki

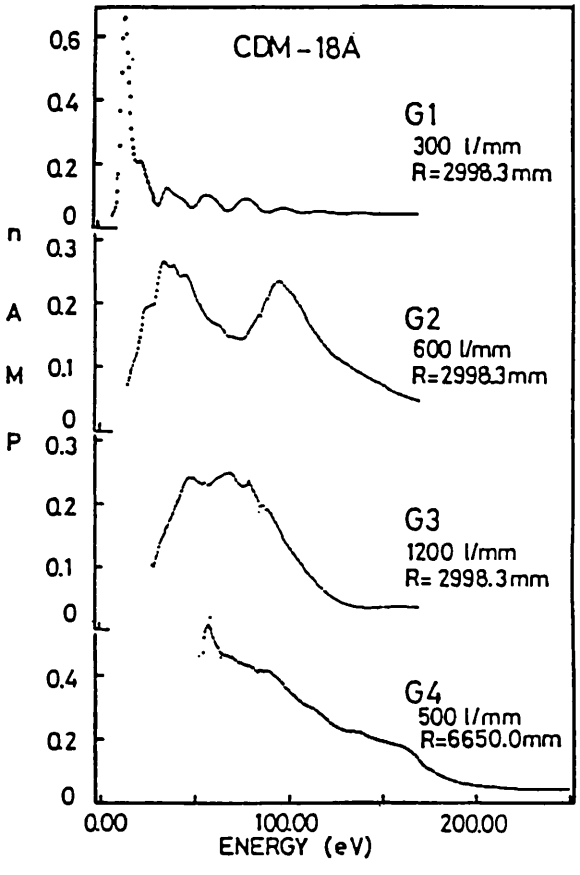

Fig. 12 Photoelectron yield spectra of a gold

BL-19, ISSP Beamline (Multi-undulator, Revolver)

BL-19A

The design principle and the outline of this beamline has been already given in the preceding volume. We have completed the characterization of the multi-undulator (Revolver#19) and the monochromator (CDM-19A) during 1989.

Among four pairs of permanent magnets, we have used magnet D, which is suited to the CDM-19A. Figure 13 shows the spectral profile of undulator radiation with 100 mm gap (K = 2.37). The photon energy at the intensity maximum and

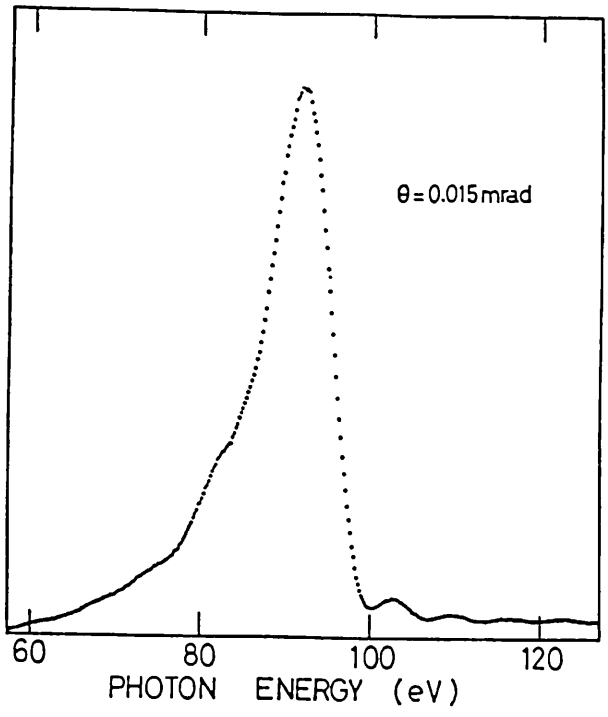

Fig. 13 Photoelectric yield spectra of a gold near the first harmonic peak with K = 237

the profile agree quite well with calculated ones.

The photoelectric yield spectra of gold with K = 4.64 and 8.38 are shown in Figs. 14 and 15, respectively. The acceptance of the radiation was chosen to be the natural spread of the undulator radiation by restricting the incident beam by water-cooled diaphragms. The photon energy covered by CDM-19A is from 20 eV to 250 eV.

A. Kakizaki

BL-20, A High Flux 3M-NIM Beamline

A high-flux VUV spectroscopic beamline is now in course of construction at BL-20. Since the beginning of the operation of the storage ring, two 1-m Seya-Namioka monochromators, installed in BL-11C and 12A, have been used for the spectroscopic studies in the gas and solid phases. However, the experiments carried out with these monochromators have always been limited by the lack of photon flux. In order to overcome this, we intend to construct a high-flux spectroscopic facility in the VUV region at BL-20. Synchrotron radiation of 28 mrad in the horizontal divergence is focused with a toroidal mirror onto the entrance slit of a 3-m normal incidence type monochromator which covers the photon energy region of 10 - 40 eV with a photon flux of 10^{10-12} photon/sec.A. The resolving power of the monochromator is estimated to be greater than 10^{4}. The first photon is expected to come out from the monochromator in April 1991.

K. Ito

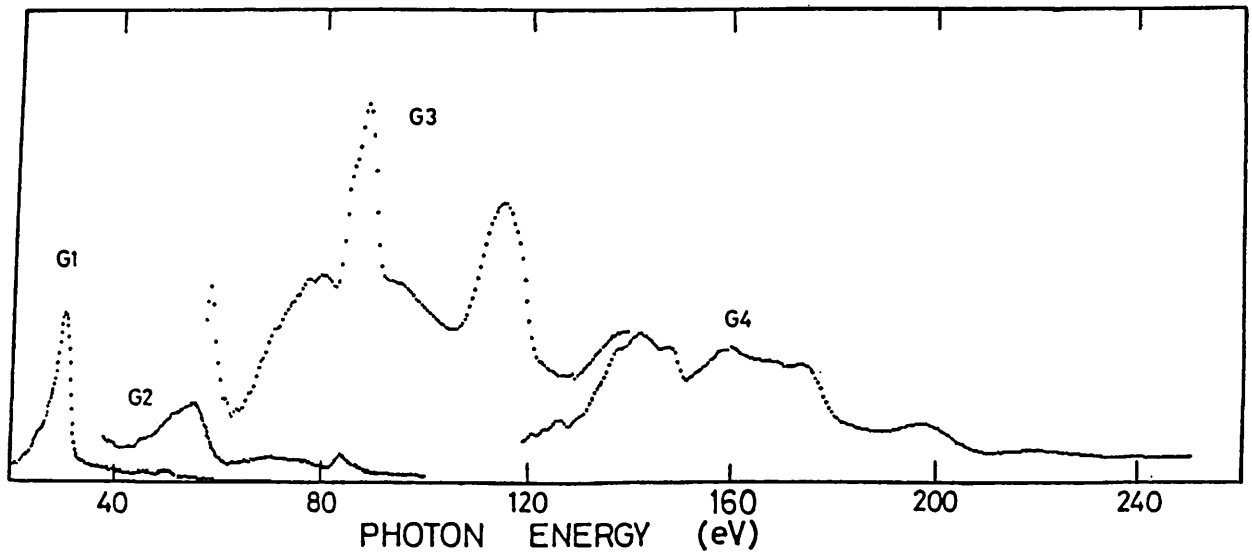

Fig. 14 Photoelectric yield spectra of a gold with gap = 67

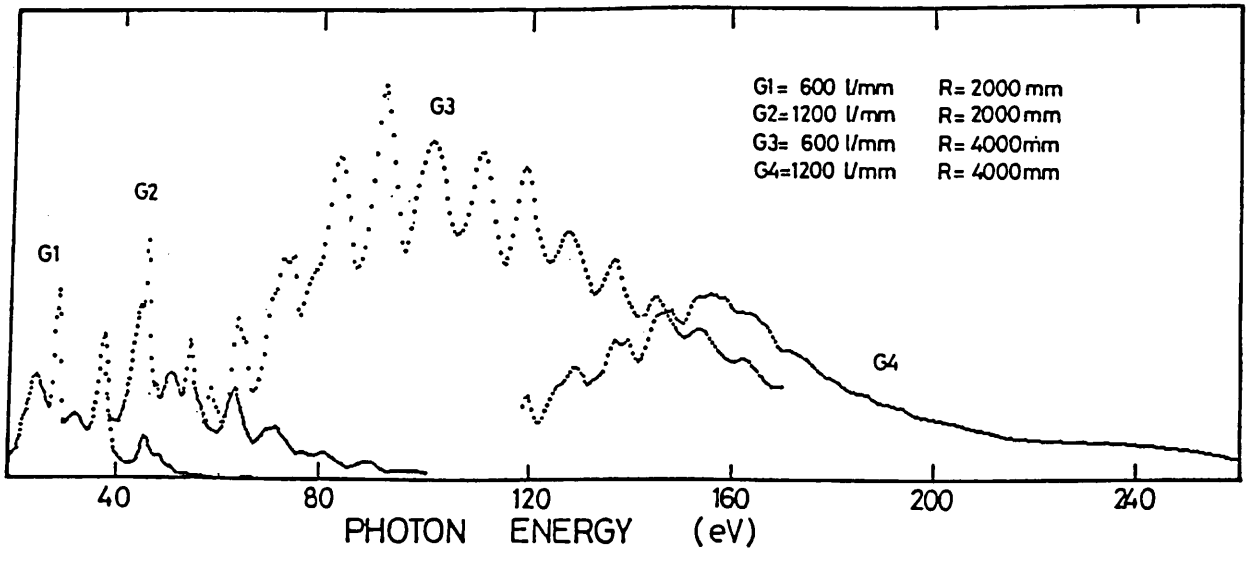

Fig. 15 Photoelectric yield spectra of a gold with gap = 37 mm

BL-27, A Beamline for Radioactive Materials

Since early stage of construction of the Photon Factory, there has been a plan to use radioisotopes as tracers, mainly for the study of irradiation effects of synchrotron radiation on biological samples. Experimental area including BL-27 and 28 and accompanying preparation rooms were constructed to enable the safe handling of radioisotopes. Recently, needs for the usage of radioisotopes have also grown up in material sciences. In order to fulfil all these requirements, BL-27 was designed where restricted kinds of radioisotopes can be used as samples.

According to the design, the beamline is divided into two branch beamlines, each of which covers soft X-ray or hard X-ray region and has two experimental stations in order to match various kinds of experimental requirements. BL-27A, a soft X-ray line accepting 5 mrad of the radiation, has a station for irradiation experiments of biological samples and a station for X-ray photoelectron spectroscopy. BL-27B, a hard X-ray line accepting 4 mrad, has an EXAFS station and a station for diffuse X-ray scattering study. Both lines have focussing systems and the photoelectron spectroscopy station and the diffuse scattering station are located at their focus points.

To avoid the contamination of beamline and the storage ring, various precautions must be taken against vacuum accidents. Reliable system to prevent the radioisotope invasion of upstream beamline is now being developed in combination with a specially designed interlock system.

K. Kobayashi

BL-28, A Circular Polarization MPW/U Beamline

The first test operation to introduce undulator radiation into BL-28 was successfully performed with changing the vertical gap from 60 mm to 190 mm. The total power of the radiation impinging on the first focussing toroidal mirror was estimated to be 550 W when the stored current was 350 mA and the vertical gap was 60 mm which corresponds to K_y = 7.6. Though the base pressure of the mirror chamber was 1.1 × 10^{-10} Torr, it increased up to 1.6 × 10^{-7} Torr with the maximum heat load. This pressure rise is not only due to temperature rise of the mirror but also due to photo-induced diffusion of impurities towards the surfaces of materials accepting the radiation. This diffusion effect was found to be strongly material dependent: When the water-cooled Cu block attached to the upstream side of the mirror was exposed to the radiation, it took 60 hours to recover 1 × 10^{-8} Torr. However when a 1 mm thick Ta plate attached to a water-cooled slit block was exposed to the radiation, it took only 4 or 5 hours to recover the same pressure. The difference may be due to the difference between the diffusiveness of impurities such as carbon and other light elements in the two materials or due to the difference between the absorption coefficients for X-rays.

The focussed image was observed through a viewport at the end of the beamline when the stored current was 5 mA. The undulator radiation was clearly distinguished from the background bending radiation because the focussing property of the toroidal mirror was optimized to give a good focussed image of the undulator radiation. This was also confirmed by observing the image with a black stripe through a polarizing plate.

T. Miyahara

C. AR, Project of Utilization of SR from Accumulation Ring

At the same time of the construction phase of the Accumulation Ring for the Tristan project which has a function of boosting electrons and positrons for the Main Ring where the colliding experiments to search new particles are performed. The Photon Factory was kindly invited by the Tristan project to have an experimental hall for the future use of synchrotron radiation when it was initiated. According to this kind offer, already since 1986 we have initiated attempt at the use of SR (synchrotron radiation) of the AR from which high energy X-rays photons are available.

The AR has potentially had capabilities as an SR source since its construction. Its accelerating energy is 8 GeV at maximum and 6.5 GeV in a storage mode because of the limitation of a cooling power. Since the radius of the curvature of the electron orbit at bending magnets is 23.2 m, the critical photon energy of 20 KeV is very similar to that from a vertical superconducting wave shifter at PF. Owing to its high energy of acceleration, it has possibilities of installing a variety of insertion devices for the X-ray energy region such as multipole wigglers and undulators.

Among driving forces of coming into the AR region is the very rapid growth of the number of experiments which utilize the station of BL-14C for SR from the superconducting wave shifter at the Photon Factory ring. In order to meet this requirement and also to create the new fields of solid state physics, molecular physics and some other applications to other fields such as angiography, we immediately made a decision to construct beamlines such that can extract fully capabilities of SR at the AR.

In addition to BL-NE5 which was constructed in 1986, a testing beamline for high-pressure and high-temperature X-ray diffraction and angiography experiments, the beamline BL-NE1 for the use of circularly polarized SR, which was constructed under the approval of the financial support from the Mombusho (the Ministry of Education, Science and Culture), has been successfully in operation since its commissioning in 1988. Along the commissioning, a trial for the extraction of high brilliance and high energy X-ray photons, problems due to high heat load of 2-4 kW have been revealed and thus many efforts have been put into to solve these problems: Those are a local bump of the first piece of a crystal chunk, another type of bump due to water pressure, d-spacing difference due to the water jacket structure, not only the first piece but also the heating of a second piece and heating of a second piece of a monochromator due to forward Compton scattering and heating of goniometer parts due to irradiation from beamline components such as a mask located just before the crystal component. It was very nice that we had opportunities to exchange over knowledge and experiences at the Argonne Workshop on High Heat Load X-Ray Optics organized by Robert Smither last summer.

Magnetic Compton profiles with good statistics and a very high resolution of 0.1 a.u. are now available. This technique has been successfully applied to three axes of ion crystals, Ni crystals and other materials. Not only circularly polarized high energy X-ray photons are produced at this line but also photons below 1 KeV are produced. These will be good for photoelectron spectroscopy in SX region. Already commissioning has been started; a spectrum in this energy region has been obtained experimentally.

As the second beamline using another type of insertion device has been designed; this will be installed in summer of 1990. This insertion device will have a capability of producing undulator X-rays ranging between 5 and 25 KeV using 3rd and 5th higher harmonics which is produced by the following performances; λu (periodicity) = 4 cm; K(deflection parameter) = 1.47; number of periods = 90; Bmax (magnetic field strength) = 0.58 T. This will give us photons of 1.9 × 10^{15} in a normal brilliance unit at 50 mA of ring current and at 6.5 GeV with emittance of εx = 157 nm. rad and εy = 4.7

nm. rad. Commissioning will be initiated sometime in the coming autumn. Overcome of 750 watts will be a main goal for the present. A special consideration such as cooling with other coolant will be needed, especially for higher ring current such as 150 mA.

A test beamline BL-NE5 is now under improvement for being capable of simultaneous use of SR at the stations NE5-A1 and A2. Currently due to the limitation of the beam aperture either one can be operated at one time. A modified beamline will be also installed in this coming autumn. Further another beamline using SR from a bend source will be installed in the very near future. Studies to be done at this line will be any experiments which will utilize capabilities of the AR such as short pulses because it is at present operated with a single bunch corresponding to approximately 1.2 μsec for the circumference and even in the future 4 bunches at maximum if in the higher current mode. Further another beamline BL-NE9 as a bend source will soon be constructed, in another words, two beamlines for two kinds of ID's and another two for bend sources. Because of the size limitation of the experimental hall at the AR, its extension will be needed in case of the growing demand for the SR at the AR.

M. Ando

AR-NE1, A Circularly Polarized Hard X-rays and Soft X-rays from E-MPW

This beamline is for experiments using circularly polarized hard X-rays and soft X-rays from an ellipsoid-multipole wiggler (E-MPW) or a helical undulator, and the outline of this beamline was described in the preceding volume. This year, commissioning of optical elements of beamline and its fine adjustment were developed. At this report, we only describe new improvements.

AR-NE1-A1

The main improvements of this beamline in this year are following two points: One is rearrangement of the beamline to obtain wider energy range of the monochromatized X-rays; E = 40 ~ 70 KeV, and another is commissioning of a quasi-doubly-bent (Q-D-B) crystal monochromator.

1. Rearrangement of the beamline

The energy range of monochromated X-rays before rearrangement was from 50 to 70 KeV, which cannot meet the experiment of the magnetic Compton scattering for Lanthanoid magnetic metals. The experiment can be performed with the energy of incident X-rays just below the K-absorption edge of these materials which distributes between 40 and 70 KeV. The energy range required is now available by the replacement of a new branch shutter and wider beam ducts.

2. A Q-D-B crystal monochromator

A Q-D-B crystal monochromator which comprises an array of 20 pieces of singly-bent crystals is illustrated in Fig. 16 and also shown in the title page of the Instrumentation Division. There are two essential points for installation; the first is the way to adjust 20 pieces of singly-bent crystals and the second is a heat problem.

2-1. How to adjust 20 pieces of singly-bent crystals

Twenty pieces of a single bent crystal must be aligned to work as a doubly-bent crystal. A preliminary adjustment was carried out by an off-line system using an ordinary X-ray source and a position sensitive propositional counter (PSPC) as schematically shown in Fig. 17 The

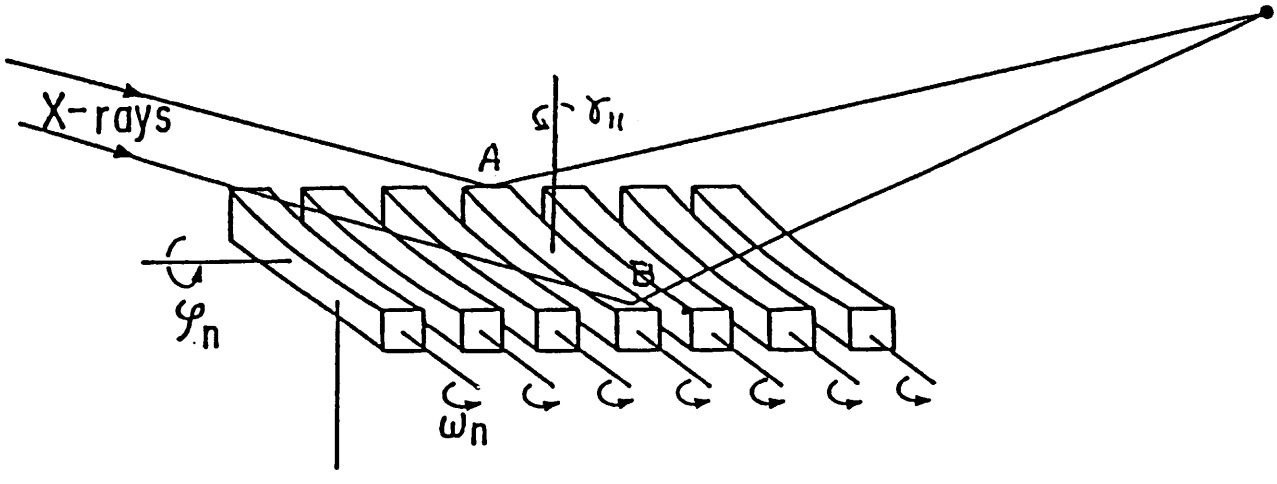

Fig. 16 Design concept of Q-D-B crystal monochromator

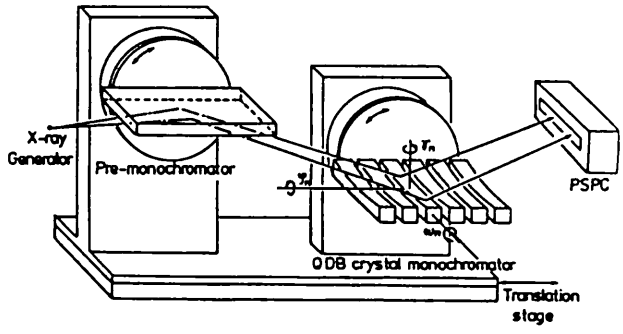

Fig. 17 Off-line adjustment system of Q-D-B crystal monochromator by using an ordinary X-ray generator

process of alignment is as follows. A pre-monochromator Si(111) and a Q-D-B crystal monochromator can be translated in the horizontal plane along an incident X-ray as a rigid body so that the whole singly-bent crystals can be adjusted by holding their orientations to the pre-monochromator. Diffraction from both ends of signly-bent crystal (say, right end and left) can be detected separately by using PSPC.

The energy resolution of design value was found not to be achieved by the adjustments of angles of ω_n and φ_n. An angle of γ_n for each bent crystal is recognized to be important for the adjustment as shown in Fig. 16. This importance can be easily understood qualitatively, as follows. If a crystal is flat, the rotation of γ_n will make no change of Bragg angle at the whole crystal, but if a crystal is singly-bent, the rotation of γ_n will produce the change of glancing angle of X-rays on the crystal surface at both the crystal ends (for example; positions marked A and B in Fig. 16) and makes a change of Bragg angle. The angles of γ_n and φ_n of each singly-bent crystal were adjusted with accuracy of 0.25 mrad. The final adjustment of ω_n was performed by using synchrotron radiation from E-MPW. Incident X-rays were limited by incident vertical slits in order to irradiate only a piece of singly-bent crystal.

The energy of monochromatized X-rays from the crystal was set by scanning ω_n by measuring an absorption edge of Tm_2O_3 (K-edge of Tm = 59.38 (KeV)). After such adjustment is performed for each crystal, step by step, the incident vertical slits are opened so that the incident X-rays irradiate the whole crystals.

The monochromator is located at 26150 mm point from a light source and the beam size limited by incident slits at the monochromator is 3.5 mm (height) × 33 mm (width). Figures 18 (a) and (b) show the image of monochromatized X-rays at 34000 mm from a light source (under focusing point) and at 37700 mm from a source (focusing point) respectively. At the focusing point, the beam size is about 3 mm (height) × 8 mm (width).

2-2. Heat problem

As described in the preceding volume, each bent crystal was mounted on a water-cooled holder and was thermally contacted with liquid Ga-In alloy, and furthermore, a thermal absorber of 7 mm thick Al plate is placed to avoid the heat load of X-rays lower than 40 KeV. At the beginning, the absorber was located in a monochromator vacuum chamber with the nearest distance of about 0.2 m from the monochromator. Under such a condition, the energy resolution changed rapidly at a full power irradiation (Acceleration energy; 6.5 GeV, Ring current; 30 mA and K-parameter for E-MPW; K_y = 15) as a manner shown in Fig. 19 (dotted line). Temperature measurements of monochromator revealed that the change for the worth of the energy resolution is estimated to be caused by temperature rising at each flame which adjusts the angle of ω_n, and that the temperature rising is caused by scattered X-rays and infrared radiation from the absorber and the crystal surface. The improvements were performed as follows. The first is that the absorber was shifted 0.5 m far from the monochromator. The second is that the scattered X-rays and radiation from the absorber and the crystal surface is shielded by a water-cooled copper plate and a 5 mm thick of lead plate. And the final is that each flame has thermal contact with cooling water by using knitted copper wires. After the above improvements, the energy resolution dose not change at all at a full power irradiation as shown in Fig. 19 (solid line).

AR-NE1-A2

A directly water-cooled double crystal monochromator is commissioned as the first stage of improvement of this beamline in this year . A special feature of this monochromator is to use an extraordinary large Si crystal for the first monochromator in order to cover the region of high energy of X-rays. The final length of the crystal size along an incident X-rays is 850 mm, but in the present stage of research and development work an Si with 300 mm long is installed in. Figure 20 shows the bottom surface of the crystal which has many channel to lead cooling water. The cooling system is similar to that of BL-16 in the PF Ring. The cooling power is almost sufficient as the rising temperature on the crystal surface which is measured by IR camera is about 10° at full power irradiation. But there are two problems: One is a bending of the crystal which is induced by the tight binding of the crystal edges to avoid a leakage of the cooling water. The radius of bend is measured 300 m by the off-line X-ray system mentioned above. An inserting thin stainless steel films (20 μm thick) between the crystal successfully makes the bending radius longer than 10 Km. Another problem is rising temperature of the second crystal and the holder higher than 40° at a full power irradiation.

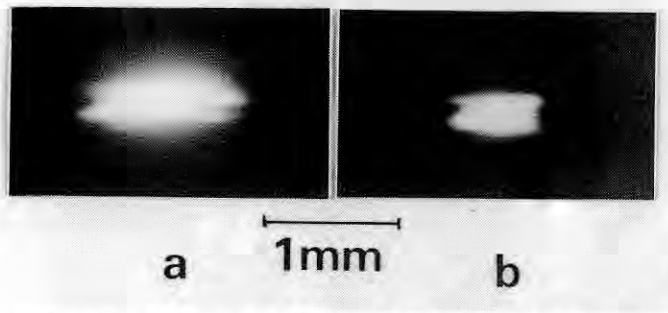

Fig. 18 Image of horizontally focused X-ray at (a) an under focusing point and at (b) a focusing point

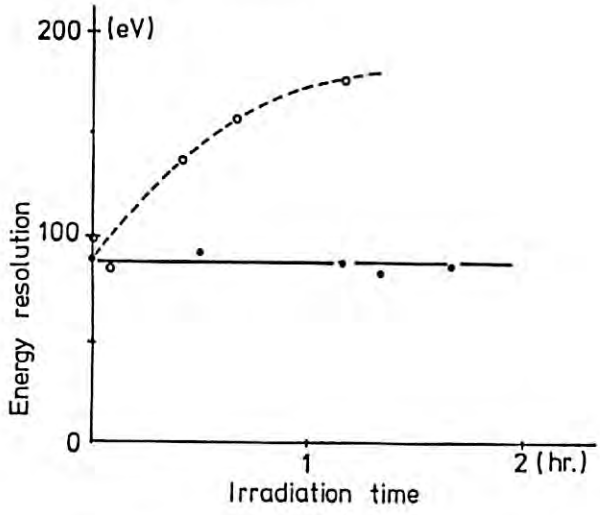

Fig. 19 Irradiation time dependence of the energy resolution of monochromatized X-rays at the beginning (dotted line) and after improvement (solid line)

The origin of this heating is considered to be the effect of Compton scattering of hard X-rays from the first Si crystal, which will be overcome soon.

H. Kawata

AR-NE3, An Undulator Beamline for the Photon Energy Ranging 5 ~ 25 KeV

As the second project of using SR (synchrotron radiation) from the AR (Accumulation Ring), production of the beamline NE-3 for uses of photons with energy ranging 5 ~ 25 KeV from an in-vacuum undulator is under way. It will be installed to commission in the fall of 1990. The source of BL NE-3 will be very much beneficial not only to Mossbauer nuclear resonant experiments but also to surface/interface structure analysis of

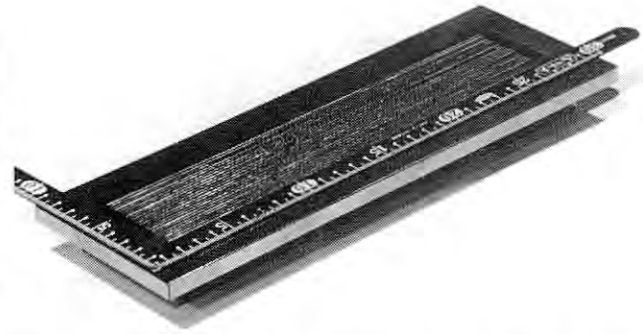

Fig. 20 Photograph of a first crystal which has channels at a bottom surface to lead cooling water directly

electronic materials, very small protein crystals and any other subjects which need high brilliance monochromatic X-rays.

The undulator installed in BL NE-3 has a magnetic periodicity of 4 cm × 90. Characteristic parameters of the AR and the undulator are shown in table. A top and side view of the beamline is shown in Fig. 21. For the destructive high power density of radiation from the insertion device, we calculated the thermal load on the beam mask and absorbers of the beamline, and evaluated water cooling apparatuses we designed.

Main sections of the beamline NE-3 are illustrated in Fig. 22. In the ring tunnel there are 1st SR position monitor, fixed mask, SR absorber unit and SR shutter unit. In the experiment hall there are carbon absorbers, beryllium windows, pre-absorbers of the DXM, pre-XY-slit of the DXM, double Xtal monochromator (DXM), fluorescence screen, γ-ray stopper, monochromatic X-ray shutter unit and 1st XY-slit. Two parts of the beamline are coupled by a transition tube long about 4 meter.

The DXM is designed as a Matsushita mechanical cam and direct water cooling model. It is suitable for incident angle 4 ° ~ 45 °.

An operation system diagram of the beamline NE-3 is shown in Fig. 23. User can operate the computer installed in the experiment station to change an angle of the DXM, angles of gonioes, slit width and a gap value of the undulator, to carry out him experiments. The design of an X-ray mirror is under way. The mirror system will condense photons from a beam size 10 mm × 1 mm to 1 mm × 1 mm or more less.

X. Zhang

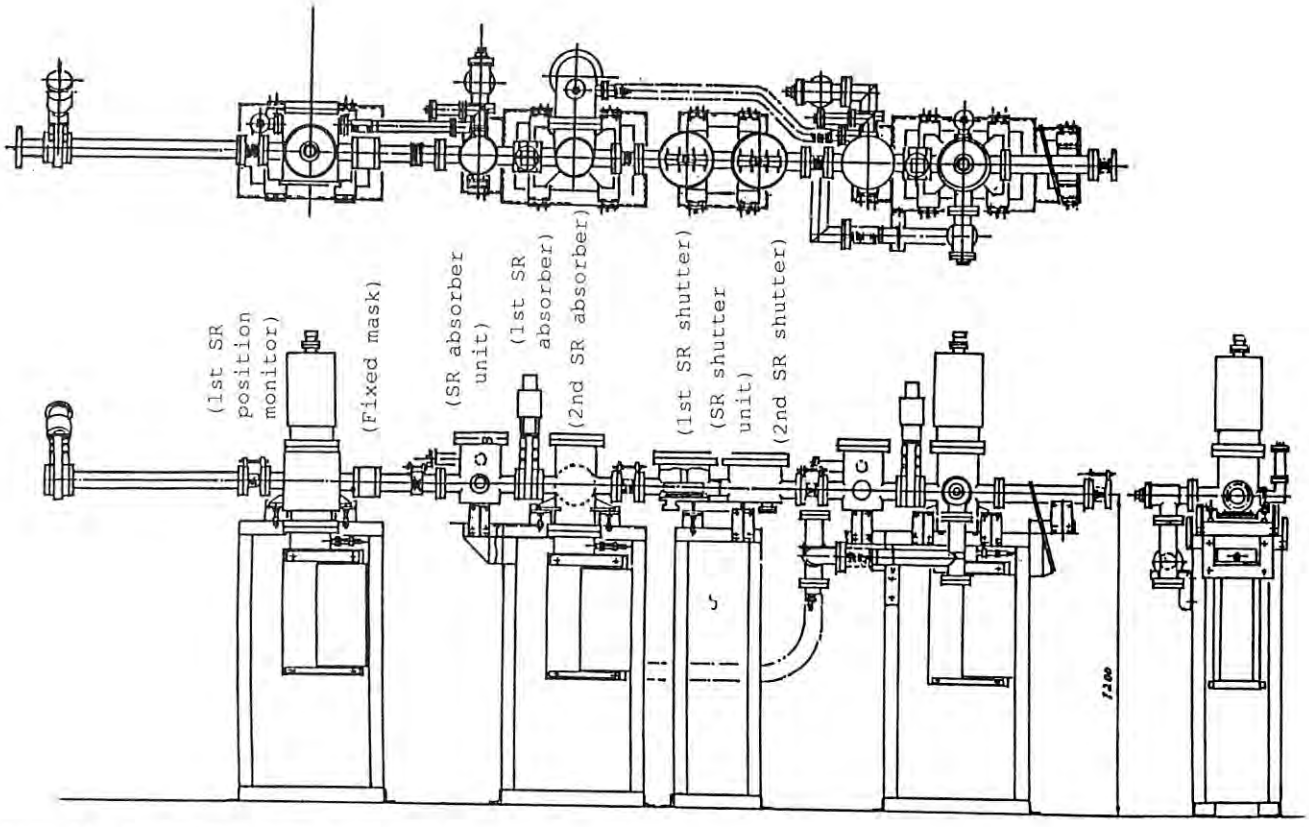

Fig. 21 A top and side view of the beamline NE3 in the accelerator tunnel. The beam path is 1200 mm high before the monochromator

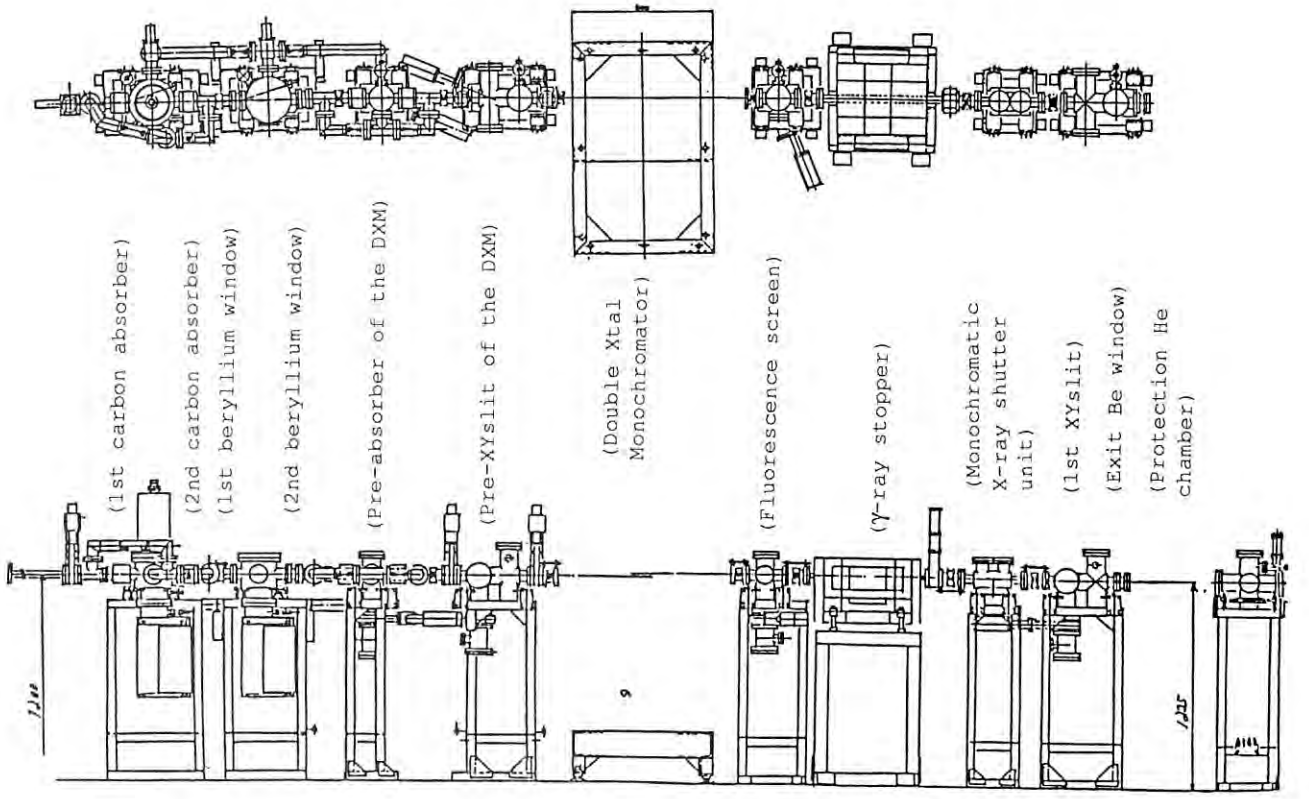

Fig. 22 A top and side view of the beamline NE3 in the AR experiment hall. The beam path became 1225 mm high through the monochromator

Table Parameters of the X-ray undulator and beamline NE-3 on the AR with 6.5 GeV and 50 mA under low emittance operation

emittance of the AR:	σ_x = 1.2 mm, σ_y = 0.20 mm σ_x' = 0.25 mrad, σ_y' = 0.030mm
beam size at monochromator:	10 mm × 1 mm
photon energy range:	5 ~ 25 KeV
total radiation power:	750 W
power density at 10 m from the source:	0.2 kW/mm^2
photon flux at 14.4 KeV:	1 × 10^{14} photon/sec/0.1%E

AR-NE5, A Beamline Utilizing SR from Bending Magnet

The beamline NE-5 was constructed as a test port at the first stage of the TRISTAN project for SR use of AR to develop synchrotron radiation science in much higher energy range.

The SR of this beamline is emitted from a bending magnet NE-4 which is the 4th bending magnet at the north-east section of AR and through a beam duct placed at the bending magnet NE-5. This beamline consists of a water-cooled aluminum window, a beam position monitor, a main beam shutter, a beam guide tube, and tandem time-shared experimental stations 5A1 and 5A2. On this beamline, high energy X-ray over 120 KeV is available in 6.5 GeV operation. It is higher than that from a vertical wiggler at BL-14 in the 2.5-GeV PF ring. Furthermore, this beamline accepts the largest horizontal divergence of 10 mrad of SR among all beamlines in the PF.

The front station 5A1, which locates at the distance of 19 m from the source point, has been used as a multi-purpose station. When this station was applied to coronary angiography, the beam has been monochromatized at 33 KeV and expanded to a beam size of 110 mm(H) and 70 mm(V) by the asymmetrical reflection from 311 planes of Si crystal. 5A2 station was constructed for the experiment such as structural study of materials subjected to high pressure and high temperatures by using MAX80 with white X-ray. In March, a double crystal monochromator was installed for high resolution X-ray experiments under the extreme condition.

Demands for high energy X-ray photons are increasing in many scientific fields as medical applications, high pressure study, CT experiments, X-ray induced chemical reactions and so on. This beamline is under reconstruction to be divided into three branch beamlines; i.e. NE-5A, 5B and 5C. The new branch beamlines 5A and 5C will be used instead of 5A1 and 5A2 stations. 5B will be applied for a feedback system to stabilize the beam position. They will accept horizontal divergence of 10 mrad for 5A branch beamline and 3 mrad for both 5B and 5C beamlines. Each beamline consists of two vacuum sections: One is a high vacuum (<10^{-9} Torr) front section, another a medium vacuum (<10^{-7} Torr) experimental section. The former section has a manual valve, a water-cooled copper absorber, the 1st pneumatic isolation valve, a water-cooled stationary beryllium absorber, a pair of beryllium windows and ion pumps. The latter section consists of a couple of beam shutters made of tantalum and the HEAVY METAL (Sumitomo metal company), the 2nd isolation valve, a beryllium window and turbo molecular pumps. This beamline has no channel section, therefore each branch beamline can be independently operated. The interlock system will be followed in that of the PF. It will be completed by November of 1990.

T. Kikegawa

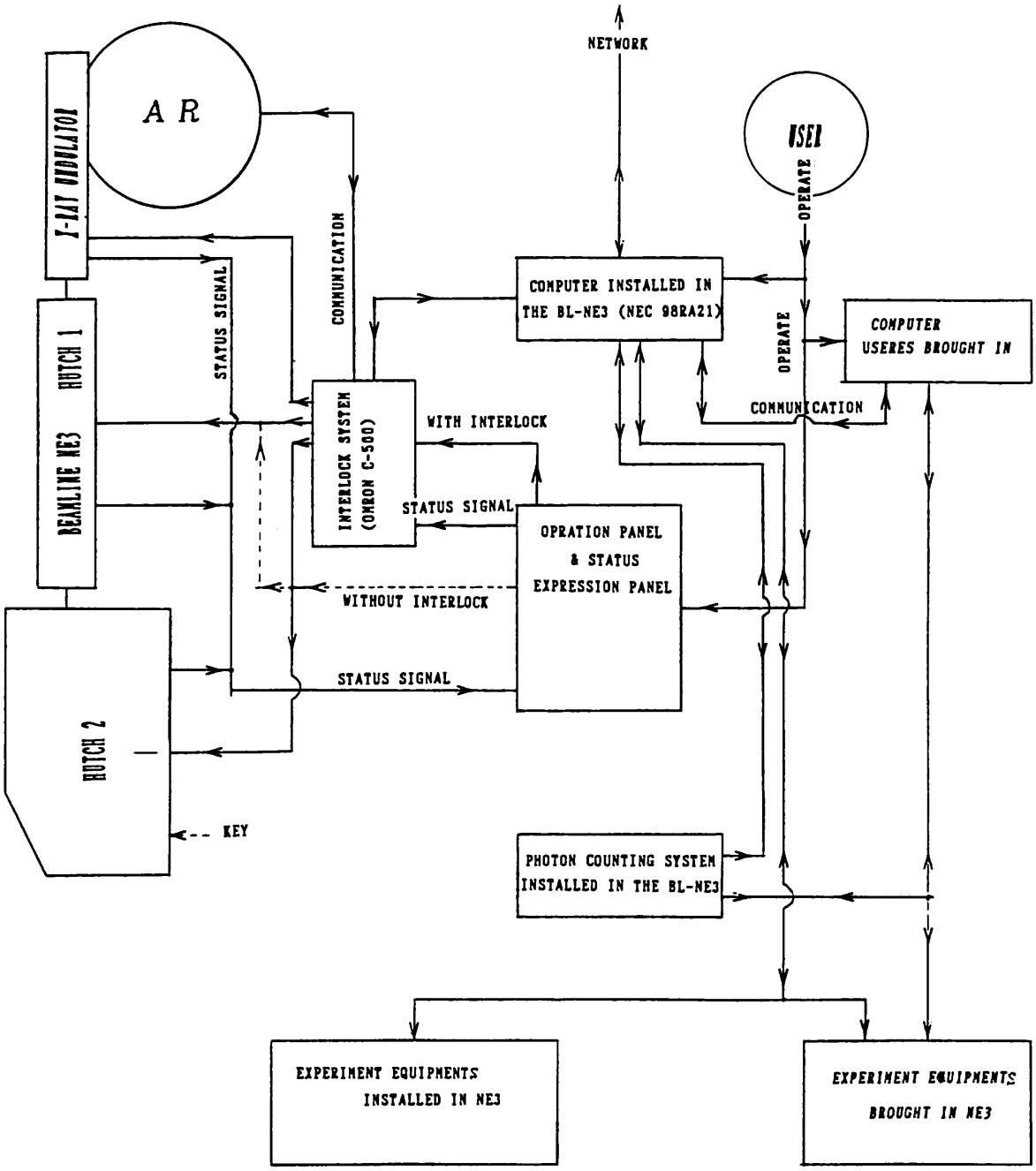

Fig. 23 A diagram of NE3 operation system. User can operate the computer installed in NE3 to change the angle of the monochromator, slit widths, angles of gonioes and gap value of the undulator. There is a without interlock mode in the system to operate the beamline directly, except 1st/2nd SR absorbers and 1st/2nd SR shutters. They are moved only in the with interlock mode.

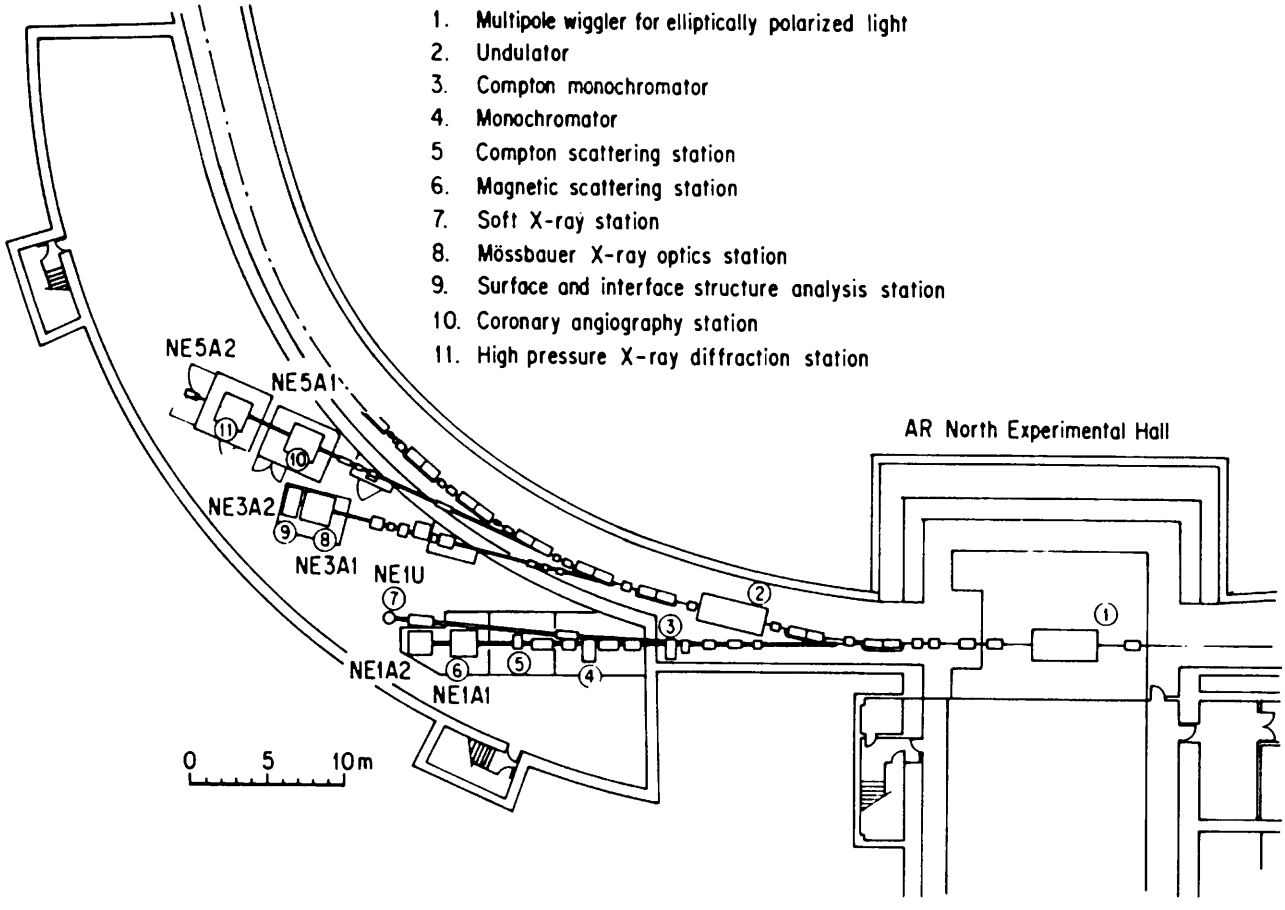

Fig. 24 Overview of the Experimental Hall of AR

Plan View of the Photon Factory

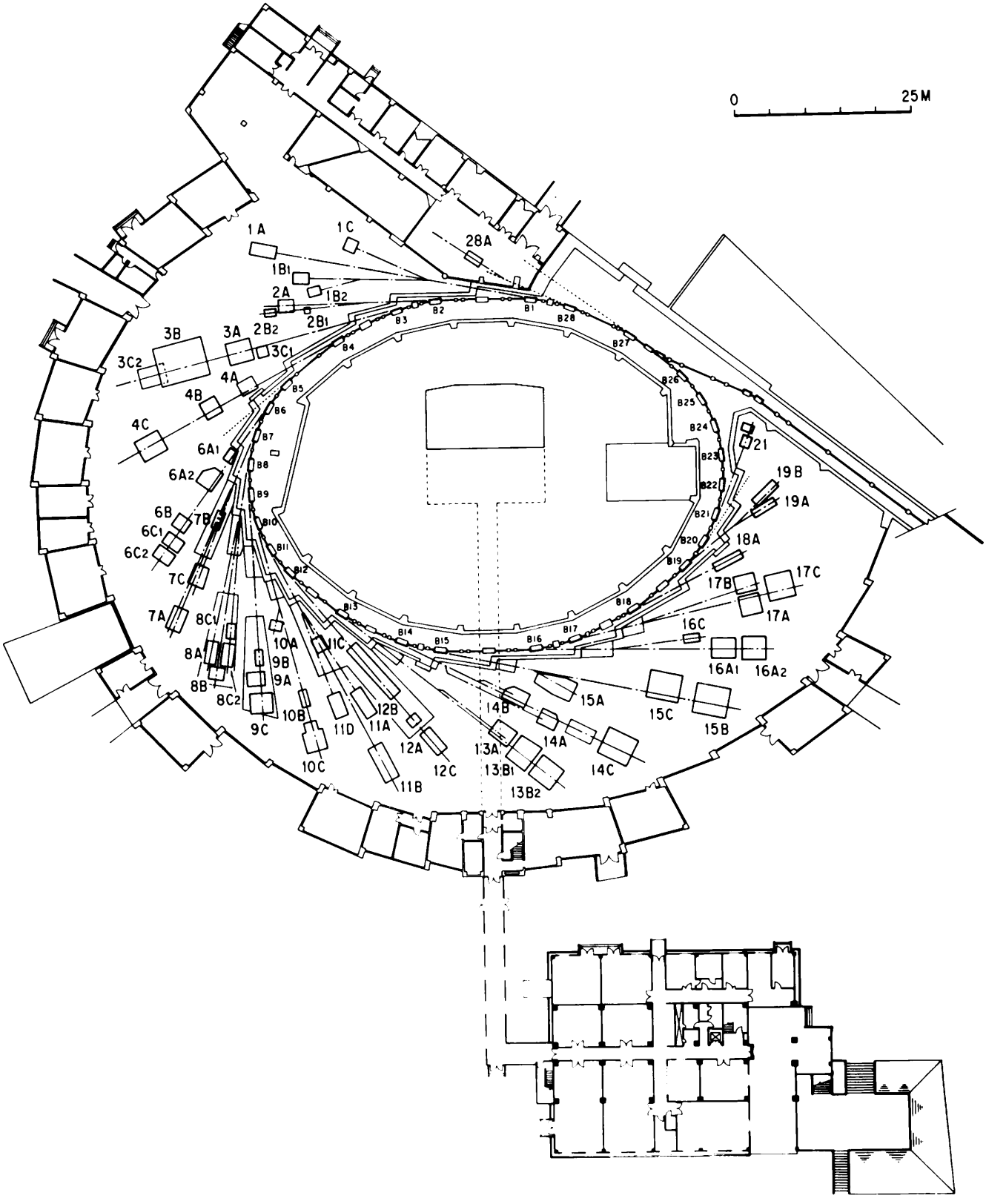

Fig. 25 Overview of the 2.5 GeV PF Ring

TABLE 1. EXPERIMENTAL STATIONS AND APPARATUSES

1. List of Experimental Stations

Beamline & Station		Contact person
BL-1	(NTT)	
1A	Solid surface analysis	M. Oshima
1B	X-ray lithography	H. Kinoshita
1C	Photo-chemical reaction	T. Urisu
BL-2	(Undulator)	
2A	Soft X-ray spectroscopy	Y. Kitajima
2B1	Soft X-ray microscopy	A. Yagishita
2B2	Soft X-ray spectroscopy	"
BL-3		
3A	X-ray diffraction and scattering	S. Sasaki
3B	24 m spherical grating monochromator	A. Yagishita
3C1	X-ray diffraction	S. Sasaki
3C2	Milli-Kelvin region X-ray topography (for solid helium)	T. Nakajima
BL-4		
4A	Trace element analysis,	A. Iida
	Radiation effects on living cells	K. Kobayashi
4B	Liquid/melt structure analysis,	K. Ohsumi
	Powder diffraction	"
4C	X-ray diffuse scattering, Fluorescent EXAFS	T. Matsushita
BL-6		
6A1	Ultra small angle X-ray scattering	M. Ando
6A2	Macromolecular crystallography by Weissenberg camera	N. Sakabe
6B	X-ray spectroscopy and diffraction	M. Nomura
6C1	X-ray diffraction at low temperatures	T. Nakajima
6C2	Accurate lattice spacing measurement	M. Ando
BL-7	(The Research Center for Spectrochemistry, Univ. of Tokyo)	
7A	Soft X-ray photoemission spectroscopy	H. Namba
7B	Surface photochemical reaction	"
7C	X-ray spectroscopy and diffraction (PF)	M. Nomura
BL-8	(Hitachi)	
8A	Soft X-ray spectroscopy	A. Nakano
8B	EXAFS	"
8C1	X-ray lithography	"
8C2	X-ray tomography and digital radiography	"
BL-9	(NEC)	
9A	X-ray lithography	J. Matsui
9B	Photochemical reaction	"
9C	EXAFS and X-ray topography/diffraction	"
BL-10		
10A	X-ray diffraction/scattering,	S. Sasaki
	Crystal structure analysis	
10B	EXAFS	M. Nomura
10C	Small-angle X-ray scattering of enzymes,	K. Kobayashi
	Surface diffraction	
BL-11		
11A	Soft X-ray spectroscopy	A. Yagishita
11B	Surface EXAFS, soft X-ray spectroscopy	Y. Kitajima
11C	VUV solid state spectroscopy	H. Kato
11D	Angle-resolved photoelectron spectroscopy	"

BL-12		
12A	VUV gas phase spectroscopy	K. Tanaka
12B	VUV high resolution absorption	K. Ito
12C	Photochemical reaction	K. Tanaka
BL-13		
13A	Accurate lattice parameter measurement	K. Nakagawa
13B1	Surface-sensitive XAFS/X-ray diffraction	H. Oyanagi
13B2	High pressure & high temperature X-ray diffraction	O. Shimomura
13C	Soft X-ray spectroscopy	N. Matsubayashi
BL-14 (Vertical wiggler)		
14A	Crystal structure analysis of proteins, EXAFS at high photon energy	S. Kishimoto
14B	High precision X-ray optics	X. Zhang
14C	Tomograp	H. Kawata
BL-15		
15A	Small-angle X-ray scattering of muscle and alloys	Y. Amemiya
15B	X-ray topography and interferometry	H. Kawata
15C	High resolution X-ray diffraction	X. Zhang
BL-16		
16A	General purpose (X-rays)	T. Matsushita
16U	General purpose (Soft X-rays)	H. Kato
BL-17 (Fujitsu)		
17A	Characterization of crystals	T. Hisatsugu
17B	Photochemical vapor deposition	"
17C	X-ray lithography	"
BL-18		
18A	Angle resolved photoelectron spectroscopy of surfaces and interfaces	A. Kakizaki
BL-19		
19A	Spin polarized photoelectron spectroscopy	A. Kakizaki
19B	Photoelectron spectroscopy at various temperatures	"
BL-21 (Light Source Division)		
	Beam position monitoring	T. Katsura
AR (Tristan Accumulation Ring)		
AR-NE-1		
1A1	Precision Compton and magnetic Compton scattering	H. Kawata
1A2	Double crystal monochromator for circularly polarized X-rays	T. Iwazumi
1B	Absorption measurement with circularly polarized soft X-rays	Y. Kitajima
AR-NE-3	Undulator X-ray beamline	X. Zhang
AR-NE-5		
5A1	Angiography	K. Hyodo
5A2	High pressure & high temperature X-ray diffraction	T. Kikegawa

2. List of Experimental Apparatuses

Format

Name of apparatus
1. General characteristics
2. Accessories
3. Other features
4. Typical Experiment
5. Station
6. Contact person
7. Pages in (A) Act. Rept. 82/83, (B) Act. Rept. 83/84, (C) Act. Rept. 84/85, (D) Act. Rept. 86, and (E) Act. Rept. 87 where detailed description is found.

X-ray

(a) X-ray fluorescence spectrometer
1. Energy dispersive type spectrometer. Equipped with a Si(Li) detector. Elemental analysis with very high sensitivity.
2. X-Z scanning sample stage.

4. Trace element analysis of semiconductor, ceramics, sea water, human tissues, etc.
Surface elemental analysis of semiconductor.
5. BL-4A.
6. A. Iida
7. (A) V-23

(b) Monochromatic X-ray irradiation system for radiation biology.
1. Usable wavelength region, 0.8 A - 3.0 A.
Beam size, typically 50 mmH × 3 mmV.
2. X-Z sample scanning stage.
Ionization chambers for measuring X-ray intensity.
4. Studies on Auger enhancement of bromine atom using various biological samples.
Wavelength dependence of radiation effects on biological samples.
5. BL-4A.
6. K. Kobayashi
7. (C) VI-21

(c) X-ray diffractometer for liquids and melts
1. Collects intensity-data for radial distribution analysis for non-crystalline materials such as gases, liquids, melts and glasses.
2. θ-2θ goniometer with monochromator and analyzer.
Single-crystal monochromator with quartz and β-alumina.
Double crystal monochromator with Si(111).
Keramax furnace.
4. Energy-dispersive study of gas and liquid.
Angle-dispersive study of liquids, melts and powder crystals.
5. BL-4B.
6. K. Ohsumi
7. (A) V-24

(d) Powder diffractometer
1. Measurement and collection of diffracted X-ray intensity from powder crystals and/or amorphous materials for profile fitting technique.
2. High speed sample spinner.
Counter monochromator (graphite).
Heating furnace.
3. $\Delta\lambda/\lambda$ - 10^{-5}
Available of energy dispersive mode of diffractometry.
Almost all of an X-ray path being in vacuum.
4. Angle-dispersive study of powder specimens or amorphous materials.
Energy-dispersive study of powder specimen or non crystalline materials.
Diffraction study using anomalous dispersion.
5. BL-4B.
6. K. Ohsumi

(e) Four-circle diffractometer with a crystal analyzer
1. Enables high resolution measurement, in momentum and energy, of intensity distribution. Intensity measurement from samples at high pressures or at low temperatures.
2. Liquid nitrogen cryostat.
4. High resolution measurement of diffuse scattering intensity, pressure dependence of commensurate-incommensurate transition.
5. BL-4C.
6. S. Kishimoto
7. (D) 160

(f) Focusing Weissenberg camera with multi-layer-linescreens
1. High resolution macromolecular crystallography with high S/N ratio.
Equipped with multi-layer-line screens.
2. Cooling unit by N_2 gas.
3. Wide range of w-axis rotation. Wide 2θ range.
4. X-ray structure determination of macro-molecular crystal (insulin, actin-DNise I complex, Plasminostreptin, etc.)
5. BL-$6A_2$.
6. N. Sakabe
7. (A) VI-5

(g) Low temperature X-ray diffractometer
1. Equipped with a three-axis goniometer (ω,2θ,χ) mainly used for low temperature ($\geq$ 0.3 K) X-ray diffraction.
2. Some types of refrigerators and magnets.
3. Available addendum limited to 500 kg in weight.
4. Structural phase transition in elpasolite at 150 mK.
Phase diagram of black phosphorus under pressure at low temperature.
Amorphous-crystalline phase transition in Ge-Si systems under high pressure at low temperature.
5. BL-6C.
6. T. Nakajima
7. (A) V-25

(h) EXAFS spectrometer (II)
1. Designed for X-ray absorption spectroscopy in transmission mode and in fluorescence detection mode.
2. Control and data acquisition system.
Closed cycle refrigerator.
4. EXAFS.
5. BL-7C.
6. M. Nomura
7. (D) 90

(i) X-ray Lithography (Hitachi Central Res. Lab.)
1. X-ray Lithography.
2. Band-pass optics, nonlinear wobbling mirror, low vacuum separating Be window, SSD X-ray detector.
3. White beam available, high speed SX shutter.
4. X-ray Lithography.
5. BL-$8C_1$.
6. T. Kimura

(j) X-ray computed tomographic imaging system (Hitachi Res. Lab.)

1. X-ray source : Monochromatic X-ray (7 keV - 40 keV).
   Detector : X-ray sensing pickup tube.
   Spatial resolution : - 10 μm.
   Field of view : ≤ 10 mm.
4. Observation of internal structure of composite ceramics.
5. BL-8C$_2$
6. K. Usami

(k) EXAFS spectrometer (NEC)

1. Designed for X-ray absorption spectroscopy in transmission mode and in fluorescence detection mode.
2. Control and data acquisition system, closed cycle refrigerator (GK ≤ T ≤ 300 K).
3. Focused beam is available.
4. EXAFS.
5. BL-9C.

(l) High-precision triple-crystal X-ray diffractometer (NEC)

1. Equipped with three crystal stages. Mainly used for a grazing incidence diffraction, X-ray topography.
2. Two high-precision goniometers (0.01"/pulse for θ, 0.004°/pulse for 2θ), two 220φ goniometers (0.0002°/pulse for φ, 0.0004°/pulse for 2φ), a 400φ goniometer (0.002°/pulse for φ), a goniometer for grazing incidence diffraction.
4. X-ray topography. Grazing incidence X-ray diffraction.
5. BL-9C.
6. J. Mizuki
7. (D) 88

(m) Six-circle-X-ray diffractometer (NEC)

1. Study of crystal structure for single crystal under various conditions (pressure & temperature).
2. Closed cycle refrigerator (13 K ≤ T ≤ 300 K), image furnace (300 K ≤ T ≤ 800 K).
4. Single crystal X-ray diffraction. Diffuse scattering.
5. BL-9C.
6. J. Mizuki
7. (D) 88

(n) Vertical-type four-circle diffractometer

1. Crystallographic studies and scattering experiments.
   Large X-circle (280 mmφ).
2. Control system with MELCOM 70/30.
   Low and high-temperature apparatus.
   X-rays film cassette. PSPC
4. Diffraction, diffuse scattering, anomalous scattering.
5. BL-10A.
6. S. Sasaki
7. (A) V-27

(o) EXAFS Spectrometer (I)

1. Dedicated to X-ray absorption spectroscopy.
   High-resolution. Easy operation.
2. Control system with a microcomputer (SORD M-223).
   Closed cycle refrigerator.
   Reaction chamber for catalyst.
   Furnace. (800°C).
4. EXAFS.
5. BL-10B.
6. A. Koyama, M. Nomura
7. (A) V-8

(p) Small angle X-ray scattering equipment for solutions (SAXES)

1. Dedicated to small-angle scattering for solutions, synthetic polymers.
2. Stopped flow apparatus.
   Temperature jump apparatus.
   Flash light for specimen.
3. Uses monochromatic beam from the optics installed at BL-10C.
4. Measurements for Bovine Serum Albumin, Lysozyme, Tobacco Mosaic Virus, Purple Membrane, etc.
5. BL-10C.
6. K. Kobayashi
7. (A) V-29

(q) Ultra-high vacuum X-ray diffractometer

1. Ultra-high vacuum with cryo-pumping system.
   Equipped with X-ray diffractometer and LEED optics.
2. Super precision goniometer using elastic torsion mechanism.
   Microcomputer control system.
   NaI scintillation counter system and SSD.
4. Study on Si(7 × 7) structure.
5. BL-10C.
6. T. Ishikawa
7. (A) V-34

(r) Time-resolved X-ray measurement system with 1D-PSD

1. Time resolution up to 1 msec.
   Either 256 ch. × 191 frames, 512 ch. × 95 frames, or 1024 ch. × 47 frames.
   Fast data acquisition up to 1 MHz.
2. LSI 11/23 computer.
   CAMAC modules (Time to Digital Converter, Histogramming Memory, etc.).
3. Uses monochromatic X-ray (λ = 1.5 Å).
4. Measurements on frog skeletal muscle, purple membrane, Ribosome, etc.
5. BL-10C, BL-15A1.
6. Y. Amemiya
7. (A) V-35

(s) Horizontal-type four circle diffractometer

1. Specially built, but having a conventional diffractometer configuration.

Fully computer-controlled for rapid, tunable and precise diffraction data collection.

2. Computer-controlled alignment carriage with 5 stepping motor driven axes, on which the diffractometer is mounted.
Rotation camera.
MELCOM 70/60 minicomputer with OPTRONICS FILM SCANNER.

3. Mechanical control interfaced through IEEE-488 bus.
CAMAC and NIM measuring system.

4. Crystal structure analysis of antibiotics, biotic metabolitos, proteins, etc.

5. BL-14A.

6. S. Kishimoto

7. (A) V-30

(t) High-speed X-ray topography camera

1. Equipped with two X-ray TV cameras.
Maximum load of 30 kg on sample goniometer.
Facilities simultaneous observation of two different Laue spots.

2. Microcomputer system (AIDACS-3000).
Image processor TF4110.
Work shutter for variable exposure time (0.1 - 9.9 sec.).

3. 1 arc sec accuracy of θ-rotation.
Ample space around the specimen position.

4. Melting process of GaAs.
Magnetization process of Fe-3% Si, etc.

5. BL-15B, BL-14C.

6. H. Kawata

7. (A) V-31

(u) X-ray diffractometer for gasses

1. Equipped with horizontal ω-2θ two-circle goniometer.
χ-ϕ circle motion available.

2. Gas cell with boiling system.
Gas cell for pressure tight experiments.
Incident beam monitor with SSD.

3. Uses white beam for energy-dispersive method. Uses monochromatic beam for angle-dispersive method.

4. Angle-dispersive X-ray diffraction and Compton scattering study of carbon dioxide.

5. BL-15C, 14C.

6. T. Mitsuhashi

7. (B) VI-172

(v) Three-axes X-ray diffractometer

1. Equipped with three precision goniometers (Huber 410, 420, and 440).

2. Scintillation counter.
SSD with MCA.
Asymmetry cut plane monochromator.

3. Accuracy of 0.36 arc sec per pulse.

4. Phase-contrast microscopy.
Development of application to medical diagnosis.

5. BL-15B.

6. H. Kawata

7. (A) V-32, VI-97, VI-98

(w) Precision X-ray optics

1. Goniometer assembly dedicated to precision diffraction study such as double-, triple-, and more than triple-crystal diffractometry and topography.

2. Microcomputer control system.
NaI scintillation detector system.
SSD and MCA.
Ionization chamber for monitoring.
Room temperature controller.
Experimental table with air springs.

3. 1 arc sec accuracy for full rotation.
0.1 arc sec accuracy within 6° using tangential bar system.
Employs super-precision rotation mechanism with elastic torsion and PZT.

4. Detection of polarization rotation under magnetic diffraction condition.
Structure analysis of epitaxial layer/substrate interfaces with standing wave method.

5. BL-15C.

6. X. Zhang

7. (A) V-33

(x) X-ray diffraction

1. Equipped with horizontal or vertical θ-2θ goniometer.

2. Measurable in He gas.
Usable an additional monochrometer.

3. A double crystal monochrometer is set at the beamline.

4. General Purpose.

5. BL-17A.

6. S. Komiya

(y) Rapid acquisition system of two dimensional images for medical application

1. Dedicated to development of medical diagnosis using two-dimensional image acquisition system.
Large exposure area (70 mmH × 120 mmV) is obtained by asymmetrical reflection from a crystal.
Usable energy is 33 KeV ± 3 KeV.

2. Two-dimensional detector system using a metal image intensifier.
Si single-crystal monochromator with 311 reflection or 111 reflection.
Z scanning table detector and sample.
X scanning stage for sample.

4. Studies on medical application to diagnosis such as angiography, K-edge subtraction and computed tomography.

5. AR-NE-5A1.

6. K. Hyodo

(z) Multi anvil high pressure X-ray system

1. Maximum pressure 13 GPa.
Maximum temperature 1700 °C.
Sample volume (typical) 2 mmϕ × 3 mmH.
White and monochromatic X-ray.

2. Two axis goniometer.
Handy type SSD (pure Ge).

3. Best quality in the world for this research field.

4. Structure of liquid Se, Ga and Bi at high pressure.
Precise determination of the equation of state of mantle minerals.
Measurement of Debye-Waller factors of Al and Mo at high pressure.
5. AR-NE-5A2.
6. T. Kikegawa
7. (A) V-26

Soft X-ray and VUV

(a) Monochromatic soft X-ray irradiation system for radiation biology studies
1. Usable wavelength 3 Å - 6.5 Å.
Beam size, typically 7 mmH × 4 mmV.
2. X-Z sample scanning chamber.
4. Biological effects of soft X-ray resonance absorption around the K-shell absorption edge of phosphorus.
5. BL-1B.
6. K. Kobayashi
7. (D) 235

(b) Gas-phase angle resolved photoelectron spectrometer
1. Ultimate pressure 5×10^{-8} Torr.
Equipped with a conventional hemispherical electrostatic analyzer and with a position-sensitive parallel-plate electrostatic analyzer.
2. Sample-gas inlet system.
3. A sample gas is confined in a gas cell.
5. BL-2B2.
6. A. Yagishita
7. (A) V-42

(c) Reflection, absorption, and photoemission (Hitachi Advance Res. Lab.)
1. Spectrometer.
2. Evaporator.
4. Analysis of multilayered structure, evaluation of optical elements, and study of electronic structure of superconductors.
5. BL-8A.
6. Y. Hirai

(d) SR induced photochemical reaction (NEC)
1. High vacuum (4×10^{-10} Torr).
2. Reactant-gas inlet system.
Angle resolved Q-pole mass spectrometer.
RHEED, AES, EELS.
4. SR induced photochemical reaction.
5. BL-9B.
6. I. Nishikawa

(e) VUV and soft X-ray reflectometer
1. Equipped with a goniometer, insuring accurate incidence angle (30 sec).
Up to 89.4° incidence angle.
Easy optical alignment.
Easy sample exchange.
High vacuum (2×10^{-9} Torr).
3. Equipped with ports for vacuum evaporation.
4. Optical constants of mirror materials.
Surface roughness.
5. BL-11A.
6. W. Okamoto
7. (A) V-41, VI-78

(f) Apparatus for surface EXAFS experiments
1. Base pressure < 1×10^{-10} mbar.
Equipped with a CMA and a soft X-ray fluorescent proportional counter.
2. Some equipments for sample preparation and characterization such as LEED, Ar^+ ion gun, e-gun for AES.
3. Mobile.
4. Surface EXAFS and soft X-ray standing wave method.
5. BL-11B.
6. Y. Kitajima
7. (B) V-9

(g) UHV experimental chamber for absorption measurements I.
1. Ultra-high vacuum (5×10^{-11} Torr).
Equipped with an electron-beam gun for evaporation of samples.
Equipped with a quartz oscillator capable of being cooled to LNT.
2. Sample holder with an adjustable linear motion, capable of being cooled to LNT.
3. Designed mainly for very reactive metal samples.
4. Absorption of alkali metals, alkali metal alloys, and rare earth metals.
Near-normal reflectance.
5. BL-11C, BL-11D, BL-11A.
6. T. Miyahara
7. (A) VI-82

(h) Apparatus for ARPES experiment for solid state
1. Base pressure 5×10^{-11} Torr.
Equipped with a hemispherical analyzer mounted on a two axis rotation mechanism.
2. Some equipments for sample preparation and characterization.
Sample bank and transfer system.
Sample gas inlet system.
4. Mainly for angle-resolved photoelectron spectroscopy (ARPES) of single crystals.
5. BL-11D.
6. H. Kato
7. (B) V-10

(i) Time-of-flight spectrometer for photoion measurements
1. Ultimate pressure 5×10^{-8} Torr.
Electrostatic lenses satisfying the conditions of double-field space focusing for ions.
2. Furnace to evaporate alkali and alkaline-earth metals.
4. The measurements of double and multiple photoionization cross sections of Ca, Sr, Rb, Cs and Ba.
5. BL-2A, BL-11A.
6. A. Yagishita
7. (A) V-40

(j) Multi-technique surface analysis system (NTT)

1. Surface analyses such as photoemission spectroscopy, surface EXAFS, AES, SIMS, LEED EELLS and ISS in conjunction with an MBE chamber.
2. CLAM analyzer, angle-resolved electron analyzer, LEED optics, Q-mass filter, X-ray source, ELS electron gun, auger electron gun, He ion gun.
4. Surfaces and interfaces of semiconductors and superconductors by using SRPES and SEXAFS.
5. BL-1A.
6. M. Oshima
7. (D) 144-117

(k) Angle resolved electron spectrometer (RCS)

1. Electron spectroscopy for surface studies.
2. Low energy electron diffraction, auger electron spectroscopy, surface preparation tools.
3. Based on beamline ADES 400 of V.G.
4. Photoelectron spectroscopy, surface EXAFS.
5. BL-7A and 7B.
6. H. Namba (University of Tokyo)

(l) X-ray lithography (Fujitsu Lab.)

1. X-ray lithography.
2. Low-pass mirror, energy dispersive type spectrometer with a Si(Li) detector.
3. White beam is available.
4. X-ray lithography.
5. BL-17C.
6. S. Gotoh
7. (E) 81

(m) XPS vacuum chamber

1. Two-box type XPS chamber with separation valve.
2. Sample preparation chamber, DCMA.
3. Ultra-high vacuum (3×10^{-10} Torr).
4. XPS of rare-earth compounds.
5. BL-2A, BL-11B.
6. T. Miyahara
7.

Table 2. X-Ray Beamline Optics and Monochromators

Branch Beam Line	Horizontal Acceptance Angle (mrad)	Typical Beam Size (Hmm × Vmm)	Photon Flux at Sample Position	Monochromator (Crystal)	Energy Resolution ($\Delta E/E \times 10^{-4}$)	Energy Range (keV)	Mirror	Line Vacuum (Gas)
BL-3A	4	80 × 3 (4 × 0.1)		Double Crystal Si (111) (Sagittal Focusing)	~ 2	4 ~ 25	Collimating and Refocusing Mirrors (Fused Quartz)	Vacuum
BL-3C1	2	20 × 4		None		4 ~ 30	None	Vacuum
BL-4A	6	50 × 4 (4 × 1)		Double Crystal Si (111) (Sagittal Focusing)	~ 2	4 ~ 20	None	Vacuum
BL-4B	4.5	50 × 5		Double Crystal Si (111)	~ 2	4 ~ 35	None	Vacuum
BL-4C	4	4 × 1		Double Crystal Si (111) (Sagittal Focusing)	~ 2	4 ~ 20	None	Vacuum
BL-6A1	0.1	10 × 3		Plane (111)	7.5	8 ~ 17		Vacuum
BL-6A2	4	2.5 × 1		Bent Si (111) (α = 0, 6.0°, 7.8°, 9.5°, 11.4°, 13.7°, 16.5°)		5 ~ 25	Bent Plane Fused Quartz	Vacuum
BL-6B	4	8 × 1		Double Crystal Si (220), Si (111) (Sagittal Focusing)		4 ~ 25 (4 ~ 16 when focused)	None	Vacuum
BL-6C1	0.5	10 × 5		None		8 ~ 30		Vacuum
BL-6C2	0.5	5 × 5		Channel-Cut Si (111)	7.5	8 ~ 12	None	Vacuum
BL-7C	4	8 × 1	$4 \times 10^9/7mm^2$ (8 keV, 100 mA) (3×10^{10} when focused)	Double Crystal Si (111) (Sagittal Focusing)	2	4 ~ 20 (4 ~ 13 when focused)	None	Vacuum

Branch Beam Line	Horizontal Acceptance Angle (mrad)	Typical Beam Size (Hmm × Vmm)	Photon Flux at Sample Position	Monochromator (Crystal)	Energy Resolution $(\Delta E/E)\times10^{-4}$	Energy Range (keV)	Mirror	Line Vacuum (Gas)
BL-8C	5	50 × 5	2×10^6/mA·mm^2 at 10 keV with Si (111)	Channel-Cut Si (220), Si (111), Si (400)	~ 2	5 ~ 40	None	Vacuum & Helium
BL-9A	5	25 × 25				1.2 ~ 3.1	SiC	Vacuum
BL-9C	5	150 × 5		Double Crystal Si (111) (Sagittal Focusing)	~ 2	5 ~ 25	None	Vacuum
BL-10A	1	10 × 3		Si (111), Si (220) Ge (111), InSb (111) Quartz (100), PG (002) Curved Si (111) (α ~ 4°, 8°)	50 ~ 5	5 ~ 25	None	Helium
BL-10B	2	8 × 1	3×10^8/7mm^2 (10 keV, 100 mA)	Channel-Cut Si (311)	1	6 ~ 30	None	Vacuum
BL-10C	4	6 × 1.5	~ 10^{10}/9mm^2 (8 keV, 100 mA)	Double Crystal Si (111)	2	4 ~ 10	Bent Cylinder	Helium
BL-13A	1			Double Crystal Si (220)	~ 0.1	4 ~ 30	None	Vacuum
BL-13B	4			Double Crystal Si (111), Si (220)	~ 2	4 ~ 25	Bent plane Fused Quartz	Vacuum
BL-14A	1.28 (Vertical)	5 × 38		Double Crystal Si (111) Si (331) Si (553)	2	5.1 ~ 19.1 12.9 ~ 48 22.7 ~ 84.5	Bent Cylinder for Vertical Forcusing, Pt-cauted Fused Quartz	Vacuum (line) Helium (monochromator)
BL-14B	2.2	5 × 30		Double Crystal Si(111),Si(220),Si(311) (Sagittal Focusing)	2	5.2 ~ 57	None	Vacuum
BL-14C	1.3	10 × 40		Double Crystal Si (111)	2	5.5 ~ 43	None	Vacuum
BL-15A	2	2.6 × 1.3	9×10^{10}/6mm^2 (8.0 keV, 150 mA)	Curved Crystal Ge (111) (α = 8.0°)	~ 10	5.6 ~ 12.4	Cylinder, Fused Quartz	Vecuum and Helium

Branch Beam Line	Horizontal Acceptance Angle (mrad)	Typical Beam Size (Hmm × Vmm)	Photon Flux at Sample Position	Monochromator (Crystal)	Energy Resolution $(\Delta E/E)\times 10^{-4}$	Energy Range (keV)	Mirror	Line Vacuum (Gas)
BL-15B	0.14	5 × 5		None		3.5 ~ 34	None	Vacuum
BL-15C	2	60 × 6		None		4 ~ 35	None	Vacuum
BL-16X	4	4 × 1		Double Crystal Si (111) (Sagittal Focusing)	~ 2	4 ~ 35	Commissioning	Vacuuum
BL-17A	4	100 × 10		Double Crystal Si (111)	~ 2	4 ~ 5	None	Vacuum
BL-17C	1	20 × 5		None		1	Quartz (plane)	Vacuum
AR-NE1-A1	2	30 × 7 (3 × 1)		Single Crystal Si (111) (Double bent crystal Si (111))	~ 10	50 ~ 70	None	Vacuum
AR-NE1-A2 AR-NE1-B	2	80 × 10 (10 × 10)		Double Crystal Si (111) (Sagittal Focusing)	~ 2	6 ~ 100	In Planning	Vacuum
AR-NE5-A1	10	120 × 70		Single Crystal Si (311) (α = 5.9°)	~ 60	33	None	In Planning
AR-NE5-A2	10	30 × 10		Double Crystal Si (111) (Sagittal Focusing)	~ 10	30 ~ 100	None	In Planning

Table 3. VUV and Soft X-Ray Monochromators

Branch Beamline	Monochromator	Grating/Crystal	Groove density (l/mm)/spacing	Blaze (A)	Typical Resolution	Range (A)
BL-1A (NTT)	Grating/Crystal	Au-Coated Original InSb(111) Si(111)	1200 2d = 7.4806 A 2d = 6.270		$\lambda/\Delta\lambda$ ~ 2000	2 ~ 2000
BL-1B (NTT)	Filtered White					
BL-1C (NTT)	Plane Grating	Pt-coated	1200 600		$\lambda/\Delta\lambda$ ~ 100	
BL-2A	Double Crystal with Constant Exit Beam	InSb(111)	2d = 7.4806 A			7.3 ~ 2.0
BL-2B1	Fresnel Zone Plate Microscope					30 ~ 15
BL-2B2	10m Grazing Incidence with Fixed Incidence Angle of 89°	Au-Coated Replica (Hitachi)	2400 1200	8 16	$\Delta\lambda$ = 0.004 A $\Delta\lambda$ = 0.008 A for 10μ–10μ Slits	6 ~ 25 6 ~ 50
BL-7A (RCS)	Grazing Incidence	Plane Au-Coated (Hitachi) " (Shimadzu)	1200 2400		$\lambda/\Delta\lambda$ ~ 500	12 ~ 1200
BL-7B (RCS)	1m Seya-Namioka	Au-Coated Replica (Hitachi, B & L)	1200 2400	380 960 1600	$\lambda/\Delta\lambda$ > 1000	275 ~ 2500
BL-8A (Hitachi)	Grazing Incidence	Plane Self-focusing	2400 800	5 80	$\lambda/\Delta\lambda$ ~ 10^{-3}	7 ~ 100 80 ~ 300
BL-8B (Hitachi)	Double Crystal	InSb(111), Beryl(1010) Si(311), (422)			$\lambda/\Delta\lambda$ ~ 10^{-4}	0.4 ~ 1
BL-9A (NEC)	Oscillating Mirror					
BL-9B	Grazing Incidence	Plane				30 ~ 2000

Branch Beamline	Monochromator	Grating/Crystal	Groove density (l/mm)/spacing	Blaze (A)	Typical Resolution	Range (A)
BL-11A	Grasshopper Mark VII	Au-Coated Replica (Hitachi)	2400	16.6	$\Delta\lambda$ = 0.02 A	10 ~ 145
	2m Grazing Incidence with Fixed		1200	33.3	$\Delta\lambda$ = 0.04 A	10 ~ 290
	Incidence Angle of 88°				for 10μ–10μ Slits	
BL-11B	Double Crystal	InSb(111)	2d = 7.4806 A		ΔE = 0.8 eV at 2 keV	3 ~ 7
		Si (111)	2d = 6.2710 A		ΔE = 0.6 eV at 3 keV	2.5 ~ 5.9
BL-11C	1m Seya-Namioka	Au-Coated Replica (Hitachi)	2400	785	$\Delta\lambda$ = 0.3 A at 500 A	400 ~ 150
		Al-Coated Replica (Shimadzu)	1200	785	for 50μ–50μ Slits	400 ~ 3000
			1200	1300		
BL-11D	2m Grqazing Incidence Constant	Au-Coated Replica	2400	32	$\lambda/\Delta\lambda$ ~ 1700	80 ~ 150
	Deviation	(B & L, Hitachi)	1200	116	for 25μ–25μ Slits	120 ~ 300
	($\alpha + \beta$ = 154°)		600	460		240 ~ 600
BL-12A	1m Seya-Namioka	Au-Coated Replica	2400	508	$\Delta\lambda$ = 0.4 A at 500 A	350 ~ 1000
		(B & L)	1200	536	for 100μ–100μ Slits	350 ~ 2000
BL-12B	6.65m Normal Incidence Off-	Pre-Coated Replica (B & L)	1200	1500		
	Plane Eagle Mounting	Os-Coated Replica (B & L)	1200	5500	$\lambda/\Delta\lambda = 2.5 \times 10^5$ A	400 ~ 2500
		Os-Coated Replica (Hyperfine)	4800	900	at ~ 800 A	
BL-12C	Multilayer Reflector	Rh-Si 21 Layers			$\lambda/\Delta\lambda$ ~ 12	20 ~ 180
BL-16U	Grazing Incidence				$\lambda/\Delta\lambda > 1000$	20 ~ 300
BL-18A	Grazing Incidence		1200		$\lambda/\Delta\lambda > 1000$	40 ~ 1000
BL-19A	Grazing Incidence Constant	Au-coated (Shimadzu)	1200	50	$\lambda/\Delta\lambda > 1000$	50 ~ 127
	Deviation			132	for 20μm-20μm Slits	99 ~ 253
	($\alpha + \beta = 160°, 170°$)		600	198		80 ~ 496
				500		359 ~ 992
BL-19B	Plane Grating	Original Varied Spaced	2400		$\lambda/\Delta\lambda > 1500$	10 ~ 150
		Plane Grating (Hitachi)	800		for 20 μm-20μm Slits	30 ~ 450

Branch Beamline	Monochromator	Grating/Crystal	Groove density (l/mm)/spacing	Blaze (A)	Typical Resolution	Range (A)
BL-28	Normal/Grazing Incidence Constant Deviation	Holographic (Shimadzu)	600 1200 2400		$\lambda/\Delta\lambda > 2000$	50 ~ 1500
AR-NE1-B	10m Grazing Incidence (Vertical Dispersion)	Au-Coated (Hitachi)	2400 1200	8 16	$\Delta\lambda = 0.001$ A $\Delta\lambda = 0.002$ A	6 ~ 25 6 ~ 50

Table 4. Optical Elements of VUV and Soft X-Ray Beamlines

Branch Beamline	Pre- and Re-focussing mirror	Radius of Curvature (mm)	Angle of Incidence	Material	Coating	Dimension (mm)	Horizontal & Vertical Acceptance (mrad)	Typical Beam Size (mm)
BL-1A	Paraboloidal		89°	Fused Quart	Pt	500 × 80 × 50	4.0 × 0.5	
(NTT)	Paraboloidal		89°	Fused Quartz	Pt	500 × 80 × 50		4 × 1
BL-1B	Plane		88° ~ 89°	SiC			1.2 × 4.0	
(NTT)						19 ϕ		
BL-1C (NTT)	Toroidal			Fused Quartz	Pt		2.0 × 4.0	
BL-2B1	Plane		88°	SiC	Pt	120 × 60 × 15		
BL-2B2	Plane		86.85° ~ 88.83°	SiC	Pt	120 × 60 × 15	0.14 × 0.4	
	Concave	8903	89°	Pyrex	Pt	ϕ 90 × 15		
	Concave	7527	89°	Pyrex	Pt	ϕ 90 × 15		
	Toroidal	R = 43574, ρ = 26.162	89°	Fused Quartz	Pt	240 × 40 × 15		
BL-7A (RCS)	Bent Cylindrical	R = 7.83 $\times 10^5$, ρ = 420	88.4°	Quartz	Pt	750 × 140 × 30	6 × 1	
	Toroidal	R = 2.58 × 10^4, ρ = 90	88.3°	Quartz	Pt	200 × 60 × 18		2 × 1
BL-7B	Cylindrical	1600	15°	Cu	Pt	250 × 80 × 30	6 × 4	
(RCS)	Toroidal	R = 2510, ρ = 200	10°	Quartz	Pt	60 × 80 × 20		1 × 1
BL-8A	Plane		89°	Quartz	Pt	400 × 170 × 40	0.5 × 1.0	
(Hitachi)	Bent	6.5 × 10^4	89°	Quartz	Pt	160 × 50 × 5		5 × 1
BL-8B (Hitachi)	Bent Cylindrical	R = 1.6 × 10^6 ρ = 1.7 × 10^2	6.3 mrad	Quartz	Ni	500 × 120 × 30	6 × 0.5	
BL-9A	Plane		89.15°	SiC		400 × 170 × 40	5 × 0.33	
(NEC)	Cylindrical	309.5	89.15°	SiC		400 × 170 × 40	5 × 0.33	
BL-9B	Plane		87°	SiO_2	Pt	700 × 60 × 20	0.2 × 0.2	

Branch Beamline	Pre- and Re-forcussing mirror	Radius of Curvature (mm)	Angle of Incidence	Material	Coating	Dimension (mm)	Horizontal & Vertical Acceptance (mrad)	Typical Beam Size (mm)
BL-11A	Spherical	360000	88°	SiC	Pt	400 × 170 × 40	1.3 × 0.4	
	Spherical	28000	88°	Fused Quartz	Au	300		
	Bent Cylindrical	R ~ 3000	89°	Pyrex	Pt	220 × 24 × 6		1 × 0.3
BL-11B	Bent Cylindrical	R ~ 950000, ρ = 300	89°	Fused Quartz	Pt	580 × 140 × 30	4.0 × 0.6	8 × 1
BL-11C	Plane		77.5°	SiC	None	250 × 100 × 40	4.8 × 3.0	
	Concave	5600	42.5°	Fused Quartz	Pt	100 × 100 × 20		
	Toroidal	R = 125, ρ = 2000	72.5 °	Pyrex	Au	90 × 50 × 10		~ 1 ϕ
BL-11D	Toroidal	R = 250000, ρ = 750	86°	SiC	Pt	400 × 80 × 40	1.5 × 2.0	
	Plane		86°	Quartz	Au	50 × 40 × 10		
	Concave	4000	86°	BK-7	Au	50 × 40 × 10		
	Toroidal	R = 3500, ρ = 700,	77°	BK-7	Au	60 × 40 × 10		~ 1 ϕ
BL-12A	Cylindrical	R = 1850	80°	SiC	None	250 × 200 × 40	2.4 × 1.5	
	Spherical	6250	45°	Fused Quartz	Pt	ϕ 100 × 20		
	Plane		80°	Pyrex	Pt	40 × 40 × 10		~ 1 ϕ
	Toroidal	R = 2000, ρ = 340	70°	Pyrex	Pt	30 × 40 × 10		
	Plane		80°	Pyrex	Pt	40 × 40 × 10		
BL-12B	Plane		80°	SiC	None	280 × 100 × 40	5.0 × 3.6	
	Concave	4321	35°	Pyrex	Pt	ϕ 110 × 20		
	Concave	2188.5	45°	Pyrex	Pt	ϕ 110 × 20		
BL-12C	Toroidal	R = 490455, ρ = 539,	88.1°				3.8 × 1.0	2 × 1
BL-16U	Cylindrical	R = 205294	87°	SiC	Pt	500 × 50 × 40	1.74 × 0.24	
	Plane			SiC	Pt	100 × 40 × 15		
	Cylindrical	R = 1796	87°	SiC	Pt	100 × 40 × 15		
	Bent Cylindrical	ρ = 52.4	86.22°	Quartz	Pt	220 × 30 × 8		
BL-17C (Fujitsu)	Plane		89° ~ 89.4°	Quartz	Pt	500 × 130 × 30	1.0 × 0.5	

Branch Beamline	Pre- and Re-forcussing mirror	Radius of Curvature (mm)	Angle of Incidence	Material	Coating	Dimension (mm)	Horizontal & Vertical Acceptance (mrad)	Typical Beam Size (mm)
BL-18A	Cylinderical	R = 203252	87.5°	SiC	Au	500 × 50 × 50	2.0 × 2.0	
	Plane		86°	Quartz	Au	420 × 30 × 40		
	Bent Ellipsoidal		87°	Quartz	Au	440 × 40 × 40		
	Toroidal	R = 16894, ρ = 72.9	87°	Quartz	Au	260 × 30 × 30		~ 0.5 ϕ
BL-19A	Plane		85°	SiC	Au	400 × 100 × 50	3.5 × 2.0	
	Toroidal	R = 350000, ρ = 372	86°	Quartz	Au	400 × 100 × 50		
	Spherical	R = 28000	86°	Quartz	Au	100 × 60 × 10		
	Toroidal	R = 13800, ρ = 320	85°	Quartz	Au	60 × 40 × 10		
	Toroidal	R = 7230, ρ = 1035	80°	Quartz	Au	60 × 40 × 10		< 0.3 ϕ
	Plane		80°	Quartz	Au, Al	60 × 40 × 10		
BL-19B	Cylindrical	R = 500000	88.5°	SiC	Au	520 × 100 × 50	2.0 × 2.0	
	Plane		88.5°	SiC	Au	500 × 50 × 40		
	Toroidal	R = 38199, ρ = 52.3	87°	Quartz	Au	200 × 40 × 20		< 0.7 × 0.5
BL-28	Toroidal	R = 250000, ρ = 680	86°					
AR-NE1-B	Plane		88.5°	SiC	Pt	500 × 40 × 40	0.2 × 0.2	
	Bent Cylindrical	R = Variable, ρ = 485	88.5°	SiO_2	Pt	700 × 40 × 20	0.2 × 0.2	

User's Short Reports

ISSN 0912-1803

PHOTON FACTORY ACTIVITY REPORT 1989

#7

PHOTON FACTORY ACTIVITY REPORT 1989 #7